Heat: A powerful tool for colloidal particle shaping

Originally published in:
Advances in Colloid and Interface Science 331, https://doi.org/10.1016/j.cis.2024.103240

Advances in Colloid and Interface Science 331 (2024) 103240

Contents lists available at ScienceDirect

Advances in Colloid and Interface Science

journal homepage: www.elsevier.com/locate/cis

Historical Perspective

Heat: A powerful tool for colloidal particle shaping

Valeria Lotito *, Tomaso Zambelli *

Laboratory of Biosensors and Bioelectronics, Institute for Biomedical Engineering, ETH Zurich, Gloriastrasse 35, 8092 Zurich, Switzerland

ARTICLE INFO

Keywords:
Colloidal particle shaping
Colloidal morphology
Colloidal self-assembly
Thermal annealing
Sintering
Colloidal lithography

ABSTRACT

Colloidal particles of spherical shape are important building blocks for nanotechnological applications. Materials with tailored physical properties can be directly synthesized from self-assembled particles, as is the case for colloidal photonic crystals. In addition, colloidal monolayers and multilayers can be exploited as a mask for the fabrication of complex nanostructures via a colloidal lithography process for applications ranging from opto-electronics to sensing. Several techniques have been adopted to modify the shape of both individual colloidal particles and colloidal masks. Thermal treatment of colloidal particles is an effective route to introduce colloidal particle deformation or to manipulate colloidal masks (i.e. to tune the size of the interstices between colloidal particles) by heating them at elevated temperatures above a certain critical temperature for the particle material. In particular, this type of morphological manipulation based on thermal treatments has been extensively applied to polymer particles. Nonetheless, interesting shaping effects have been observed also in inorganic materials, in particular silica particles. Due to their much less complex implementation and distinctive shaping effects in comparison to dry etching or high energy ion beam irradiation, thermal treatments turn out to be a powerful and competitive tool to induce colloidal particle deformation. In this review, we examine the physicochemical principles and mechanisms of heat-induced shaping as well as its experimental implementation. We also explore its applications, going from tailored masks for colloidal lithography to the fabrication of colloidal assemblies directly useful for their intrinsic optical, thermal and mechanical properties (e.g. thermal switches) and even to the synthesis of supraparticles and anisotropic particles, such as doublets.

1. Introduction

Material engineering based on bottom-up approaches is an enticing route in comparison with top-down nanofabrication techniques such as photolithography or electron beam lithography due to its lower cost and time burden, which paves the way for high scale and large area fabrication. To this end, spherical colloidal particles self-assembled in both two-dimensional (2D) and three-dimensional (3D) arrangements represent a reliable and robust workhorse. Silica and polymer colloids are the most commercially available and most widespread building blocks for colloidal particle assemblies [1–4].

Particle monolayers and multilayers can be effectively used as a template for the fabrication of nanostructures by further processing steps (e.g. deposition or etching of material in the area not masked by the particles) in the so-called colloidal lithography or nanosphere lithography or natural lithography process [1,5]. In this case, they typically serve as a sacrificial material and are removed at the end of the process [1,5]. In other cases, 2D and 3D particle assemblies are directly exploited for their inherent physical properties, e.g. optical properties for photonic crystals [1,6]. Independently of their indirect use as a mask or their direct use for their intrinsic properties, applications range from sensors to optoelectronic devices, photovoltaics, optical metasurfaces, surface engineering, light harvesting and environmental remediation [1,7,8].

By tuning the experimental conditions, structures with different degrees of order (e.g. crystalline or amorphous) and symmetry (e.g. hexagonal, rhombic, square) and density (e.g. closely-packed, non-closely-packed) can be obtained; single-sized, binary and polydispersed particles can be used [9–13]. A wide variety of self-assembly techniques is available to control the final arrangements [1,10,11,14–17]. All these factors can be exploited to tune the morphology of the colloidal masks when particles are used for colloidal lithography or to directly engineer the physical properties of colloidal assemblies.

In order to further enrich the variety of attainable structures and materials, specific approaches have been developed to shape colloidal particles after self-assembly [1]. One common approach is to resort to

* Corresponding authors.
E-mail addresses: valerialotito.vl@gmail.com, lotito@biomed.ee.ethz.ch (V. Lotito), zambelli@biomed.ee.ethz.ch (T. Zambelli).

https://doi.org/10.1016/j.cis.2024.103240
Received in revised form 10 June 2024;
Available online 20 June 2024

dry etching [5,18–23]. This method is typically used to reduce particle size, which can be exploited to turn a closely-packed arrangement into a non-closely-packed arrangement [5,18]. In addition, for specific dry etching conditions, characteristic morphological deformations can be obtained, for instance the formation of necks between neighbouring particles [18–23]. Besides, as the induced deformation is typically anisotropic (due to preferential etching in the direction orthogonal to the substrate on which particles are assembled), anisotropic particles can be synthesized starting from spherical ones [18,24–26]. Also high energy ion beam irradiation can be exploited to change particle shape both at individual and collective level (isolated particles or particle assemblies) to get modified colloidal masks with tunable interstice size or sintered particles (with the formation of necks between neighbouring particles until their complete coalescence) or anisotropic particles (ellipsoidal or more complex shapes) depending on the particle characteristics (e.g. material) and irradiation conditions (e.g. energy and type of ion, angle of irradiation) [9,27–33]. However, all these methods require complex and expensive equipment.

Thermal treatment of colloidal particles represents a more straightforward and affordable approach to tailor the morphology of colloidal particles and colloidal masks. Different shaping effects can be obtained depending on particle characteristics (such as size and material) and experimental implementation of the thermal treatment (for instance, how heat is applied, temperature and duration of the treatment). Mainly used for polymer particles, it has been adopted also for inorganic materials, such as silica. Many physicochemical properties intervene in particle shaping, in particular critical temperatures for particle material (glass transition temperature and melting temperature) relative to the temperature of thermal treatment and surface groups involved in dehydration and dehydroxylation processes.

Heat can be effectively used for particle shaping to achieve deformations useful in indirect use of colloidal particles for colloidal lithography, for example by tuning the size and shape of the interstices between neighbouring particles in monolayers of hexagonal closely-packed particles. In addition, colloidal assemblies modified via thermal annealing and sintering can be directly exploited for their optical, thermal and mechanical properties, for instance by harnessing the variation in spectral properties, thermal conductivity and mechanical stability upon necking and coalescence between particles due to heating. Moreover, it can be exploited to get particles with specifically engineered morphology, such as anisotropic shapes (e.g. doublets consisting of two particles of the same type or of different type) from spherical particles, or to increase the cohesion between particles composing supraparticles or colloidosomes.

In this review, we provide a thorough description of thermal treatments of spherical colloidal particles, focusing on polymer and silica particles. First, we will describe the physicochemical properties that play a key role in material deformation upon heating. Then, we will focus on the specific theoretical models and mechanisms behind colloidal particle deformation. Subsequently, we will dwell on the experimental implementations of thermal treatment of colloidal particles, by distinguishing between the cases in which the thermal treatment is carried out on particles assembled on a substrate (polymeric or non-polymeric) or at the air/water interface. Finally, we will provide an account of applications of thermally treated colloidal particles and assemblies.

2. Basic concepts

In this section, we will introduce the basic definitions concerning the physicochemical properties of interest for thermal treatments, with specific focus on polymer and silica particles.

2.1. Polymer particles

Polymers can be classified according to their character into amorphous and crystalline [34]. The former are typically characterized by their glass transition temperature, the latter by both melting and glass transition temperatures [34]. As crystallization is never complete, the so-called crystalline polymers are virtually semi-crystalline ones [34]. In fact, almost all crystallizable polymers are considered to be semi-crystalline because they contain significant fractions of poorly ordered, amorphous chains [35]. Polystyrene, polymethylmethacrylate, styrene-acrylonitrile copolymers, acrylonitrile-butadiene-styrene copolymers, poly(vinyl chloride), cellulose acetates, polycarbonates, phenylene oxide-based resins are examples of amorphous polymers [34].

2.1.1. Glass transition temperature and melting temperature

Melting temperature T_m and glass transition temperature T_g are characteristic constants of polymers [34]. One often talks about melting ranges and glass transition ranges [34,36].

Warming of glassy amorphous materials converts them into rubbery liquids and eventually into viscous liquids [35]. An ordinarily glassy polymer like polystyrene (PS) is transformed into a rubbery liquid upon warming to a high enough temperature [35]. The glass transition of amorphous polymers or amorphous domains of semi-crystalline thermoplastics marks the change from a glassy to a rubbery state [36]. At temperatures $T > T_g$, the mobility of the chain segments is greater than it is below it (where it is said to be “frozen”) [36]. The material undergoes a noticeable variation in volume [36]. This represents a relaxation transition and not a genuine phase transition [36]. The temperature range over which it occurs is called the glass transition range or freezing range [36]. The glass transition temperature T_g is defined, by convention, as the temperature at which half of the change in specific heat capacity has occurred [36]. For techniques to determine and model T_g, the reader is referred to [37].

Melting is a change from a solid, crystalline state into an amorphous liquid state, occurring without loss of mass or chemical change [36]. Differently from metals, whose melting point represents the equilibrium temperature between solid and liquid, semicrystalline polymers melt over a relatively broad range [36]. Similarly to the glass transition range, the melting range is fundamentally governed by the structure of the polymers [36]. Semi-crystalline polymers consist of crystallites of different lamellar thicknesses and degree of perfection; hence, the melting curve reflects this non-uniform structure [36]. The experimental melting temperature T_m is the temperature at which all crystallites have definitely melted and the crystalline order has been destroyed [36].

The concepts of T_g and T_m have been extensively explored in literature [34–45]. The reader is referred to Appendix A for a more detailed discussion about glass transition temperature and melting temperature.

2.1.2. Values of characteristic temperatures

Table 1 reports the values of T_g and T_m for different polymers [34,35]. Observed T_g vary between −123 °C for poly(dimethyl siloxane)-PDMS and 273 °C for polyhydantoin polymers used as wire enamels and reach even higher values for other polymers whose main chain consists to a great extent of aromatic structures [35]. Please note that the values reported in the table are only indicative, because, as described in Appendix B, T_g and T_m are affected by several parameters, which explains the variability in the values reported in literature. Hence, the values of temperature reported in the following paragraphs may differ from those reported in this table. In fact, T_g is influenced by several factors, including polymer structure, pressure, presence of additives, solvent residues, moisture, etc. A more extensive discussion of the factors affecting characteristic temperatures is given in Appendix B.

2.2. Silica particles

In addition to polymers, colloidal particles made up of different materials can undergo thermal treatments. One notable example of

Table 1
– Glass transition temperature T_g and melting temperature T_m of selected polymers [34,35]

Polymer	T_g [°C]	T_m [°C]
Ref. [35]		
Poly(dimethyl siloxane)	−127	–
Polyethylene	−120	140
Polypropylene (isotactic)	−8	176
Poly(1-butene) (isotactic)	−24	132
Polyisobutene	−73	–
Poly(4-methyl-1-pentene)	29	250
cis-1,4-polybutadiene	−102	–
cis-1,4-polyisoprene	−73	–
Polystyrene (atactic)	100	–
Poly(alpha-methyl styrene)	168	–
Poly(methyl acrylate)	10	–
Poly(ethyl acrylate)	−24	–
Poly(propyl acrylate)	−37	–
Poly(phenyl acrylate)	57	–
Poly(methyl methacrylate) (atactic)	105	–
Poly(ethyl methacrylate)	65	–
Poly(propyl methacrylate)	35	–
Poly(*n*-butyl methacrylate)	21	–
Poly(*n*-hexyl methacrylate)	−5	–
Poly(phenyl methacrylate)	110	–
Poly(acrylic acid)	106	–
Polyacrylonitrile	97	–
Poly(vinyl chloride) (conventional)	87	–
Poly(vinyl fluoride)	41	200
Poly(vinylidene chloride)	−18	200
Poly(vinyl acetate)	32	–
Poly(vinyl alcohol)	85	–
Polycarbonate of bisphenol A	157	–
Poly(ethyleneterephtalate) (unoriented)	69	267
Poly(*p*-xylene)	–	375
Ref. [34]		
Polyacrylonitrile	100	320
Polyamide 6	40	220
Polyamide 6, 6	50	255
Polyamide 6, 10	46	226
Polyamide 11	–	186
Polybutadiene	−86	−20
Polycarbonate	155	235
Polyisobutylene	−73	44
Polyethylene, low density	−100	120
Polyethylene, high density	−70	135
Polypropylene	−30	165
Poly(butylene terephtalate)	65	220
Poly(ethylene terephtalate)	69	256
Poly(ethylene vinyl acetate)	−20 to +20 (depending on ethylene content)	40–100 (depending on ethylene content)
Poly(fluoroethylene propylene)	–	280
Polytetrafluoroethylene	−20	327
Poly(vinyl acetate)	30	–
Poly(vinyl chloride)	85	190
Poly(vinylidene chloride)	−17	–
Poly(vinylidene fluoride)	–	178

utmost interest for nanotechnological applications of colloidal particles is given by silica.

Silica colloids represent one of the best characterized inorganic systems that have been manufactured as monodispersed samples, also in large quantities [2]. The concentration of hydroxyl groups and the dehydration (i.e. the removal of physically adsorbed water), dehydroxylation (i.e. the removal of silanol groups from the silica surface) and rehydroxylation (i.e. the restoration of the hydroxyl covering) of the silica surface play an important role during thermal treatments [46].

Most of the following groups involving Si − O bonds either as silanols or as siloxanes have been identified on the surface or in the internal structure of amorphous silica (Fig. 1(a)) [46–49]:

- single silanol groups, also known as free or isolated or single silanols (i.e. located at a distance sufficiently far from neighbouring hydroxyl groups to prevent hydrogen bonding) ≡ SiOH containing isolated free OH groups; they are indicated as Q^3 in nuclear magnetic resonance (NMR) Q^n notation, where n equals the number of bridging oxygens (SiO −) bonded to the central silicon atom;
- silanediol groups, also called geminal silanols = $Si(OH)_2$ containing geminal free OH groups; they are designated as Q^2 in NMR;
- silanetriols $-Si(OH)_3$ postulated even if real existence is not yet generally accepted; they are designated as Q^1 in NMR;

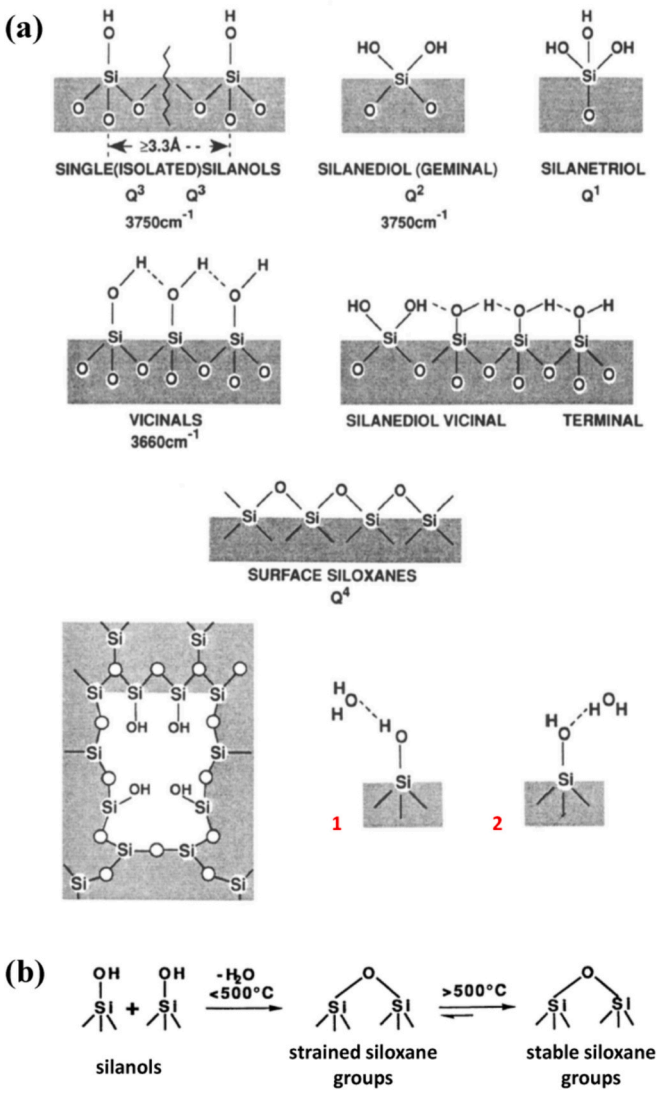

Fig. 1. - Fundamental properties of silica: (a) silanol groups and siloxane bridges on the surface of colloidal silica and corresponding Q^n notation used in NMR (first, second and third row); internal silanol groups where the fourth oxygen is above or below the plane of the paper and two basic types of orientation of the water molecule with respect to the silanol group on the silica surface; in type 1, the oxygen atom in the H_2O molecule is bonded to the hydrogen atom of the ≡ SiOH group; in type 2, the hydrogen atom in the H_2O molecule is bonded to the hydrogen atom of the ≡ SiOH group (fourth row) (reprinted with permission from [47]. Copyright 1994 American Chemical Society); (b) condensation of surface and internal silanol groups to siloxane bridges (reprinted with permission from [47]. Copyright 1994 American Chemical Society).

- hydrogen-bonded vicinal silanols (single or geminal), including terminal groups, i.e. containing vicinal, or bridged, or OH groups bound through the hydrogen bond (H-bonded single silanols, H-bonded geminals and their H-bonded combinations);
- internal silanol groups involving OH groups, sometimes classified as structurally bound water, present within colloidal silica particles at various concentration levels depending on the synthesis temperature and other variables;
- strained and stable siloxane bridges and rings or $\equiv Si-O-Si\equiv$ bridges with oxygen atoms on the surface; surface siloxanes are indicated as Q^4 in NMR;
- physically adsorbed H_2O hydrogen-bonded to all types of surface silanol groups.

Surface and internal silanol groups may condense to form siloxane bridges: strained siloxane bridges are formed on the hydroxylated silica surface by thermally induced condensation of hydroxyl groups up to about 500 °C; at higher temperatures, the strained siloxane groups are converted into stable siloxane groups [47] (Fig. 1(b)). Strained siloxane bridges undergo complete rehydroxylation upon exposure to water, while rehydroxylation of stable siloxane bridges also occurs but at a slower rate [47].

The structure of silica surfaces as synthesized is strongly dependent on the preparation method [47]. At a sufficient surface concentration, the OH groups make the silica surface hydrophilic, whereas predominance of siloxane bridges on the silica surface makes the surface hydrophobic [47].

Of particular interest are silanol groups, because the surface of the as-synthesized silica colloids is often terminated with silanol groups originated during the condensation-polymerization of $Si(OH)_4$ or as a result of rehydroxylation of thermally dehydroxylated silica when treated with water or aqueous solutions; such groups can ionize to generate a negatively charged interface at pH values higher than 7 [2,47]. The silica surface OH groups are the main centers of physical adsorption (physisorption) of water molecules: water can be associated by hydrogen bonds to any type of surface silanols and sometimes to internal silanol groups [47]. Pristine samples of silica colloids undergo a series of changes upon thermal treatment at elevated temperatures [2]. Dehydration of the silica surface (i.e. removal of physisorbed water) occurs at relatively low temperatures; the threshold temperature corresponding to complete dehydration and beginning of dehydroxylation by condensation of surface OH groups is around 190 °C [47]. The concentration of OH groups on the surface decreases monotonically with increasing temperature when silica particles are heated under vacuum [47]. The physisorbed water is released first at about 150 °C [2,47]. By about 450–500 °C all the vicinal groups condense, yielding water vapour, and only single, geminal and terminal silanol groups and strained siloxane bridges remain [47]. The estimated ratio of single to geminal silanol groups on the surface is believed not to change with temperature, at least to about 800 °C [47]. Internal silanols begin to condense at about 600–800 °C and in some cases at lower temperatures [47]; in [49], slow removal of internal water was observed to occur at 200–400 °C, while the rate of removal increased at 400–600 °C; internal water was found to be removed by the transport of water molecules (through the solid material or ultramicropores) from the bulk to the surface; the diffusion rate increases with temperature, giving rise to an increase in removal of internal water; at higher temperatures, up to about 1000–1100 °C, only isolated (single) silanol groups remain on the silica surface [47]. Finally, particles start to fuse into aggregates when the temperature is raised above the glass transition temperature of amorphous silica (approximately 800 °C) [2].

The concentration of silanol groups on the silica surface expressed in number of OH groups per square nanometers α_{OH} is often called the silanol number [46–48]. Similarly a degree of surface coverage with OH groups θ_{OH} can be defined [46]. Table 2 shows typical values of such parameters for variable temperature. Fig. 2 reports α_{OH}, γ_{OH} (internal water loss) and δ_{OH} (total water loss) expressed as the number of OH groups per unit area of SiO_2 surface as a function of temperature.

2.3. Thermal annealing and sintering

Two main concepts of interest within the framework of thermal treatments of colloidal particles are thermal annealing and sintering.

Thermal annealing can be defined as a process where a material

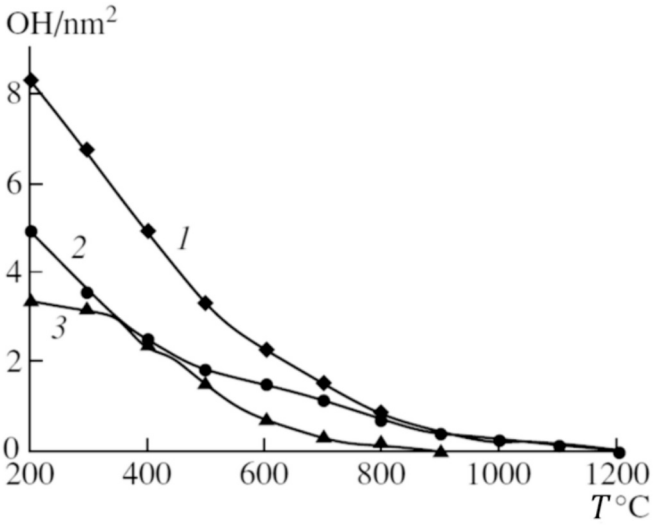

Fig. 2. - Concentration of silanol groups on the silica surface: δ_{OH} (curve 1), α_{OH} (curve 2) and γ_{OH} (curve 3) as a function of temperature (reprinted by permission from Springer Nature: [49], Copyright 2006, reproduced with permission from SNCSC).

Table 2
– Parameters characterizing the surface concentration of the different types of surface groups [46].

Temperature of vacuum treatment T [°C]	α_{OH}(total) [OH nm^{-2}]	$\alpha_{OH,I}$ (isolated) [OH nm^{-2}]	$\alpha_{OH,G}$ (geminal) [OH nm^{-2}]	$\alpha_{OH,V}$ (vicinal) [OH nm^{-2}]	θ_{OH} (total)	$\theta_{OH,I}$(isolated)	$\theta_{OH,G}$ (geminal)	$\theta_{OH,V}$ (vicinal)
180–200	4.60	1.20	0.60	2.80	1.00	0.26	0.13	0.61
300	3.55	1.65	0.50	1.40	0.77	0.36	0.11	0.30
400	2.35	2.05	0.30	0	0.51	0.45	0.06	0
500	1.80	1.55	0.25	0	0.39	0.34	0.05	0
600	1.50	1.30	0.20	0	0.33	0.29	0.04	0
700	1.15	0.90	0.25	0	0.25	0.20	0.05	0
800	0.70	0.60	0.10	0	0.15	0.13	0.02	0
900	0.40	0.40	0	0	0.09	0.09	0	0
1000	0.25	0.25	0	0	0.05	0.05	0	0
1100	0.15	0.15	0	0	0.03	0.03	0	0
1200	0	0	0	0	0	0	0	0

undergoes a heat treatment at a certain temperature, is kept at that temperature for a definite time and is subsequently cooled to room temperature (RT) in order to alter the material properties; hence, the annealing process is dependent on both time and temperature [50].

The annealing of semi-crystalline polymers may influence the crystal structure, the degree of crystallinity, the perfection of the crystals, the orientation of both crystalline and amorphous phases, their contiguous structural morphology and the number of tie chains between the crystallites [50]. Morphological changes can also occur in bulk-crystallized samples upon annealing, as well as polymorphism in crystalline polymers, i.e. the transformation of one crystalline form into another one [50].

Thermal annealing can be exploited for the stabilization of glassy polymers via the densification of their polymer chains [50]. For amorphous polymers, the thermal treatment can play a major role in changing the morphology [50]. In fact, if the temperature is lower than the glass transition temperature T_g, the polymer chains are mainly immobile and, consequently, the existing morphology is mantained; however, if the annealing temperature is greater than T_g, the polymer chains will relax; hence, the morphology can be modified upon annealing at a temperature higher than T_g, with variations in the physical properties of the polymers [50].

It is noteworthy to observe that material characteristics, e.g. bulk or particle, influence their thermal properties. For example, submicrometer PS particles exhibit physical properties not inherent in the bulk because of a higher surface area that subsequently lowers their T_g and melting point [51]. In [52], suppression of T_g in comparison to bulk PS has been investigated by fast scanning calorimetry (FSC) for PS particles of diameter between 230 and 500 nm, suggesting its decrease for decreasing diameter. In other works, dependence of T_g on film thickness had been investigated, for instance for PS films [53].

Another concept of interest is sintering. Traditionally, the term "sintering" refers to joining mechanisms between two particles or grains [54]. Developed for thermoplastic polymer powders, as we will see, it can be recalled when considering heating at elevated temperatures of adjacent polymer colloidal particles. When the temperature attains the softening point or melting point of the powder material, a sintering neck is formed between the particles due to the flow of the powder material and then aggregation occurs: the process of formation of the sintering neck and the agglomeration of the powder particles is referred to as sintering [55]. When the polymer temperature reaches its agglomeration temperature T_c (which is related to T_m for semi-crystalline polymers and to T_g for amorphous polymers), the polymer molecular chains or segments begin to move freely [55]. In order to reduce the surface energy of the powder material, the powder particles form sintering necks between them (a phenomenon driven by the surface tension) even until fusion [55]. The process can be characterized via the definition of a sintering temperature window included between a softening point T_s of the powder (at which the powder particles begin to adhere to each other and cannot flow freely) and agglomeration temperature T_c (at which complete agglomeration occurs) [55]. The sintering temperature window is determined by the thermal properties of the material itself [55]. A wider sintering temperature window implies an easier control over sintering and lower sensitivity to warping deformation [55]. In addition, for amorphous polymers, one has $T_s = T_g$ and $T_c > T_g$ (for example T_c is approximately 116 °C for polystyrene), while for crystalline polymers the sintering temperature window lies between the start temperature of recrystallization and the start temperature of melting [55]. The differences in temperatures for sintering for amorphous and crystalline polymers as well as the difference in viscosity (much higher for amorphous polymers at T_g than for crystalline polymers at T_m) explains the large difference in the sintering rate and in the density of the sintered parts [55].

3. Models of colloidal particle shaping under thermal treatment

In this section we will introduce the theoretical background and models describing morphological changes induced by thermal treatment of polymer and silica particles.

3.1. Polymer particles

Let us consider first the case of polymers. As a preamble, we have to say that we will take into account thermal treatments of polymer particles close to T_g.

A first distinction needs to be traced between wet and dry sintering. Fig. 3(a) illustrates the process of film formation starting from a colloidal suspension to full coalescence of particles and film formation. The film formation process from polymer colloidal particles from the evaporation of an aqueous suspension is articulated into the following steps [56–61]:

- stage I: the aqueous colloidal suspension is allowed to evaporate; particle self-assemble during the evaporation of water; if particles are sufficiently monodispersed, they assemble into a colloidal crystal;
- stage II: it occurs only above the minimum film forming temperature (MFFT), which is strongly related to T_g of the polymer, being often close to T_g; exceeding T_g leads to the softening of the particles, allowing them to deform into polyhedrons (dodecahedrons for 3D assemblies), where each facet is in full contact to a facet of the neighbouring particles; this results in optically clear polymer films due to the loss of the refractive index contrast within the structure; possible causes of particle deformation include air/water, water/polymer or polymer/air interfacial tensions, osmotic forces or surface adhesive forces;
- stage III: polymer diffusion across the particle-particle interfaces takes place, yielding a continuous polymer film.

Particle self-assembly by evaporation from an aqueous suspension is carried out at a certain temperature, typically room temperature. The main driving factor for either wet sintering or dry sintering processes resides in the glass transition temperature of the particle polymer material relative to the temperature at which evaporation of the particle suspension is carried out (the drying temperature, typically room temperature). Particles with T_g above the drying temperature behave as hard particles, whereas particles with T_g below the drying temperature behave as soft particles [58,62,63]. One can distinguish between two cases [56–59,64]:

- if the MFFT (which, as said, is close to T_g) is below the drying temperature, stages II and III occur already during water evaporation and one speaks about wet sintering; for example, for applications such as paints, the MFFT is below the drying temperature, resulting in wet sintering of the particles as the water evaporates; this means that particle deformation and inter-diffusion in stages II and III occur for soft latex particles, where the applied temperature is maintained above the polymer glass transition temperature (T_g); for lower applied temperatures, a powdery and brittle film is formed;
- if the particles possess a T_g above drying temperature, the polymer is still in its glassy state and deformation of the particles is hampered

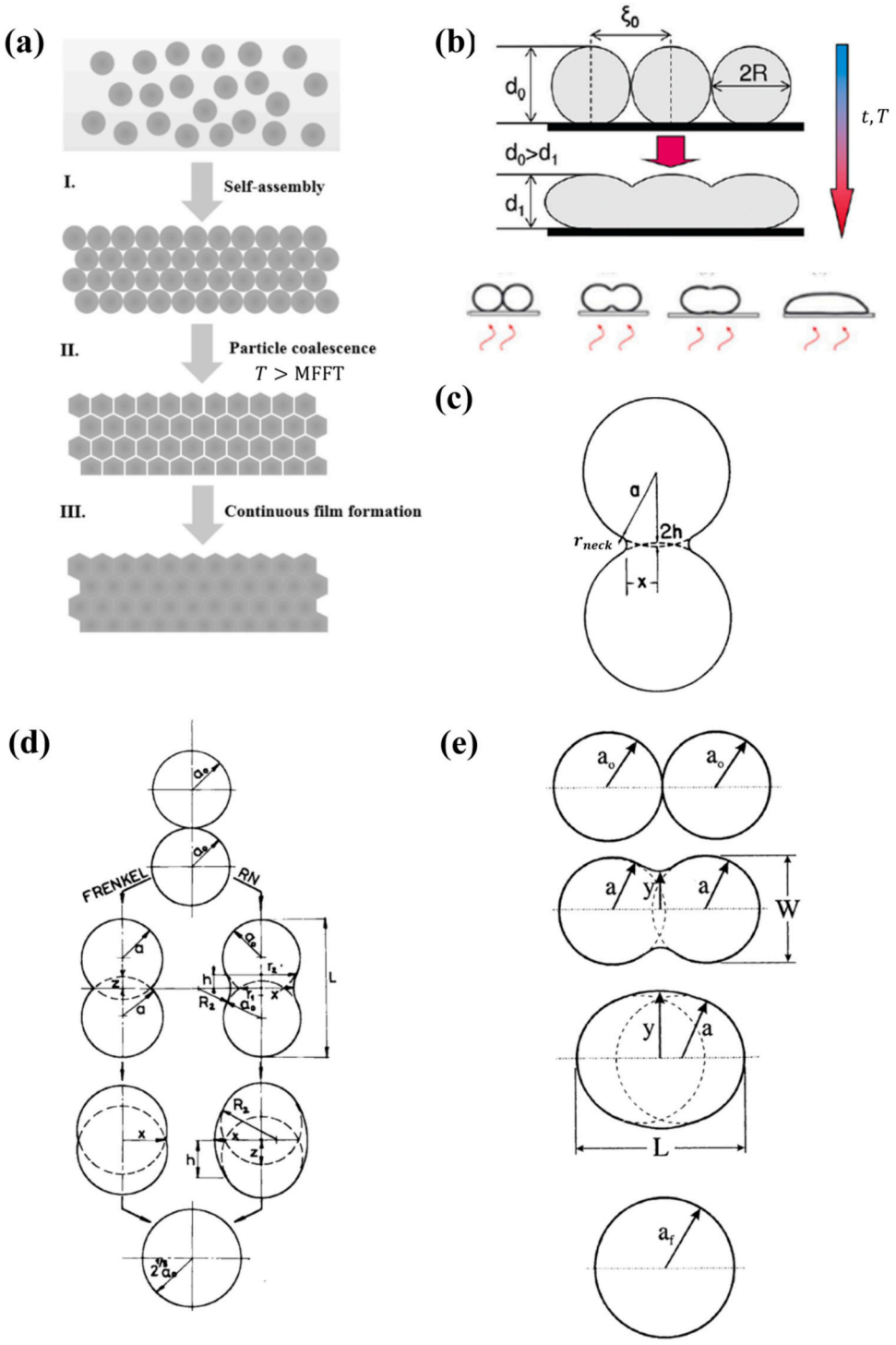

Fig. 3. - Polymer colloidal particle shaping under treatment: (a) sketch of colloidal film formation process starting from a colloidal suspension to full coalescence of particles and film formation (reproduced from Ref. [56] with permission from the PCCP Owner Societies; https://pubs.rsc.org/en/content/articlelanding/2017/cp/c7cp01994g); (b) sketch of the effect of thermal treatment close to T_g (reprinted with permission from [123]. Copyright 2012 American Chemical Society; reproduced from [76], with permission, copyright 2010, John Wiley & Sons); (c) geometry of a sintered contact ([84], reprinted by permission of Informa UK Limited, trading as Taylor & Francis Group, http://www.tandfonline.com on behalf of Institute of Materials, Minerals and Mining and ASM International); (d) two geometrical models describing sintering of a colloidal particle pair: Frenkel's sharp corner model (on the left) and round neck model (on the right) (reproduced from [77], with permission, copyright 1981, John Wiley & Sons); (e) sketch of the sintering sequence for two particles showing all the geometrical quantities involved (reproduced from [87], with permission, copyright 1996, John Wiley & Sons).

during water evaporation, meaning that stages II and III do not occur; nonetheless, after the film dries well below the polymer glass transition temperature (in order to negate the possibility of particle deformation), the temperature can be raised; thermal treatment above its T_g entails dry sintering of the particles, with the occurrence of stages II and III; in case of hard particles with T_g above drying temperature undergoing annealing, the process proceeds via void closure and, after disappearance of the voids, by inter-diffusion of

polymer chains, followed by healing at the polymer-polymer interface.

The closure of the porosity and the formation of mutual full contact areas is driven by the following factors [56]:

1. the viscosity of the polymer at the specific temperature,
2. the surface tension between the water and the polymer in case of wet particle sintering or the one between air and polymer in case of dry particle sintering.

In addition, particle deformation in stage II is also size-dependent [56,60]. Moreover, the MFFT depends on particle composition, size and morphology [65].

Hence, for low-T_g soft particles (with T_g below room temperature, e.g. poly-(butyl methacrylate)-PBMA), the forces accompanying evaporation of the solvent (e.g. water) in a colloidal dispersion are sufficient to compress and deform particles into a transparent, void-free film (a film formed by the coalescence of sub-micrometer soft polymer particles with low T_g, i.e. by compaction, deformation, cohesion and polymer chain inter-diffusion) [58,62,63,66–69]. High-T_g hard particles (e.g. from PMMA or PS) remain discrete and undeformed during the evaporation of an aqueous suspension, but their mechanical properties can be tailored after solvent evaporation by sintering, resulting first in void closure and then to inter-diffusion of chains across particle-particle boundaries [58,62,63,66–69]. As discussed in Appendix B, in case of particles made up of block copolymers, T_g and, hence, sintering, can be controlled by the relative amount of the different components, for example, for poly (methyl methacrylate / butyl acrylate) (p-MMA/BA) latexes, T_g and the MFFT values increase as the MMA weight ratio used in the formulation increases [61]. More complex behaviours can be obtained in multi-component particles, for instance core/shell particles made up of two different polymers (including a low-T_g and a high-T_g polymer), with possible phase separation and self-stratification in polymer films or formation of zebra stripe structures [64]. Wet and dry sintering of polymer particles have been investigated using different techniques, such as small-angle neutron scattering (SANS) [70,71], small-angle X-ray scattering (SAXS) [72], grazing incidence ultrasmall-angle X-ray scattering (GIUSAXS) [73], environmental scanning electron microscopy (ESEM) [61], atomic force microscopy (AFM) [73,74], NMR [74], differential scanning calorimetry (DSC) [74], dilatometry [74], direct non-radiative energy transfer (DET) and fluorescence study of dye-labelled polymer particles [65,68,75] or ultraviolet (UV)/visible spectroscopy [58,63]. We will consider mainly dry sintering processes carried out on polymer particle films already assembled by any self-assembly technique whatsoever.

Fig. 3(b) sketches the effect of thermal treatment close to T_g of the polymer in the plane orthogonal to the substrate on which polymer particles are placed. When neighbouring polymer particles undergo thermal treatment above T_g, two different phenomena can occur [76]:

- coalescence, i.e. adhesion and inter-diffusion of particles;
- densification, due to the reduction of the inter-space distance between the particles due to the inter-diffusion.

Sintering is a common term to describe high temperature coalescence of solid particles such as metals, ceramics and polymers [77,78]. High temperature sintering can occur with or without compaction or decrease of total volume [76,79–81]. The main driving force for the sintering process for polymer particles is their surface tension [77]. Additional parameters governing the rates of sintering of polymeric spherical particles are their size, viscosity and gravity [77].

Sintering of amorphous polymer particles above their glass transition temperature is a slow coalescence process in which surface tension is the main driving force, tending to decrease the total surface area, resisted by the polymer viscosity [82]. In fact, amorphous polymer particles contacting each other at a temperature above their glass transition temperature tend to decrease their total surface area by coalescence [78,80,81]. The shape and, consequently, the boundaries of the coalescing particles change with time [82]. Different theoretical models (analytical, empirical or numerical) have been developed to describe sintering of particles.

Particles in contact with each other at elevated temperatures will tend to decrease their total surface energy by coalescence; this process can be approximated by a neck forming between two spheres [82,83]. If we consider particles of radius a, a neck of radius x will start forming between adjacent particles (Fig. 3(c)). Generally speaking, three stages can be identified during sintering [84]:

- early stage of neck growth: neck growth proceeds according to an exponential time law; particles still remain as individuals, since it is still not possible for strong grain growth to occur beyond the original particle; the tensile stresses resulting from surface tension preserve the grain boundaries between two adjacent particles in the plane of contact, but the occasional formation of new grains is possible;
- stage of densification and grain growth: when the x/a ratio exceeds a certain value after intensified neck growth, the separate particles begin to lose their identity; most of the shrinkage occurs at this stage, where a coherent network of pores is formed;
- final stage with closed pore spaces: the isolated pores become increasingly spheroidised; further densification still proceeds slowly, thereby making it often impossible to define whether it has come to an end, e.g. whether the residual porosity is permanent.

Quite often (for instance, at lower temperatures) the process is limited to neck growth, i.e. the first stage is essentially the only one observed [84].

The rate of increase of neck radius x formed between two spheres of radius a can be described by a general equation of the form [81,84]:

$$\left(\frac{x}{a}\right)^n = \frac{F(T)}{a^m} t \tag{1}$$

where t is the sintering time, $F(T)$ is a function of temperature T characteristic of the type of flow predominant in the process, n and m are exponents dependent on the process; for example [81,85]:

- $n = 2$ for viscous flow and, in particular, for viscous Newtonian flow $n = 2$ and $m = 1$;
- $n = 3$ for evaporation-condensation;
- $n = 5$ and $m = 3$ for volume diffusion;
- $n = 7$ and $m = 4$ for surface diffusion.

We observe that some of these models and exponents have been put in question and contested [84].

These flows are caused by the capillary tensile stress in the neck area whose value can be approximately expressed by the eq. (2) [81]:

$$\sigma = \frac{\gamma}{r_{neck}} \tag{2}$$

where r_{neck} is the radius of neck curvature and γ is the surface tension of the solid, considered as isotropic.

The evaporation-condensation mechanism involves the evaporation of the atoms from the convex parts of the system and condensation on the concave areas, or in the “neck”, and may occur if the vapour pressure of the material is high [85]. The distinct difference between the mechanism of viscous flow and that of volume diffusion (even if the former may also be caused by diffusion) lies in the fact that, for the occurrence of viscous flow, stress is needed, which may be produced by surface tension; on the other hand, in the case of volume diffusion flow, such a stress is not necessary [85]. While metallic and ceramic materials sinter

by volume and surface diffusion, organic molecules and especially macromolecules sinter by flow mechanisms since the activation energy for diffusion of the organic molecules is too high; hence, viscous flow is the most important transport mechanism for polymers [86,87].

One of the first models of particle sintering by Newtonian viscous flow is the Frenkel's model, which can be formulated as [80,81,83,85–91]:

$$\frac{x^2}{a} = \frac{3\gamma}{2\eta} t \tag{3}$$

where η is the viscosity; this equation represents a specific case of eq. (1). This equation can also be written as [79]:

$$x^2 = Kt \tag{4}$$

where K includes the contribution of a, γ, η. This expression describes the rate of coalescence of adjacent spheres under the action of surface tension, the thermodynamic premise being that a system left to itself would lower its free energy by decreasing its total surface [89]. Corrections to this model have been proposed, for example the Frenkel/Eshelby's model in which the factor $\frac{3}{2}$ of eq. (3) is missing [87] or other modified models [92]. Frenkel's model assumes that coalescence takes place by mutual penetration of the particle pair, one to the other, thereby forming a sharp neck at the circular area of contact (Fig. 3(d)) [77]. In reality, the sintering of two particles can be schematically represented as in Fig. 3 (e), which shows that the sintering process over time can be characterized via the particle radius a_t (which progressively departs from the initial particle radius a for longer treatments), the neck radius x, the length L and the width W of the sintering particles, the final particle radius a_f [87]. The particle's penetration is accompanied by neck build-up where the external contour in the figure consists of circular arcs making tangential contact with each other with no sharp corners [77]. The system thus tends to form spherical shapes of minimum surface area eventually leading to a single sphere from two spheres [77]. The validity of Frenkel's model is limited to Newtonian flow and only to the early stages of sintering, when the particle diameter remains relatively constant ($a_t = a$) [77,87].

Experimental investigations have been carried out on polymer particles, with results that are often contradictory. For example, a Newtonian sintering behaviour has been reported over a wide temperature range for both PS and PMMA particle pairs and trimers, showing a fundamentally good agreement with Frenkel's model (Fig. 4) [78–80,82]. In other cases, discrepancies with the Frenkel's model have been observed, for example in [81], where, for PMMA particles, a variation in the polymer rheology was found changing from pseudoplastic behaviour to dilatant one in the temperature range of 150 °C to 207 °C (in particular being pseudoplastic at the lower temperatures and dilatant at the higher ones after passing through a certain temperature at which the behaviour is Newtonian), suggesting a non-Newtonian viscous flow [79,81,82]; the behaviour could be summarized in the following empirical Frenkel-Kuczynski equation [81,86]:

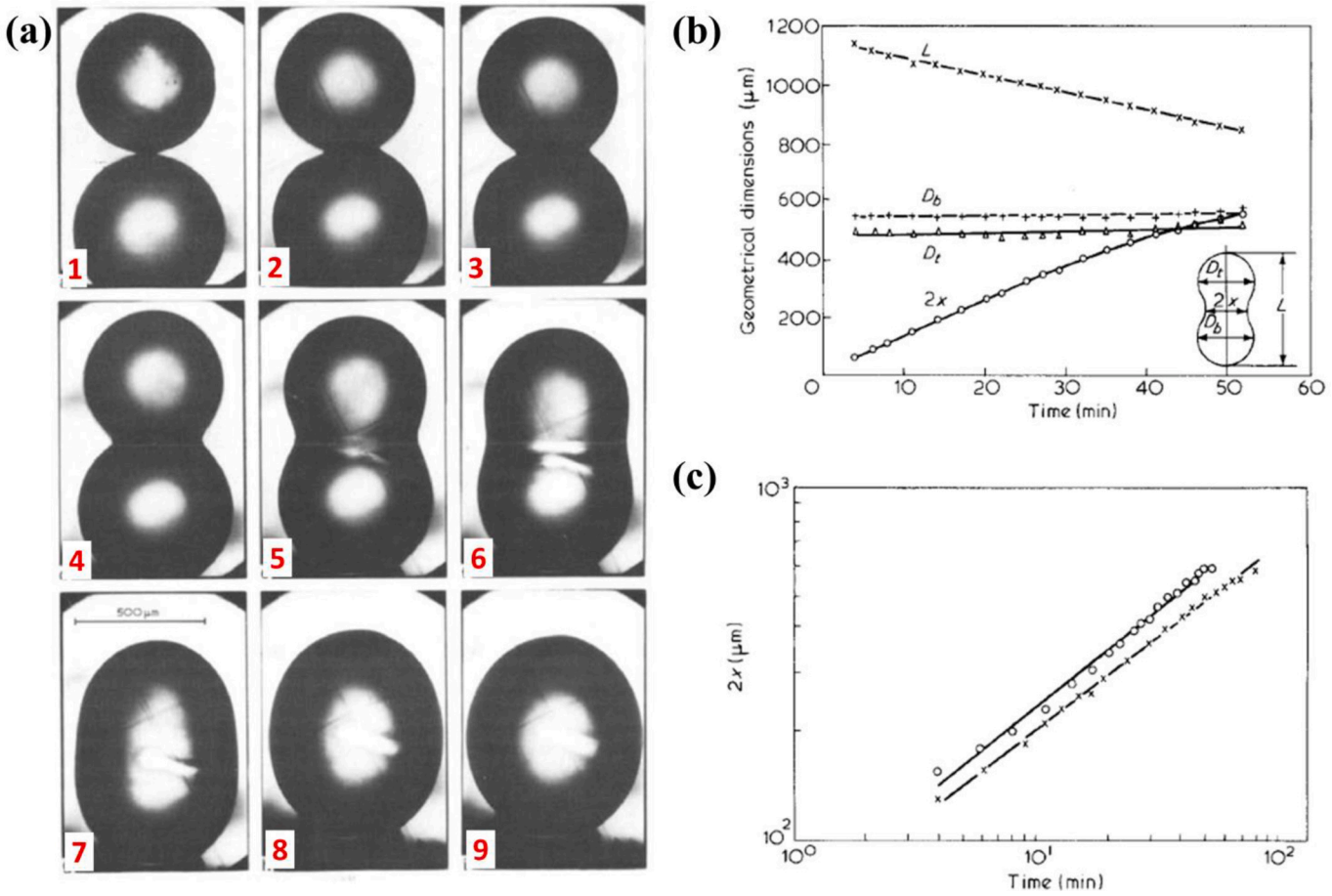

Fig. 4. - Polymer colloidal particle shaping under treatment: (a) evolution of PS particle sintering at 180 °C after (1) 0, (2) 8, (3) 14, (4) 20, (5) 32, (6) 41, (7) 55, (8) 69, (9) 79 min (reprinted from [79], Copyright 1980, with permission from Elsevier); (b) dependence of typical geometric dimensions upon sintering time for PS particles treated at 180 °C (L total length, D_b diameter of the bottom particle, D_t diameter of the top particle, $2x$ diameter of contact neck circle) (reprinted from [79], Copyright 1980, with permission from Elsevier); (c) linear dependence of neck size (log$2x$) versus time (log$t$) for PS particles at 180 °C (circles) and PMMA particles at 200 °C (crosses) (reprinted from [79], Copyright 1980, with permission from Elsevier).

$$\left(\frac{x^2}{a^{1.02}}\right)^p = F(T)t \tag{5}$$

where $p = \frac{1}{n}$; for $n = 1$, the equation reduces to the case of Newtonian viscous flow, while, for $n > 1$, dilatant behaviour occurs. In [79], the previous equation was reformulated as a generalized Frenkel's equation of the form:

$$x^{2p} = K't \tag{6}$$

where the deviation of p from unity indicates a deviation from Frenkel's theory; the range of p values reported by [81] varies from 2.5 at 150 °C to 0.27 at 207 °C, while for [86], a significantly narrower range of p values is found from 1.12 at 175 °C to 0.55 at 203 °C. A viscoelastic mechanism especially at the lower sintering temperatures has also been found [79,89]. In particular, in [89], studies on polytetrafluoroethylene particles revealed a viscoelastic sintering, suggesting that the sintering or coalescence of polymers can be conceived in rheological terms as either viscous or viscoelastic transport or as a combination of the two mechanisms, which are not necessarily mutually exclusive and can intermingle either by change in temperature (as for PMMA) or with increasing time of sintering (as with polytetrafluoroethylene). Thermal degradation of the polymer (as for PMMA) can have a notable impact by changing the viscosity and thus requiring still further temperature- and time-dependent components in the Frenkel-Kuczynsky expression [89]. The description is complicated by the fact that the quantities present in the different models (in particular surface tension and viscosity) are temperature-dependent [80,89]. For example, the viscosity decreases significantly with temperature increase (typically described via Arrhenius equation) and the surface tension decreases linearly with temperature increase [80]. Polymer viscosity changes exponentially with temperature and a typical viscosity reduction for each 20–25 °C temperature rise would be approximately an order of magnitude; surface tensions of 26 and 24.2 dyn/cm have been reported for PS at 150 and 200 °C respectively [80].

Different models have been proposed to describe more faithfully the sintering process at least at the early stage [77,82,87,92,93]. For example, a geometrical model relating geometrical parameters between themselves (first and second principal radii of the contact neck and total height) in a two-spherical particles sintering system was also proposed; the model distinguishes the two stages of neck shape (the one in which the neck is concave, i.e. $x < a$, and the one in which the neck is convex, i.e. $x > a$, see Fig. 3(d)) to describe the experimental data covering the whole sintering range [77,82]. Other models, such as the sintered cube model, have been developed to describe sintering of a large number of particles [55].

In addition, one should bear in mind that the coalescence-sintering dynamics of two viscous spherical particles is much more complicated than the Frenkel's model and its modifications; the complicated flow patterns describing the spherical pair undergoing sintering impose also the need for numerical models [82,94–101].

For more information on this topic and for references also to specific models developed to describe the late stage of sintering, i.e. the one of pore closing, or specific cases such as laser sintering or sintering of particles of different size, the reader is referred to [80,87,91,92,94–113] and references therein. What we would like to point out here is the role of different parameters in influencing the sintering process, in particular [55]:

- surface tension: as we have seen, this is a fundamental factor driving the sintering process and determining the sintering rate of polymers; nonetheless, most polymers have relatively small surface tensions and they are very similar; hence, it is not a major factor causing a difference in sintering rate between polymers; we have previously hinted at the dependence of surface tension on temperature;
- particle size and shape: the size of the particle also affects the rate of sintering; the smaller the average particle size, the greater the sintering rate; also irregular particle shapes deviating from the spherical one or size polydispersity may affect the sintering process;
- viscosity: polymer melts are non-Newtonian fluids whose viscosity is dependent on shear rate; however, at low shear rates, non-Newtonian fluids can be approximated as Newtonian fluids; viscosity is affected by both molecular weight and temperature. As to temperature, as the temperature increases, the free volume of the melt increases and the mobility of the polymer segments increases, so that the fluidity of the polymer increases and the melt viscosity decreases exponentially; as we have previously seen, the temperature-dependence of the viscosity can be expressed via an Arrhenius law of the form:

$$\eta(T) = Ae^{-\frac{E_a}{RT}} \tag{7}$$

where E_a is the activation energy of viscous fluid flow and R is the universal gas constant. When the temperature is lowered below the temperature of viscous flow, the apparent activation energy of viscous fluid flow is no longer a constant, but increases sharply with the decrease of temperature, and the Arrhenius equation is no longer applicable. The Williams-Landel-Ferry (WLF) model can be used:

$$\log\left[\frac{\eta(T)}{\eta(T_r)}\right] = \frac{-C_1(T - T_r)}{C_2 + T - T_r} \tag{8}$$

where C_1 and C_2 are empirical parameters and one can assume $T_r = T_g$. Values that are frequently used to describe viscosity between T_g and $T_g + 100^{\circ}$C are $C_1 = 17.44$ and $C_2 = 51.6$. For most amorphous polymers, the viscosity $\eta(T_g)$ is of the order of 10^{12} Pa·s. The viscosity of the amorphous polymer decreases sharply above T_g with increasing temperature. The closer the temperature approaches T_g, the higher the sensitivity of the viscosity to temperature. Concerning the dependence on molecular weight, the following empirical relationships can be used:

$$\eta_0 = K_1\overline{M_w} \text{ if } \overline{M_w} < M_c$$

$$\eta_0 = K_2\overline{M_w}^{3.4} \text{ if } \overline{M_w} > M_c \tag{9}$$

where η_0 is the zero-shear viscosity, i.e. the viscosity for shear rate tending to zero, K_1 and K_2 are empirical constants, $\overline{M_w}$ is the weight-average molecular weight, M_c is the characteristic critical molecular weight for a given polymer. When the molecular weight is less than M_c, the zero-shear viscosity of the polymer melt is proportional to the weight-average molecular weight; when the molecular weight is greater than M_c, the zero-shear viscosity increases sharply with the increase of molecular weight and is generally proportional to the 3.4 power of the weight-average molecular weight.

3.2. Silica particles

Dehydration and dehydroxylation processes described in section 2.2 play a major role in silica and mesoporous silica particle sintering.

As we have mentioned, silica particles together with polymer particles are the most widespread building blocks for particle assemblies, especially for nanotechnological applications. In addition, mesoporous silica particles are of interest for a vast range of applications, in particular biomedical ones, including therapeutics, pharmaceuticals and diagnosis, drug delivery but also catalysis and optical applications [114–119]. They find applications also in chromatography, gas sensing, coatings in the semiconductor industry and water-repellent surfaces [119]. Mesoporous silica particles exhibit exceptionally high pore volumes (>60%) and surface areas, high thermal and chemical stabilities, as well as versatility in surface functionalization [119].

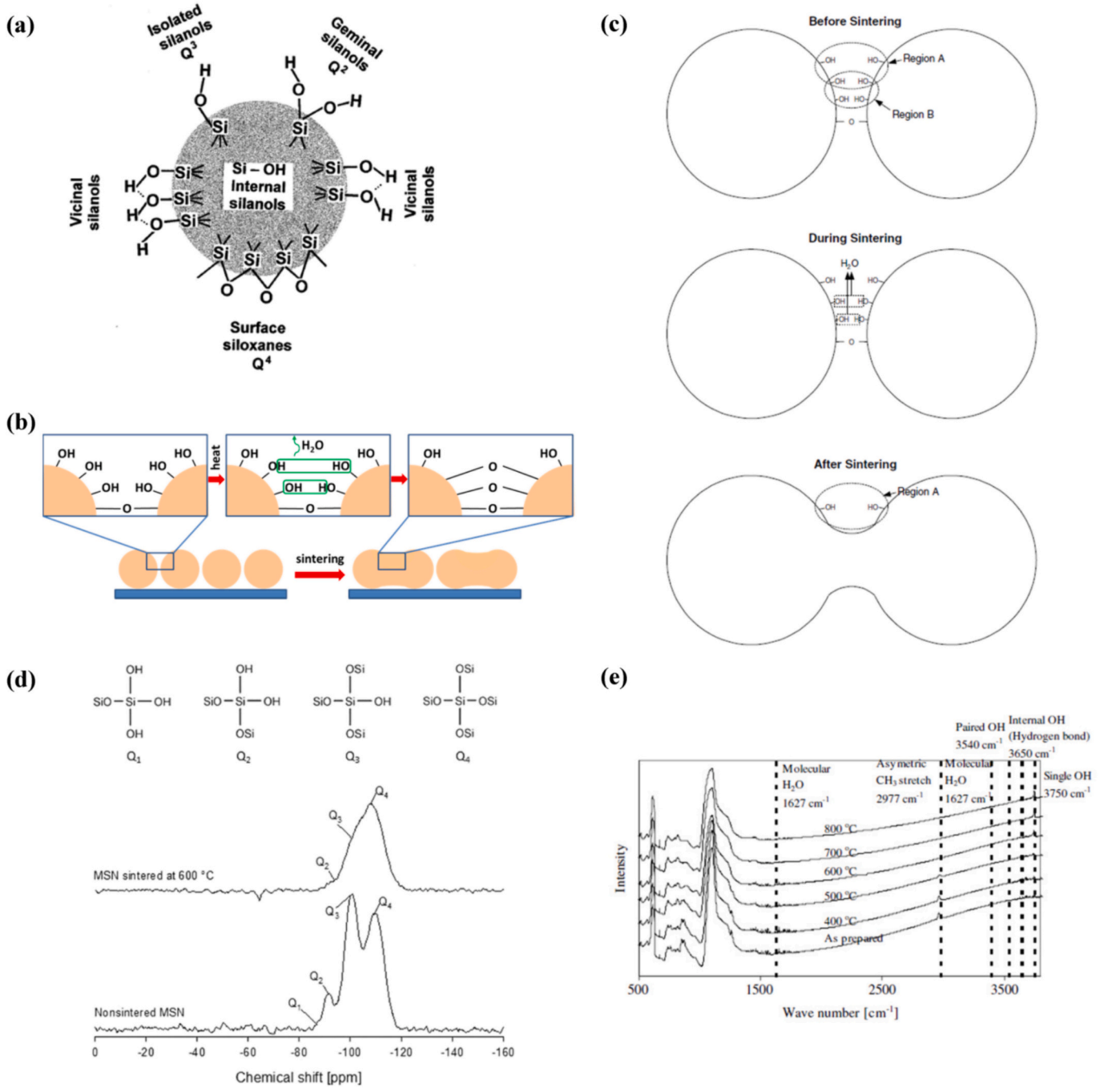

Fig. 5. - Silica colloidal particle shaping under treatment: (a) types of silanol groups and siloxane bridges on the surface of amorphous silica and internal OH groups (reprinted from [46], Copyright 2000, with permission from Elsevier); (b) schematic of bonding initiation between mesoporous silica particles (redrawn and adapted from [119]); (c) sketch of the variation in mesoporous particle structure upon sintering showing the different involved regions (reprinted from [120], Copyright 2004, with permission from Elsevier); (d) ^{29}Si solid-state magic angle spinning (MAS) NMR profiles (59.60 MHz) of nonsintered and sintered (600 °C) mesoporous silica particles (MSN) (reprinted with permission from [119]. Copyright 2015 American Chemical Society); (e) FTIR on mesoporous silica particle films as a function of temperature (reprinted from [120], Copyright 2004, with permission from Elsevier).

Fig. 5(a-c) sketch initiation of bonds between neighbouring particles upon thermal treatment. In [120] mesoporous silica films were produced using a binary solvent approach and a surface modification technique leading to the replacement of −OH groups with $-Si(CH_3)_3$ groups [120]. Before sintering, there are two regions, A and B, which contain −OH groups [120]:

- in region A, there is enough space for $-Si(CH_3)_3$ groups to reach and replace −OH groups,
- in region B, narrow necks block the access of $-Si(CH_3)_3$ groups.

During the sintering process, the −OH groups in region B are close enough to be removed by condensation reactions and neck growth results from surface tension as the driving force; only region A, the easily accessible region, remains as sintering proceeds and the neck thickens between the particles [120]. The presence of silanol groups at the surface of adjacent silica nanoparticles, is crucial to establish necks between the silica particles upon sintering [119]. In brief, the hydroxyl

groups at the surface of the particles condense, water is released and oxo bridges (Si − O − Si) allow for more consolidation and atom diffusion to occur within the silica structure [119]. Such modifications induced by thermal treatment have an impact also on the refractive index of sintered particles. Fig. 5(d-e) show the NMR profile of mesoporous silica particles before and after sintering and Fourier transform infrared (FTIR) spectra of a mesoporous silica film showing a decrease in −OH groups upon thermal treatment.

In [121], the concentration of isolated silanols has been investigated for non-porous, colloidal silica particles annealed at three different temperatures (800, 900 and 1050 °C). FTIR spectroscopy confirmed that the abundance of isolated silanols on the surface was reduced by annealing at 900 or 1050 °C; FTIR also revealed that there was markedly increased hydrogen bonding of the isolated silanols to neighbours after rehydroxylation [121]. Results were interpreted as the outcome of reduction in surface roughness for increasing temperature; a plausible interpretation of how smoothing the surface through annealing could reduce the abundance of isolated silanols and also red-shift the FTIR peaks of the isolated silanols is sketched in Fig. 6: isolated silanols are interpreted to be present at nanoscale bumps on the surface; such bumps would be the simplest way of isolating a silanol group because it raises the −OH groups above its neighbouring silanols to place it beyond the optimal hydrogen bonding distance; upon annealing, the heights of the bumps decrease and, once rehydroxylation creates neighbouring silanols, these groups are now closer to the optimal hydrogen bonding distance of the isolated silanols [121].

4. Thermal treatment of colloidal particles on a solid non-polymeric substrate

Heating of colloidal particles pre-assembled on a solid non-polymeric substrate can be applied in different ways.

For example, in [122], heating has been provided with a heating plate, via an air gun or by microwave irradiation:

- for experiments with a heating plate, the substrate was placed on a Si wafer, located on the heating plate; a thin layer of silicone oil was used to improve the thermal conductivity between the heating plate and Si wafer; the whole set-up was covered with a polymer cover with a small window to improve heat stability; temperature was monitored via a thermocouple adhered to the Si wafer and covered with a piece of aluminium foil to reduce uncontrolled fluctuations; after an annealing period, the samples were allowed to cool down [122]. Annealing periods were in the range of tens of seconds and temperatures were between 100 and 150 °C [122]. In [123], the hot plate used for annealing the samples was heated electrically and cooled with compressed air;
- the set-up to use hot air from an air gun for annealing consists of a silicon wafer support with an air gun and a room temperature argon dispenser below the wafer (providing sample cooling via heat sinking through the silicon wafer support); the hot air stream could be adjusted between 70 and 140 °C and measured via a thermocouple [122];
- in microwave heating, the samples were immersed in a liquid in a glass beaker and exposed to microwave radiation in a commercial microwave oven [122,124]. Microwave heating of the submerged sample was used up to the boiling temperature of the mixture; then sequential microwave pulses with a duration of 3 s and a period of 28 s were applied; finally, the sample was removed from the beaker and dried [122,124].

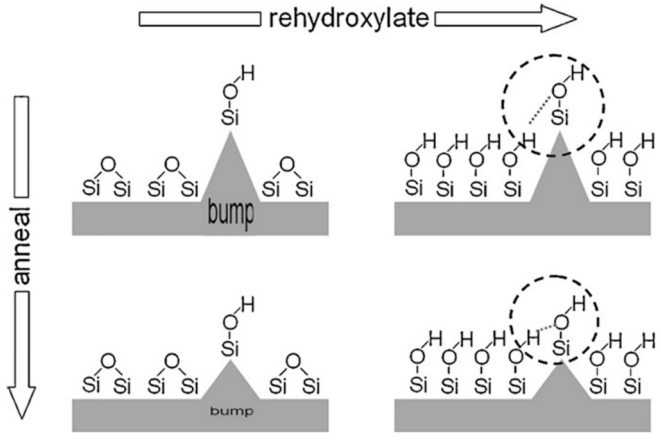

Fig. 6. - Schematic of the processes occurring upon annealing of non-porous colloidal silica particles (reprinted from [121], Copyright 2011, with permission from Elsevier).

A hot air oven or a laboratory electrical furnace have also been used [119,125,126].

Besides convection and conduction-based heating, heating based on radiation can also be adopted.

Laser sintering, which represents a commonly used additive manufacturing (AM) technique applicable to a variety of applications in fields such as the automotive industry, healthcare and consumer goods [127], represents an alternative option also for colloidal particle shaping [96,97,128–130]. This requires a more complex set-up, as, for example, the one shown in Fig. 7(a). It consists of a home-built heated sample chamber in which sintering takes place while optical imaging via the top and side is possible with two separate optical trains [128]. Laser light (visible light, e.g. 532 nm) is guided into the chamber from the top; an acousto-optic modulator (AOM) is used to pulse the laser; the chamber is built from aluminium walls fitted with heating rods on each side, as well as in the substrate [128]. A low thermal conductivity isolation around the box limits the heat loss to the environment; to avoid sintering of the polymer particles in the absence of laser light, the temperature of the sample chamber should remain sufficiently below the glass transition temperature of the polymer [128]. In addition to the possibility to perform in situ laser sintering with simultaneous visualization of the sintering dynamics by incorporation of quartz windows on the top and sides [128], other techniques can be encompassed in the set-up to study the sintering process, for example in situ X-ray and thermal characterization [128,130]. With a laser being the heat source that locally binds particles together, inhomogeneous and non-isothermal temperature profiles are obtained, which results in significant differences in the sintering process in comparison with thermal sintering in a homogeneously heated chamber [128].

Radiation from a near infrared (NIR) lamp (peak emission wavelengths between 1 and 2 μm) has also been reported for sintering of colloidal particles [131,132].

Colloidal particles in both monolayers and multilayers heated in different ways have been investigated using different characterization techniques, including scanning electron microscopy (SEM) [119,122–125,133], AFM [51,73,123,131], optical microscopy [123,133], ellipsometry [123], X-ray diffraction and SAXS [59,72,134,135], grazing incidence small-angle X-ray scattering (GISAXS) and grazing incidence transmission small-angle X-ray scattering (GTSAXS) [123,136], GIUSAXS [73], SANS [60], thermal gravimetric analysis (TGA) [72]. Such investigations aimed not only to envisage routes to deform colloidal particles and colloidal masks (e.g. by tuning the size of the interstices between neighbouring particles), but also to study the stability and integrity of colloidal particles at high temperatures.

4.1. Thermal treatment of polymer particles

Concerning polymer particles, some studies have focused on the effect of the heating system on the colloidal particle deformation. For

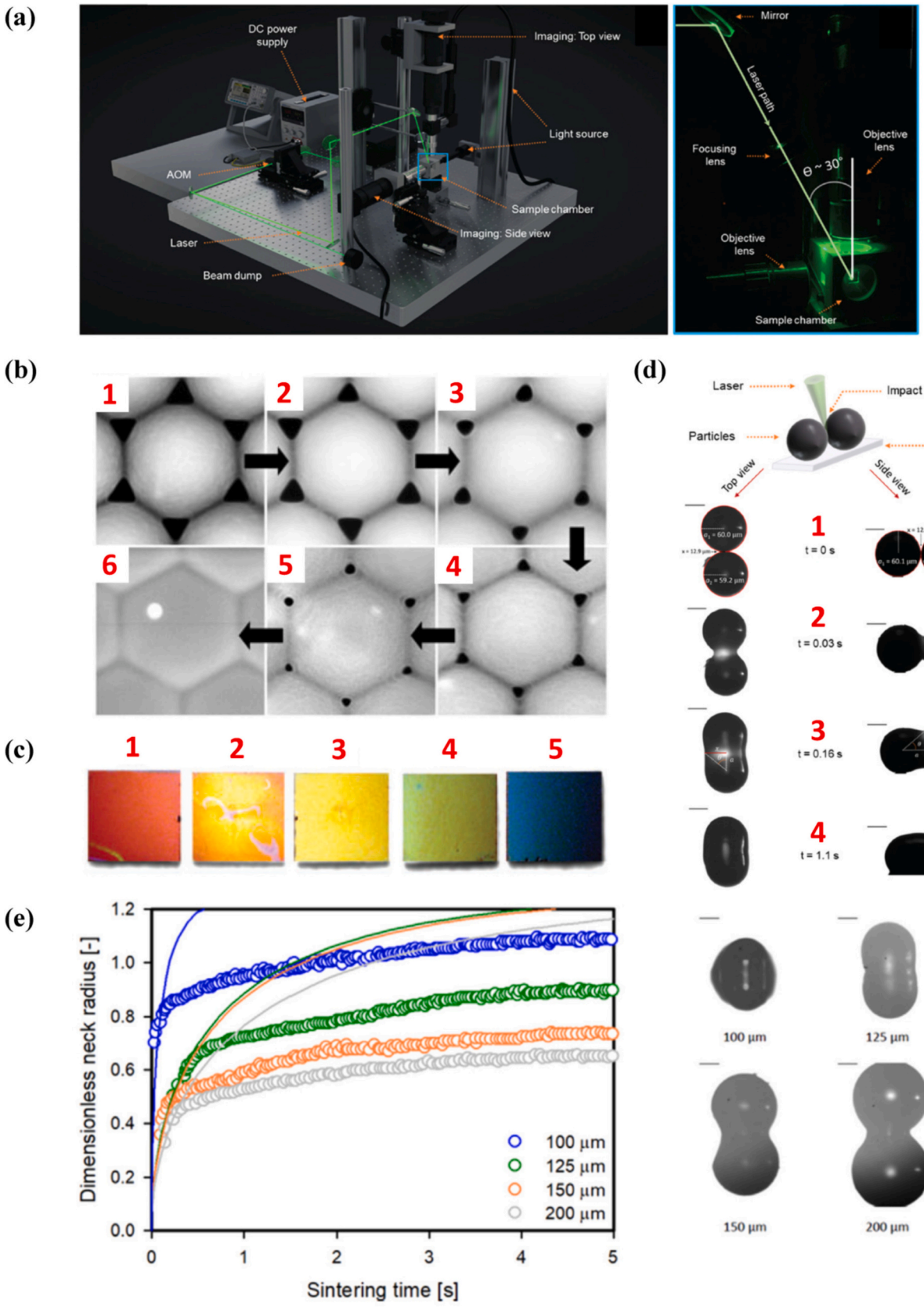

(caption on next page)

Fig. 7. - Polymer particle annealing: (a) set-up for laser sintering (rendering and close-up of the sample chamber depicting the laser path) (reproduced from Ref. [128] with permission from the Royal Society of Chemistry; https://pubs.rsc.org/en/content/articlelanding/2019/sm/c8sm02081g); (b) PS (540 nm) colloidal mask annealed in 25 ml of water/ethanol/acetone mixture with (1) 1, (2) 2, (3) 4, (4) 6, (5) 7 and (6) 10 microwave pulses (reproduced from [124], with permission, copyright 2005, John Wiley & Sons); (c) thin layer interferometric colours corresponding to different annealing levels and, hence, interstice sizes between 540 nm PS particles, in particular (1) 150 nm (not annealed) interstices, (2) 100 nm interstices, (3) 50 nm interstices, (4) 30 nm interstices and (5) completely closed interstices (reproduced from [124], with permission, copyright 2005, John Wiley & Sons); (d) typical laser sintering experiment with particle radius of 60 μm, heating chamber temperature 53 °C, pulse energy of 28 mJ and pulse duration of 800 ms (reproduced from Ref. [128] with permission from the Royal Society of Chemistry; https://pubs.rsc.org/en/content/articlelanding/2019/sm/c8sm02081g); (e) laser sintering kinetics of PA12 doublets with heating chamber temperature of 155 °C: dimensionless neck radius versus sintering time (on the left: experimental data represented as coloured circles and fits with a modified Frenkel model indicated with lines) and images of particle doublets after sintering (on the right) (reprinted from [130], Copyright 2022, with permission from Elsevier).

example, the particle modifications obtained by microwave heating have been compared with those achieved via a heating plate and via an air gun [122,124].

As to microwave heating, a PS particle monolayer (diameter 540 nm) assembled by air/water interface and transferred onto a conductive silicon substrate has been immersed in a 25 ml mixture of water/ethanol/acetone (3:1:1) [122,124]. Clean water revealed to be an inconvenient medium, since high surface tension causes mask desorption [122]. As the number of applied microwave pulses increases, the size of the interstices decreases, as revealed by both SEM micrographs and monolayer colour, which switches from red for the non-treated monolayer to orange, yellow, yellowish-green and finally blue for interstice size going from 150 nm to 100 nm, 50 nm, 30 nm until being completely closed [124] (Fig. 7(b-c)). The thickness of the sample decreases for longer annealing [124].

By studying the temporal dependence of interstice size upon annealing for 28–280 s in a microwave oven at 1200 W and 2450 MHz, a linear dependence was found; in case of annealing on a heating plate at 105 °C between 2 and 22 s, the time dependence was less regular; annealing by an air gun was performed at 125 °C for up to 30 s; similar crack densities were obtained with the different treatments [122]. The following conclusions have been drawn [124]:

- heating plate allows control over monolayer annealing via monolayer colour observation by naked eye;
- heating plate annealing can be performed also on non-conductive substrates (e.g. glass, sapphire, etc.);
- heating plate annealing implies a rapid change of particle monolayer, making the process less controllable;
- the use of a heating plate makes the annealing process less homogeneous due to temperature gradient on the sample resulting from imperfect contact between the heating plate and the substrate;
- the liquid environment of the sample in case of microwave annealing ensures very homogeneous annealing over the whole sample area with good reproducibility.

A very specific case, i.e. sintering of particles induced by radiation, has been considered too, either using a lamp or selective sintering by laser radiation.

In particular, NIR sintering of acrylate latex particles composed of a copolymer of methyl methacrylate, butyl acrylate, and methacrylic acid (in a weight ratio of 18.3:13.3:1; glass transition temperature determined by DSC to be 37.9 °C; particle diameter 420 nm) was compared with sintering in a convection oven at 60 °C [131]. In some experiments, poly(3,4-ethylene dioxythiophene)/poly(styrene sulfonate) (PEDOT/PSS), which is strongly absorbing in NIR, was added [131]. Particles were drop-cast on glass slides up to a thickness of 20 μm [131]. Film temperature during sintering was monitored via a non-contact thermometer [131]. The following conclusions were drawn [131]:

- the surface of the film treated with a convection oven was irregular, with remnants of cracks, and the film was not fully transparent because of surface roughness and wrinkling, while film heated under NIR was smoother and transparent; in case of addition of PEDOT/PSS (1 wt%), the film quality was also good, but with a bluish tint;
- the time required to reach 48 °C in a conduction oven was 10 min against 2 min for NIR sintering in case of addition of PEDOT/PSS; this result was ascribed to the fact that, with conductive heating in an oven, heat diffuses from the film surface, which defines the time dependence of the temperature; in contrast, in a radiative heating process, energy is deposited directly into the film (varying with depth according to the Lambert-Beer law);
- after just 4 min of NIR radiation, the voids were decreased in size and the particles were flattened until almost loss of particle identity after 30 min; a similar evolution was detected in case of addition of PEDOT/PSS, but more pronounced; in the oven at 60 °C, lower particle flattening was observed.

Infrared radiation-assisted sintering was also investigated for three methyl methacrylate/butyl acrylate (MMA/BA) copolymer latex particles (diameter 150 nm) with glass transition temperatures ranging from 45 to 64 °C: adjusting the IR power density enables accurate control over film temperature, polymer viscosity and evaporation rate during latex film formation; when the temperature is too high, a skin layer develops; in order to avoid skin formation, the film temperature, and, hence, the IR emitter power density, must not be too high; when the temperature is too low, the process requires extended time periods [132].

Selective laser sintering of polymer particles has also been performed and, by in situ visualization of the sintering dynamics, necking of PS particles has been investigated over time (Fig. 7(d)) and the effect of different parameters such as heating chamber temperature, laser pulse energy and duration, laser spot size and particle size on the dimensionless final neck radius (i.e. the ratio between the neck radius and the particle radius) has been assessed [128]. When increasing the particle radius from 30 to 105 μm, the ratio of the laser spot size to particle size decreased from 0.66 to 0.19; since for large particles a larger part of the heat energy flows to the non-illuminated regions, the temperature increase in the neck region will be less, resulting in a higher viscosity and thus a slower sintering kinetics [128]. For the cases resulting in incomplete sintering, it can also be seen that the sintering kinetics slows down at the later sintering stages, thereby no longer allowing a description of the kinetics using a modified Frenkel model [128]. Once incomplete sintering is obtained, the final dimensionless neck radius decreases approximately linearly with the overall particle radius [128]. The sensitivity to the heating chamber temperature was shown to be rather limited within a relatively wide range of heating chamber temperatures [128]. The sintering kinetics was demonstrated to be relatively insensitive to the applied laser pulse duration (or correspondingly the laser power) [128]. A linear relation between the laser energy and the dimensionless final neck radius was obtained for the whole range of relevant laser energies, ranging from those resulting in nearly no sintering to those leading to complete sintering [128]. A non-isothermal viscous sintering model has been developed to predict the observed effects of the various parameters: while the initial sintering kinetics as a function of time can be described with a modified Frenkel model for isothermal sintering of viscous liquids (whereby the characteristic viscosity depends on the applied process conditions), the overall sintering kinetics is determined by a complex interplay between the temperature and time effects on the viscosity [128]. Contrary to thermal sintering in a homogeneously heated chamber, laser-induced particle sintering can

slow down and even completely halt at later stages, as a result of the viscosity build-up as a function of time due to the finite relaxation time of the material [128]. Other polymer particles have been investigated, for example polyamide 12 (PA12) particles, using also in situ synchrotron wide angle X-ray diffraction (WAXD) characterization [129,130,137] (Fig. 7(e)). Different models have been developed to describe the sintering process [96,97,112,137].

In addition to the heating system, also the particle characteristics (such as functionalization or size) affect the results of thermal treatments. It is known that such aspects influence self-assembly of particles in terms of order and area coverage [1,5,6,9–11,14,138].

For instance, the influence of particle functionalization has been investigated [123]. This has been done by comparing bare PS and carboxylated PS particles (diameter 96 nm) deposited by spin coating on silicon, annealed with a hot plate at different temperatures (90 °C, 100 °C, 110 °C, 120 °C) and cooled to RT [123]. Non-annealed samples consisting of bare PS particles at RT showed the coexistence of domains of hexagonally ordered particles and of less ordered and uncovered areas, due to non-optimized spin coating conditions [123]. In fact, self-assembly techniques such as spin coating are more sensitive to experimental conditions and more prone to defects in terms of area coverage and order, unless a careful calibration of process parameters is carried out [1,138]. The non-annealed carboxylated PS particles appeared less ordered compared with the bare PS particles, even if with a higher and more uniform average surface coverage [123]. After annealing, particle coalescence occurred for bare PS particles, making individual particles hardly distinguishable, whereas for carboxylated PS particles, individual particles were still visible even if partially merged with neighbours [123]. By studying the global characteristics of the particle film by ellipsometry, it was found that, for thermal treatments around T_g, both the thickness and the refractive index of the polymer film change for both bare and carboxylated PS particles; the variation is strong for bare PS particles already at 110 °C (while, at this temperature, only minor changes are observed for carboxylated PS particles) and for carboxylated PS particles at 120 °C [123] (Fig. 8(a)). The reason for the variation in optical properties has been explained because [123]:

- before annealing, the samples are covered with spherical nanoparticles and voids in between them filled with air; because of the voids, the effective index of refraction of the layer is lower than that of bulk PS;
- after annealing above T_g, particles deform in a way leading to partial merging and coalescence and reduction of the overall film thickness (Fig. 3(b)) leading to fewer voids.

In brief, bare PS particles showed a rapid loss of ordering already at 110 °C, while carboxylated PS particles were more stable until 120 °C [123]. This result was confirmed by in situ GISAXS measurements on samples annealed for one hour [123]. Thus, the stability limit can be shifted towards higher temperatures by a proper surface functionalization, a finding that is useful for applications of PS nanoparticle films at higher temperatures, e.g. when particles are used as a mask for material nanostructuring steps carried out at higher temperatures [123].

Besides 2D particle assemblies, also 3D assemblies of polymer particles have been investigated upon annealing. For instance, such studies have been performed by using in situ X-ray diffraction studies [134–136]. In particular, PS particles were assembled by vertical deposition on glass substrates; the annealing experiments were performed inside the X-ray diffraction chamber [134–136]. More specifically, the glass substrates were mechanically attached to a copper holder plate fixed to a copper block designed as an insert flange in the vacuum sample chamber; the heating of the copper block was supplied by two parallel connected heating elements built into the copper block body [134–136]. For the purpose of sufficient heat exchange, the inner copper block with heating elements was separated by a Peltier element from the outer copper part connected to a water cooling cycle; temperature sensors and controllers completed temperature and heating power control [134–136]. A sketch of the set-up for in situ SAXS and GISAXS is shown in Fig. 8(b). During the measurements, the temperature of the sample was raised incrementally starting from RT; after each temperature increment, a waiting time of 5 min was applied before collecting the data to reach thermal equilibrium within the sample [134–136]. Colloidal crystal films consisted of few tens of monolayers of PS spherical particles, depending on the position on a film along the growth direction, with a cracked texture composed of domains with an average size of several tens of micrometers [134–136] (see the inset of Fig. 8(b)). Fig. 8(c) reports the X-ray diffraction patterns measured in situ during incremental heating of the PS colloidal crystals in experiments for particles of two different sizes. The inspection reveals the following behaviour [134]:

- at temperatures below glass transition temperature T_g, no strong changes are observed in the structure of diffraction peaks, with only a slight decrease in the intensity of higher order Bragg peaks at elevated temperatures;
- at $T > T_g$, a rapid evolution of the diffraction patterns with temperature is observed, namely with a gradual decrease in the intensity of higher order diffraction peaks, which indicates the decay of long-range order in the colloidal crystal upon heating; moreover, a 6-fold modulation of both the intensity of Bragg peaks and the diffuse scattering background in diffraction patterns suggests a transformation of spherical particles in a colloidal crystal into a faceted shape upon dry sintering.

The form factor profiles $I(q)$ (obtained by azimuthal averaging of 2D diffraction patterns over the 2π angular range) confirmed these observations [134] (Fig. 8(d)):

- a high number of intensity oscillations in these curves is found at room temperature, due to the fact that the investigated colloidal particles can be described as hard spheres with narrow size distribution;
- the contrast of intensity oscillations of the form factor curves at high q-values decreases with temperature, as a result of particle deformation towards non-spherical shape and to broadening of the size distribution of particles.

A detailed quantitative characterization of the Bragg peaks as a function of temperature for the measured diffraction patterns via the computation of the Bragg peak position q_B, integrated intensity and full widths at half maximum (FWHM) in radial (w_q) and azimuthal (w_ϕ) directions in reciprocal space allowed the identification of four different stages in the structural evolution of particles upon heating [134]:

- stage I: it corresponds to heating from room temperature to pre-annealing temperature $T_{PA} = 323$ K; no significant variation occurs in the peak parameters, except for a slight decrease in the peak positions q_B due to thermal expansion of the crystal lattice, an increase in w_q and a decrease in w_ϕ for increasing temperature due to a slight increase of the lattice positional disorder along with an annealing effect when crystalline domains become more angularly ordered in the plane of a film;
- stage II: it corresponds to a temperature between T_{PA} and the annealing temperature $T_A = 355$ K; q_B continues to decrease, while both w_q and w_ϕ increase until reaching a maximum at T_A; these results suggest strong enhancement of the lattice disorder and mosaic spread in the colloidal crystal film;
- stage III: it corresponds to a temperature between T_A and $T_g = 373$ K; both w_q and w_ϕ drop to a local minimum, due to the relaxation of the PS crystal film and the reduction of the structural disorder due to annealing;

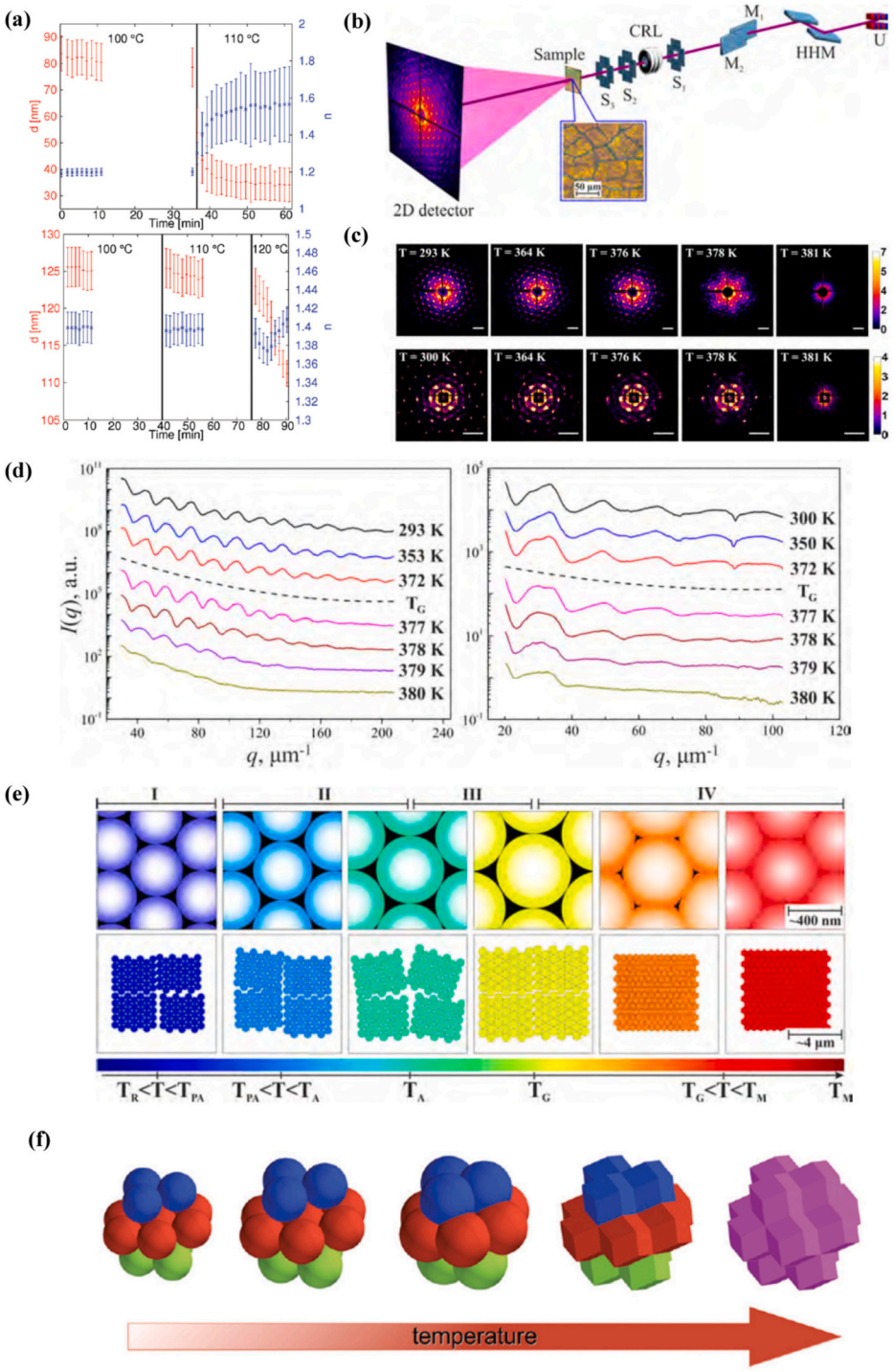

Fig. 8. - Polymer particle annealing: (a) effect of functionalization on PS particle annealing, in particular simulated refractive index *n* and polymer layer thickness *d* of spin-coated PS particles (upper part) and spin-coated carboxylated PS (lower part) during annealing treatment (reprinted with permission from [123]. Copyright 2012 American Chemical Society); (b) sketch of the set-up for in situ SAXS and GISAXS comprising an undulator source (U), a high heat load monochromator (HHM), a pair of flat X-ray mirrors (M_1 and M_2), slit systems (S_1, S_2, S_3), compound refractive lenses (CRL); the inset shows an optical micrograph of the colloidal crystal (reprinted with permission from [134]. Copyright 2015 American Chemical Society); (c) X-ray diffraction patterns measured in situ during incremental heating of the PS colloidal crystals in experiments for particles of two different sizes (upper row 415 ± 8 nm and lower row 386 ± 8 nm) (reprinted with permission from [134]. Copyright 2015 American Chemical Society); (d) form factor curves of PS spherical particles measured from colloidal crystal samples of 415 (left) and 386 nm (right); the glass transition temperature of PS 373 K is indicated by the dashed curve (reprinted with permission from [134]. Copyright 2015 American Chemical Society); (e) schematic diagram of the structural evolution in a colloidal crystal film under incremental heating at nanoscopic (top row) and mesoscopic (bottom row) length scales (reprinted with permission from [134]. Copyright 2015 American Chemical Society); (f) schematic 3D model illustrating the structural rearrangement of face-centered cubic (fcc) closed-packed colloidal spheres in the process of dry sintering (reproduced from Ref. [136] with permission from the Royal Society of Chemistry; https://pubs.rsc.org/en/content/articlelanding/2018/sm/c8sm01412d).

- stage IV: it corresponds to a temperature between T_g and T_m = 381 K; the PS colloidal film undergoes a fast melting process, occurring in a narrow temperature range and ending when the Bragg peaks completely disappear at T_m due to the coalescence of PS particles.

Nanoscopic and mesoscopic changes occur upon incremental heating during these four different stages as sketched in Fig. 8(e) [134]. The nanoscopic length scale is about the size of a colloidal particle that is in the range of few hundred nanometers in this case (Fig. 8(e), top row) [134]. The mesoscopic length scale is related to the size of a coherently scattering domain that is about a few micrometers for the colloidal crystals under study (Fig. 8(e), bottom row) [134]. The following changes have been found [134]:

- on the nanoscopic length scale, a linear growth in the average lattice parameter has been found up to T_g due to thermal expansion; above T_g, PS particles soften and change their shape by flattening in the directions where they are in contact, leading to the observation of the 6-fold diffraction pattern; a decrease in the long range order in the crystalline film occurs with a consequent decrease in the intensity of higher order peaks for increasing temperatures; for temperatures above T_g, the lattice parameter rapidly decreases until complete disappearance of the crystalline structure at T_m;
- on the mesoscopic length scale, no particular change was observed up to T_{PA}, while for temperatures between T_{PA} and T_g, more significant changes occur, namely a relaxation of the crystal lattice due to a partial annealing process above T_A and the coalescence of particles and increase in the inter-atomic distances above T_g due to softening and inter-diffusion of polymer chains.

In a 3D view, particle shape transformation from a sphere to a rhombic dodecahedron occurs upon increasing temperature; the shape transformation is followed by the particle fusion stage, where the boundaries between particles merge together due to the inter-diffusion of polymer chains (Fig. 8(f)) [135,136]. Size-dependent effects have also been found: for example, the melting transition of the colloidal crystal consisting of larger particles of 430 nm size took place at a temperature higher than the transition temperature of the crystal made of smaller particles of 163 nm size [135].

Restructuring of polymer particle films upon thermal annealing has been observed also for other material systems, e.g. 3D assemblies of 160 nm diameter styrene/butyl acrylate copolymer particles (T_g = 64 °C) [59]. The films, formed by evaporation, were annealed by placing them directly on a glass cover slip in a preheated vacuum oven; the annealed samples were quenched to room temperature immediately after thermal treatments and were studied by SAXS [59]. By studying films annealed at different temperatures (between 50 and 170 °C) and for variable annealing time, the role of non-polymeric materials (such as emulsifiers, surfactants and salts) present in the aqueous dispersions and located in the interstices between particles before annealing was also emphasised: as a consequence of this inter-diffusion of polymeric chains, non-polymeric materials tend to aggregate into domains, whose size and polydispersity increase with increasing annealing temperature and time, as sketched in Fig. 9(a) [59].

The mechanisms of closure of voids between nanosized PS particles (between 30 and 93 nm) deposited on silicon substrates in a closely-packed morphology have been investigated by SANS to monitor the size of the voids and their evolution during annealing [60]. Two different patterns of void closure were individuated depending on particle size [60] (Fig. 9(b)):

- larger particles close simultaneously and uniformly throughout the annealing process;
- for particles smaller than 60 nm the interstices close heterogeneously at the nanoscopic level: at the beginning of annealing, some interstices around the nanoparticles close while the others grow, and eventually they all vanish.

The different behaviour has been ascribed to the larger polydispersity of small particles compared to the larger ones, that leads to a more amorphous random closely-packed structure for polydispersed small particles and a more crystalline close-packed morphology for the monodispersed large particles [60]. The random closely-packed structure in small particles yields interstices with a polydispersed size, contrary to the perfect closely-packed structure which gives interstices with a monodispersed size [60]. Interstices with different sizes in the case of small particles originate different curvatures of the polymer/air interface, resulting in different Laplace pressures, with consequent closure of some interstices around the particles and enlarging of the remaining interstices [60]. The uniformity/heterogeneity of void closure was shown not to be affected by the temperature and by the rheological properties of the polymer, but rather by the morphology of the interstices and particularly by their size distribution [60].

As we have seen from the cases previously discussed, particle material plays a key role as it affects T_g. Careful adjustment of T_g can be achieved in copolymer particles. As discussed in Appendix B, copolymer particle composition can be properly adjusted to tune T_g of particle material, thereby tailoring the morphological changes occurring upon thermal treatment. This has been demonstrated in nBA-co-MMA colloidal crystals (monodisperse nanoparticles comprising a random copolymer of methyl methacrylate-MMA and n-butyl acrylate-nBA), possessing different polymer compositions [56]. By varying the nBA content between 10 and 30 vol% the glass transition can be shifted to lower temperatures, in particular 103 °C, 74 °C and 54 °C for 10, 20 and 30 vol% nBA, respectively, with a consequent variation of the viscosity of the polymer at a given temperature [56].

So far, we have discussed thermal treatment of dense 2D and 3D assemblies of colloidal particles. Isolated and small assemblies (clusters like lines or islands) of PS articles (about 100 nm) arranged on silicon substrates by AFM manipulation have been investigated upon sintering above the glass transition temperature T_g of PS: the particles exhibited a significant (approximately 50%) reduction in height and became strongly attached to the substrate; compact structures in form of lines and islands could be obtained after sintering [51].

4.2. Thermal treatment of silica particles

Thermal treatment of silica and mesoporous silica particles is chiefly governed by dehydration and dehydroxilation processes. At specific temperatures, transitions in physicochemical properties of the particles occur, especially in terms of surface functional groups, eventually leading to contraction, necking and coalescence between neighbouring particles.

Morphological variations in particles can be tracked by studying the transmission spectra at normal incidence (Fig. 10(a-b)), complemented by thermogravimetric measurements and SEM characterization. The samples, consisting of 3D assemblies of silica particles, were baked at different temperatures up to 1100 °C, with a heating ramp of 1 °C/min and a holding time of 3 h at the selected sintering temperature [133]. An initial decay in the wavelength corresponding to the minimum in the transmission spectra λ_c was observed between 100 °C and 200 °C [133]. This behaviour was ascribed to sample contraction revealed by thermogravimetric measurements: non-annealed samples contain 9% wt interstitial water, partially hydrogen-bonded to the silanol groups present on the particle surface; thermal annealing above 100 °C results in water removal, with a consequent first contraction of the structure [133]. In addition, water contributes to an increase in the average dielectric constant; hence, loss of water originates a blue-shift of the Bragg reflection wavelength [133]. Above 200 °C, dehydroxylation

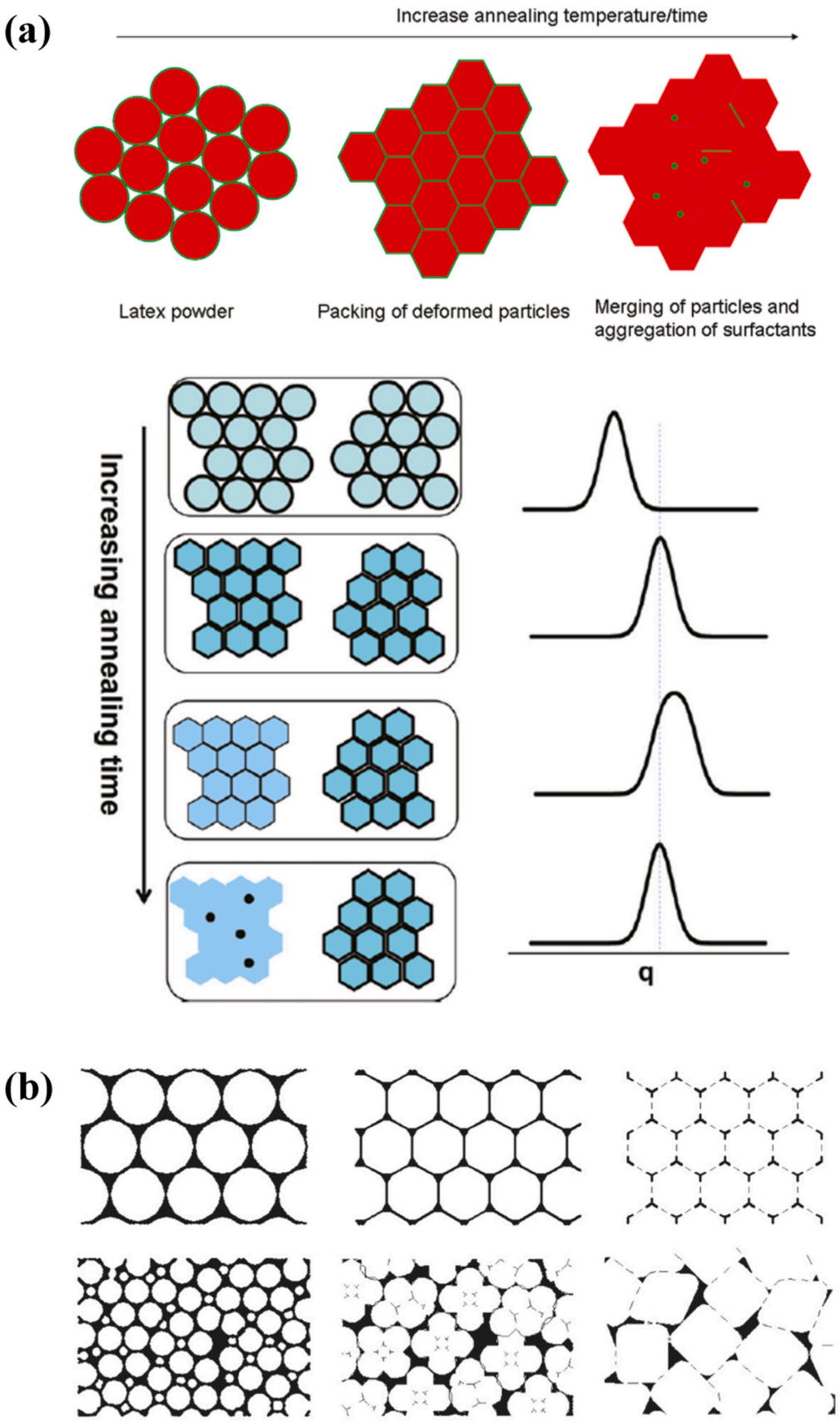

Fig. 9. - Polymer particle annealing: (a) sketch of the aggregation of non-polymeric materials into domains, whose size and polydispersity increase with increasing annealing temperature and time and schematic of the structural evolution of crystallites during annealing at 110 °C and corresponding schematic X-ray diffraction curves (reprinted with permission from [59]. Copyright 2011 American Chemical Society); (b) schematics of different patterns of void closure during particle deformation depending on particle size (reprinted with permission from [60]. Copyright 2009 American Chemical Society).

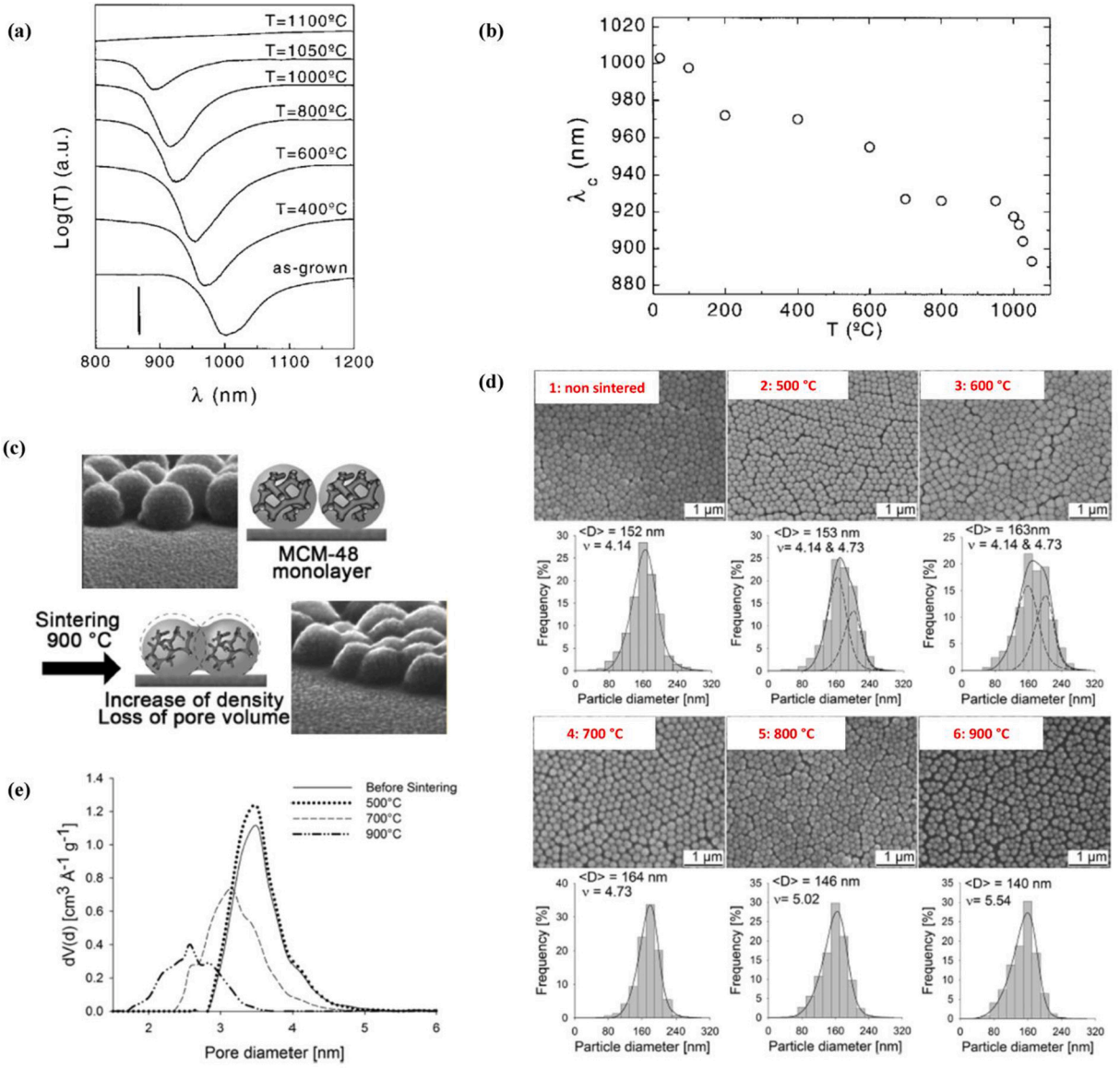

Fig. 10. Silica particle annealing: (a) transmission spectra performed at normal incidence for a photonic crystal made up of silica spherical particles of diameter 415 nm annealed at different temperatures (the vertical bar indicates one decade of attenuation) (reproduced from [133], with permission, copyright 1998, John Wiley & Sons); (b) the (111) Bragg reflection maximum wavelength λ_c plotted against the annealing temperature T (reproduced from [133], with permission, copyright 1998, John Wiley & Sons); (c) SEM images and sketch of mesoporous silica particles upon sintering (reprinted with permission from [119]. Copyright 2015 American Chemical Society); (d) SEM images of mesoporous silica particle layers before sintering and after sintering at different temperatures (reprinted with permission from [119]. Copyright 2015 American Chemical Society); (e) evolution of pore size for mesoporous silica particles sintered at different temperatures (reprinted with permission from [119]. Copyright 2015 American Chemical Society).

processes (implying condensation of the surface silanol groups) occur [47,133]. This results in a surface with new physicochemical characteristics, which, as a consequence, could modify the interparticle interactions, leading to the observed shrinkage of the structure, which could be responsible for the gradual decrease in λ_c between 200 °C and 700 °C [133]. Between 700 °C and 950 °C, neck formation occurs, without contraction, resulting in no variation in λ_c [133]. The sharp variation in λ_c above 950 °C is due to the strong contraction of the structure due to particle interpenetration via viscous flow [133]. This phenomenon causes a reduction of the interstice size (thereby increasing the filling factor of the structure) and is responsible for the observed reduced intensity of the optical attenuation bands [133]. SEM characterization revealed a shrinkage of 7% for the structure treated at 700 °C with respect to the non-annealed sample, but no further contraction until 950 °C, with minor morphological changes up to 950 °C [133]. Hence, the whole structural and optical changes are due to the combination of different phenomena (such as water desorption, surface chemistry and shrinkage) induced by thermal treatment, which causes an increase in the filling factor from 0.74 (non-annealed sample) to 1 (system without interstices and, consequently, devoid of diffraction for annealing at 1100 °C) [133]. These phenomena can be exploited for optical applications, as we will discuss in section 7.2.1.

In [139], sintering of non-porous silica nanoparticles spin-coated to form a monolayer has been investigated: sintering was accomplished by increasing the temperature from 800 °C up to 1200 °C at a rate of 1 °C/min in presence of air, then maintaining constant step temperature for 3 h. A distinct neck-formation was observed, starting at 800 °C and becoming more evident at 950 °C; above 1100 °C, coalescence of particles was observed until the formation of a continuous layer of coalesced silica particles [139]. Particle size distribution and surface packing density were investigated, revealing shrinkage of individual particles and compaction with a change in area coverage [139]. A

geometrical model was developed to quantitatively estimate the evolution of the neck and shrinkage of the silica particles as well as their curvature radius and interpenetration depth [139].

In [119], heating of mesoporous silica particles has been investigated. Thermal treatment of mesoporous silica particles induces densification and loss of pore volume as sketched in Fig. 10(c) [119]. Monolayers of mesoporous silica particles (diameter 154 nm) assembled on silicon substrates by dip coating have been subjected to thermal treatment in an oven and heated under air flow with a ramp of 1 °C/min (sintering at 500, 600, 700, 800, 900 °C for one hour followed by quick cooling to 80 °C) [119]. Particle diameter and pore size were estimated for the different temperatures [119]. Fig. 10(d) shows the corresponding SEM images and particle size distribution. For increasing temperature, the particle distribution widens and tends to higher mean diameter values, then narrows again at 700 °C; at higher temperatures, the distribution widens again but with lower average diameter [119]. Low angle X-ray diffraction (XRD) was used to investigate pore evolution with temperature, which confirmed a densification of the particles, with the decrease in pore volume from 500 °C and of pore diameter from 700 °C [119]. The pore size was not influenced by sintering at 500 °C (about 3.5 nm), but decreased at higher temperature (3.2 nm at 700 °C and 2.6 nm at 900 °C); the pore volume decreased by a factor 2 for sintering at 900 °C [119]. Fig. 10(e) shows the evolution of pore size upon thermal treatment [119]. Above a certain temperature, the diffusion of atoms along the surfaces of mesoporous silica particles is promoted, thereby leading to the formation of necks binding adjacent particles together or increasing binding of particles to the substrate [119]. At higher temperatures and upon densification of silica, volume diffusion becomes the predominant mechanism; the presence of necks is one of the key indications confirming the occurrence of surface diffusion [119]. In particular, it was found that neck formation is clearly observable at 900 °C, but such a high sintering temperature implies also shrinkage of mesoporous silica particles and the occurrence of crevices between clusters of particles, while, at 700 °C, a moderate inflection in pore volume in comparison with treatment at 600 °C was observed [119]. The morphological changes observed in mesoporous silica particles were explained in terms of the behaviour of the silanol groups present on both the surface and inside the particle [119]. As described in section 2.2, upon thermal treatment at increasing temperatures (400–700 °C), the number of −OH groups plunges. Such a decrease in hydroxyl groups was confirmed by comparing NMR measurements on mesoporous silica particles treated at 600 °C and untreated particles as well as by TGA-DSC [119]. At 500 °C, a slight increase in particle diameter was noticed, ascribable to the initiation of Si and O rearrangement due to −OH condensation into $Si-O-Si$ [119]. Between 500 and 600 °C, strong particle swelling occured (>10% of the initial diameter) as well as the presence of a slight heterogeneity in particle morphology [119]. This increase in particle size may be attributed to a rearrangement of the SiO_2 framework, possibly in the presence of H_2O from further $Si-OH$ condensation reactions [119]. Between 700 and 800 °C, pore volume and radius decrease significantly as a result of an intra-particle diffusion/densification process as well as by hydroxyl condensation [119]. Thermal treatment of mesoporous silica particles below 700 °C was suggested as a route to ensure anchoring of mesoporous silica particles to silicon substrates and between them, while preserving optimal mesopore volume and structure [119].

The role of hydroxyl groups in promoting the formation of necks between mesoporous silica particles as well as in affecting the refractive index has been investigated also in [120] by combining TGA, FTIR, SEM, ellipsometry and ellipsometric porosimetry. In particular, a reduction in the refractive index of mesoporous silica films was observed due to the decrease of −OH groups (because the presence of −OH groups increases the dielectric constant of mesoporous silica films).

4.3. Thermal treatment of composite particles

Thermal treatment of PS core/silica shell particles can be exploited to get spherical hollow silica particles [140]. Calcination of the core/shell structure was performed by heating core/shell particles in a furnace at 500 °C, 650 °C, 800 °C or 950 °C in air for 12 h [140]. Decomposition of the PS core sets in at about 300 °C [140]. Thermal elemental analysis of N, C and O confirmed the complete combustion process by a lack of carbon in the 500 °C calcined particles, demonstrated also via TGA where a loss of ~2% was observed due to the removal of intercalated water [140]. The weight loss step (~ 2%) at temperature up to 100 °C relates to the loss of adsorbed water [140]. Another 1% of mass is lost up to 950 °C, which can be attributed to the removal of trace amounts of silica condensation products such as water [140]. During this core-removal calcination step the outer diameter of the core/shell sphere shrinks by about 2% when transitioning into hollow spheres [140]. Uniformity and monodispersity of the obtained hollow spheres was confirmed by transmission electron microscopy (TEM) measurements, which showed that the spheres remain fully intact during the calcination cycle and that they do not feature any cracks or dents; they exhibit a smooth surface, do not form aggregates or clusters or sinter necks between particles, so that they can be individually redispersed in ethanol (Fig. 11(a-d)) [140]. Furthermore, only a minor shrinkage of their diameter and shell thickness was observed even after higher calcination temperatures up to 950 °C: the diameter slightly shrank from 316 nm to 310 nm, whereas the shell thickness remained almost constant at 44 nm [140]. The density of the silica shell measured via He pycnometry was shown to be 2.27 g cm^{-3} [140]. The internal structure of the silica shells changes quite considerably with the calcination temperature [140]. Using N_2 sorption measurements, NMR and non-local density functional theory (NLDFT) analysis, a drop in the micropore volume was detected for increasing calcination temperature [140]. Fig. 11(e) reports the pore size distribution for variable calcination temperature, revealing the closure of micropores of about 5–8 Å in radius for increasing temperature [140]. Despite the rearrangement, which happens during the high temperature calcination, the SiO_2 network remains in its fully amorphous state and exhibits no onset of crystallization, as suggested by XRD characterization [140]. Silica networks obtained by the Stöber method predominantly consist of Si atoms, which are connected to three (Q^3) or four (Q^4) neighbouring $-O-Si-$ units [140]. The ratio between Q^3 and Q^4 changes with increasing calcination temperature and ultimately leads to a fully condensed SiO_2 network: the ratio $Q^4/(Q^3+Q^4)$ increases from 0.88 to 0.94 for temperatures varying between 500 and 950 °C [140]. In addition, also the rigidity of the still amorphous silica network increases for increasing temperature [140]. All these changes to the internal structure (surface area reduction, closure of micropores, increase of Q^4 content and increase of rigidity) happen simultaneously during calcination as sketched in Fig. 11(f) [140]. Colloidal crystals of hollow silica nanoparticles have been proposed as a highly thermally insulating material controllable via the calcination temperature, with a temperature-dependent thermal conductivity increasing for increasing calcination temperature (Fig. 11(g)) [140].

Thermal annealing of core/shell particles composed of polymers with a strong difference in glass transition temperature has been investigated using GIUSAXS and AFM [73]. In particular, particles were made up of a low-T_g (−54 °C) core (*n*-butylacrylate, 30 wt%) and a high-T_g (41 °C) shell (*t*-butylacrylate, 70 wt%) and had an overall diameter of about 500 nm [73]. The particles were self-assembled on silicon substrates by vertical dip coating and annealed at temperatures between 60 and 140 °C by placing them directly on a copper plate in a preheated oven for 2 h; other tests were carried out at 60 °C for annealing time between 5 and 800 min; the annealed samples were quenched to room temperature immediately after thermal treatment [73]. The AFM images showed smoothening of the surface morphology of the latex film during

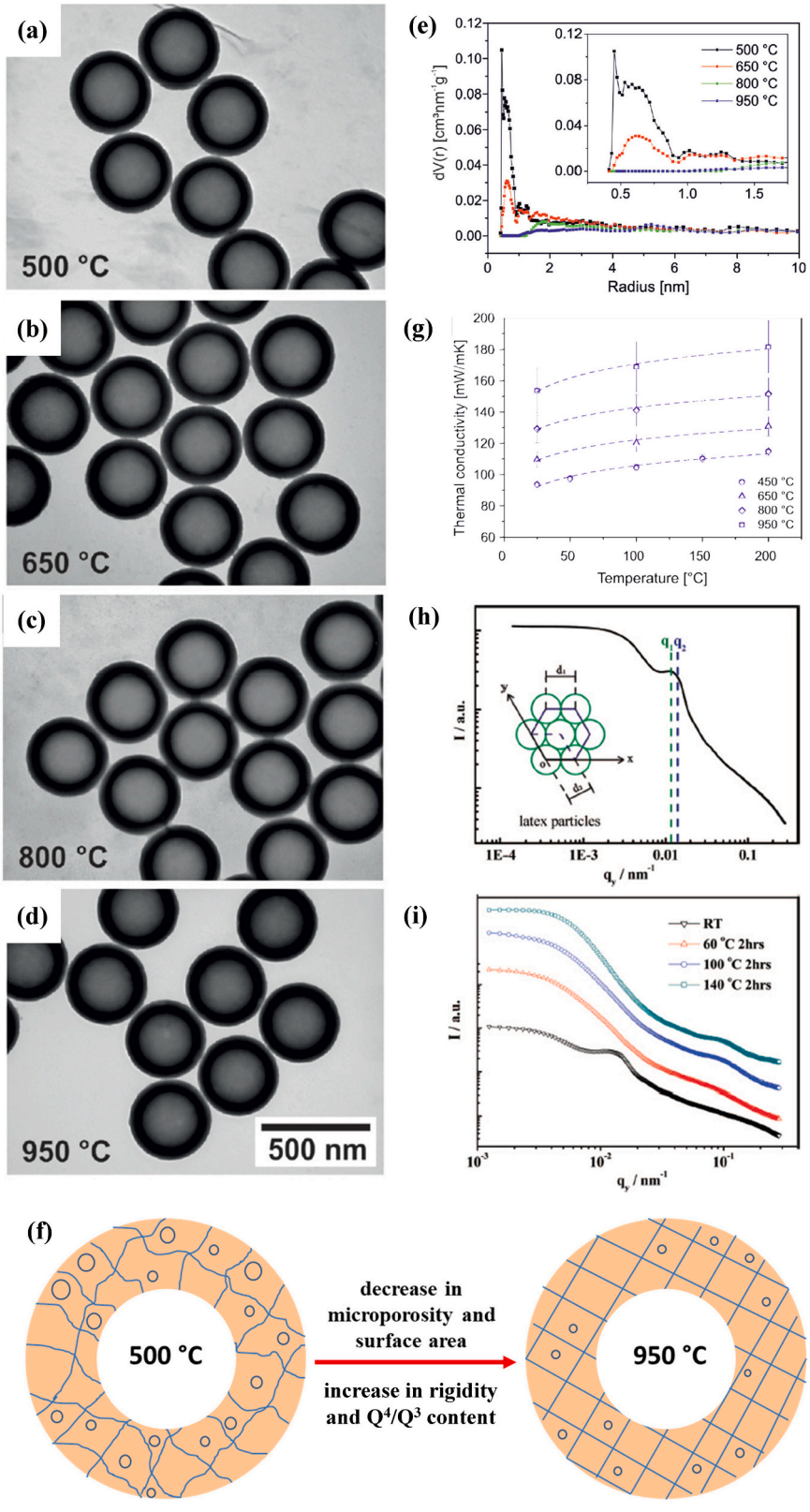

(caption on next page)

Fig. 11. - Silica particle annealing: (a-d) TEM images of hollow silica nanoparticles at different calcination temperatures (500–950 °C); the particle dimensions remain constant for the various calcination temperatures and do not show any clustering (reproduced from Ref. [140] with permission from the Royal Society of Chemistry; https://pubs.rsc.org/en/content/articlelanding/2015/nr/c5nr00435g); (e) computed pore radius distributions suggesting closure of the micropores at higher calcination temperatures (reproduced from Ref. [140] with permission from the Royal Society of Chemistry; https://pubs.rsc.org/en/content/articlelanding/2015/nr/c5nr00435g); (f) schematic representation of the internal structural changes upon high temperature calcination (redrawn and adapted from [140]); (g) thermal conductivity of annealed colloidal crystals (450–950 °C), calcinated at 950 °C prior to the assembly of the monoliths (reproduced from Ref. [140] with permission from the Royal Society of Chemistry; https://pubs.rsc.org/en/content/articlelanding/2015/nr/c5nr00435g); (h) scan of the GIUSAXS pattern of the latex film before annealing along the q_y direction at $q_z = 0.27\ \mathrm{nm}^{-1}$; the inset indicates the structure of the latex film (reprinted with permission from [73]. Copyright 2008 American Chemical Society); (i) GIUSAXS patterns along the q_y direction at $q_z = 0.27\ \mathrm{nm}^{-1}$ for a latex film annealed at different temperatures for 2 h (reprinted with permission from [73]. Copyright 2008 American Chemical Society).

annealing, while GIUSAXS for variable temperature revealed a distinct change in the structure of the thin film, in particular with the disappearance of the Bragg peaks representing large-scale ordering and the appearance of a new Bragg peak representing small scale ordering, which suggest a thermally induced reconstruction of the latex film (Fig. 11(h-i)) [73].

Thermal annealing of colloidal crystal fibers formed by self-assembly of styrene/n-butyl acrylate copolymer particles (118 nm diameter) in a cuboidal Kapton tube with a length of 25 mm, a width of 5 mm and a height of 1.5 mm has been investigated by SAXS for variable temperature, revealing changes of the lattice constant of the colloidal crystallites and the intensity evolution of the scattering from the crystalline and the amorphous phases during heating and annealing; such changes denote characteristic temperatures where the system exhibits pronounced structural changes [72].

Thermal properties of polymer-grafted particle systems have been investigated, for example polystyrene-grafted silica colloids in the dense grafting limit: the glass transition temperature of particle brush materials was shown to depend on the architecture of particle brush systems; generally speaking, the grafting of polymers to the particle surface was found to raise the glass transition temperature of polymers and the relative increase (with respect to the corresponding linear polymer of equal degree of polymerization) was found to increase with decreasing degree of polymerization of surface-grafted chains [141].

5. Thermal annealing of polymer particles on a polymer film

Thermal annealing of polymer particles pre-assembled on a polymer film has been investigated as a tool to get anisotropic particle shapes or structured polymer films [142].

The principle is shown in Fig. 12(a-b). As a model system, PS particles on PMMA-coated glass have been considered. The sequence of the processing steps can be summarized as follows [142]:

- polymer particles are assembled on the polymer film;
- annealing is carried out at a temperature $T > T_g$ of both the particle material and the polymer film (for example at 240 °C higher than T_g of both PS and PMMA which amount approximately to 100 °C for PS and 105 °C for PMMA, respectively) for a certain annealing time;
- polymer particles gradually sink into the polymer film and convert their shape from spherical to hemispherical in case of thick polymer film or in disk-like particles in case of thin polymer films;
- by selective removal of the polymer film (e.g. using acetic acid for the PS/PMMA system), anisotropic polymer particles can be released; by selective removal of particles (e.g. using cyclohexane for the PS/PMMA system), a patterned polymer film can be obtained; if none of them is removed a heterogeneous deformed PS/PMMA polymer surface is obtained.

Morphological evolution of PS particles of 6–10 μm on thin (5 μm) and thick (13 μm) PMMA films has been investigated as a function of time by optical microscopy and SEM (Fig. 12(c)) [142]. The PS particles

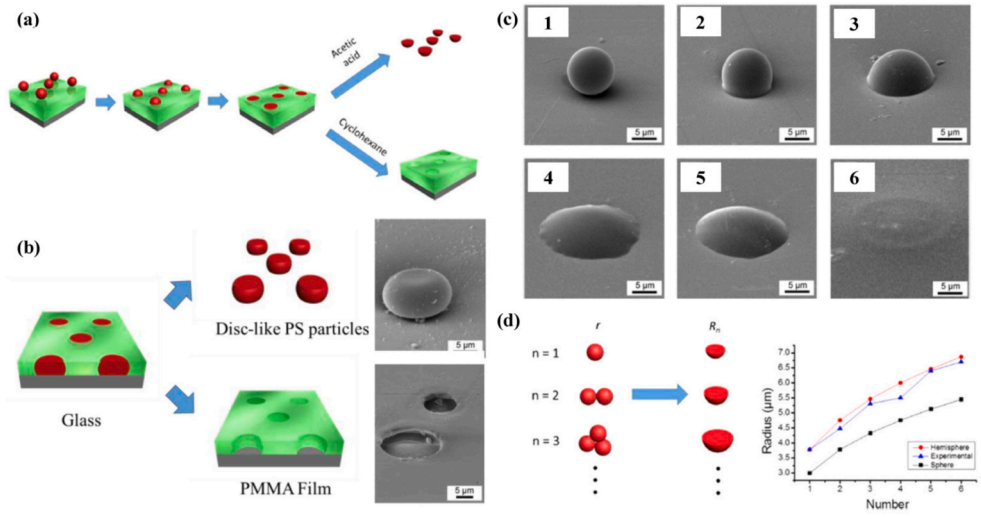

Fig. 12. - Thermal annealing of polymer particles on a polymer film: (a) sketch of the experimental process to prepare PS/PMMA composites by annealing PS microspheres on PMMA films to obtain either PS hemispheres or porous PMMA films by the selective removal technique (reprinted with permission from [142]. Copyright 2015 American Chemical Society); (b) sketch of the experimental process to remove the PMMA film or the PS particles selectively in the case of thinner PMMA films and corresponding SEM images (reprinted with permission from [142]. Copyright 2015 American Chemical Society); (c) SEM images of PS microspheres annealed on PMMA films at 240 °C for (1) 0, (2) 30, (3) 60, (4) 180, (5) 240 and (6) 300 s (reprinted with permission from [142]. Copyright 2015 American Chemical Society); (d) sketch of transformation of single or multiple spheres into hemispheres and plot of the radius of the merged PS particles as a function of the number of microspheres (the original radius of the PS microspheres before annealing is ~3 μm) (reprinted with permission from [142]. Copyright 2015 American Chemical Society).

gradually sink into the PMMA films with the annealing time, until sinking completely after about 300 s; the surfaces of the PS/PMMA composite films become flat [142]. This has been explained in terms of surface tension: the one of PS is lower or very close to that of the PMMA when the samples are annealed at 240 °C [142]. The possible presence of the surfactants, used for PS particle synthesis, might also contribute to the lower surface tension of the PS [142].

The shape evolution has been modelled under the hypothesis that PS particle volume is conserved during the annealing process [142]. In case of transformation into a hemispherical shape for an isolated particle, the

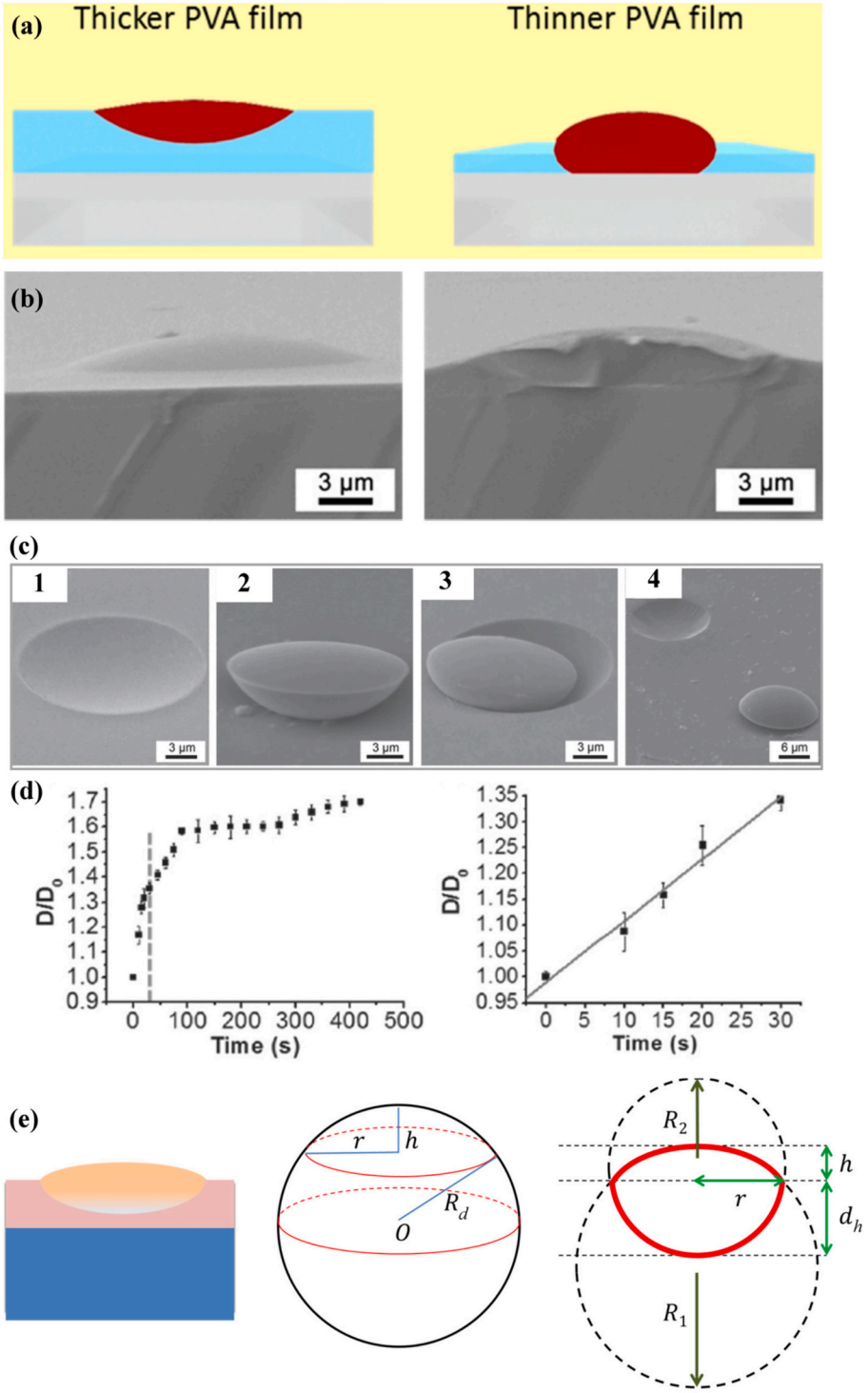

Fig. 13. - Thermal annealing of polymer particles on a polymer film: (a) schematic of the PS/PVA composites for thicker and thinner PVA films (reproduced from [143], with permission, copyright 2016, John Wiley & Sons); (b) SEM images of the cross-sections of PS/PVA composites for thinner PVA films (thickness ~ 1 μm) (reproduced from [143], with permission, copyright 2016, John Wiley & Sons); (c) SEM images of PVA films with cavities and asymmetric PS particles: (1) a PVA film with a cavity, (2) an asymmetric PS particle, (3) an asymmetric PS particle and a cavity and (4) an asymmetric PS particle near a cavity (reproduced from [143], with permission, copyright 2016, John Wiley & Sons); (d) plots of diameter ratio (D/D_0) versus time with different time ranges (reproduced from [143], with permission, copyright 2016, John Wiley & Sons); (e) sketch of the geometrical model of morphological change (redrawn and adapted from [143]).

following equation should hold [142]:

$$\frac{4}{3}\pi r^3 = V_{sphere} = V_{hemisphere} = \frac{1}{2}\frac{4}{3}\pi R_1^3 \tag{10}$$

where V_{sphere} is the volume of the original spherical particle of radius r and $V_{hemisphere}$ is the volume of the deformed hemispherical particle with radius R_1 after annealing. Hence, the final particle radius can be written as [142]:

$$R_1 = \sqrt[3]{2}r \tag{11}$$

In case multiple neighbouring particles are annealed, particles aggregate, merge and transform into larger hemispheres; the previous model can be extended to the case of n particles in the following way [142]:

$$n\frac{4}{3}\pi r^3 = nV_{sphere} = V_{hemisphere(n)} = \frac{1}{2}\frac{4}{3}\pi R_n^3 \tag{12}$$

where $V_{hemisphere(n)}$ is the volume of the hemisphere resulting from merged particles whose radius R_n is [142]:

$$R_n = \sqrt[3]{n}r \tag{13}$$

These relationships were confirmed by measurements on both isolated and multiple neighbouring particles (Fig. 12(d)) [142].

The flexibility of the process has been explored by changing the polymer material combination. While flattened asymmetric polymer particles were obtained in the PS particle/PMMA film system, by replacing PMMA with poly(vinyl alcohol) (PVA, $T_g = 85^{\circ}C$) films, asymmetric PS particles composed of two hemispheres with different curvatures can be obtained after annealing at 240 °C and selective removal of PVA film in acetic acid or PVA films with cavities can be generated after selective removal of PS particles in cyclohexane as inferred from studies of 10 μm PS particles on thin (1 μm) and thick (7 μm) PVA films [143]. The morphologies obtained for thin and thick PVA films are shown in Fig. 13(a-c). For longer annealing times, PS particles sink more deeply into the PVA film for both isolated and multiple neighbouring particles; for example, two particles can form peanut-like and rod-like structures [143]. The morphological transformation has been explained as the combination of two processes [143]:

- the deformation process: the shape of the PS particles converts from spherical to asymmetric; this process dominates at the initial stage of annealing;
- the sinking process: the PS particles are immersed into the PVA films and their shape is preserved; this process dominates at a later stage of annealing.

By studying the variation of particle diameter over time (in particular its increase with respect to the initial particle diameter), two different regimes have been distinguished (Fig. 13(d)) [143]:

- an initial period of linear growth;
- a second period of non-linear slower growth.

A geometrical model of shape change has been developed as illustrated in Fig. 13(e) in case of thick PVA film. The final shape is the intersection of two spheres with different radii, where R_b is the radius of the bottom sphere, R_t is the radius of the top sphere, R_d is the radius of the deformed particle, h is the upper height of the particle and d is the lower height of the particle [143]. The upper height h can be estimated by SEM images even without removal of PVA and the lower height d_h can be estimated by volume conservation as [143]:

$$\frac{4}{3}\pi r^3 = V_{sphere} = V_{deformed} = V_b + V_t = \pi h^2\left(R_b - \frac{1}{3}h\right) + \pi d^2\left(R_t - \frac{1}{3}d_h\right)$$
$$= \pi h^2\left(\frac{R_d^2 + h^2}{2h} - \frac{1}{3}h\right) + \pi d_h^2\left(\frac{R_d^2 + d_h^2}{2d} - \frac{1}{3}d_h\right) \tag{14}$$

Deviations from this geometrical model could occur because of its simplifying assumptions: in particular, perfect volume conservation could not be guaranteed because slight volume contraction could take place during thermal annealing to get a denser packing of polymer chains; in addition, the ideal model of two intersecting spheres could not be completely faithful to reality [143].

Annealing at lower temperatures (e.g. 200 °C) results in a slower annealing process because of the lower mobilities of the polymer chains and higher polymer viscosity at lower temperatures [142,143].

Self-stretching and deformation into ellipsoidal shapes could be obtained by performing annealing on polymer particles assembled on a free-standing polymer film clipped with two binder clips on both sides; after the annealing process, the binder clips were removed from the films and the deformed polymer films with stretched polymer particles were obtained [144]. In particular, the process illustrated in the schematic (Fig. 14(a)) has been applied to the annealing at 240 °C of 10 μm PS particles on 50 μm thick PVA films; morphological changes have been

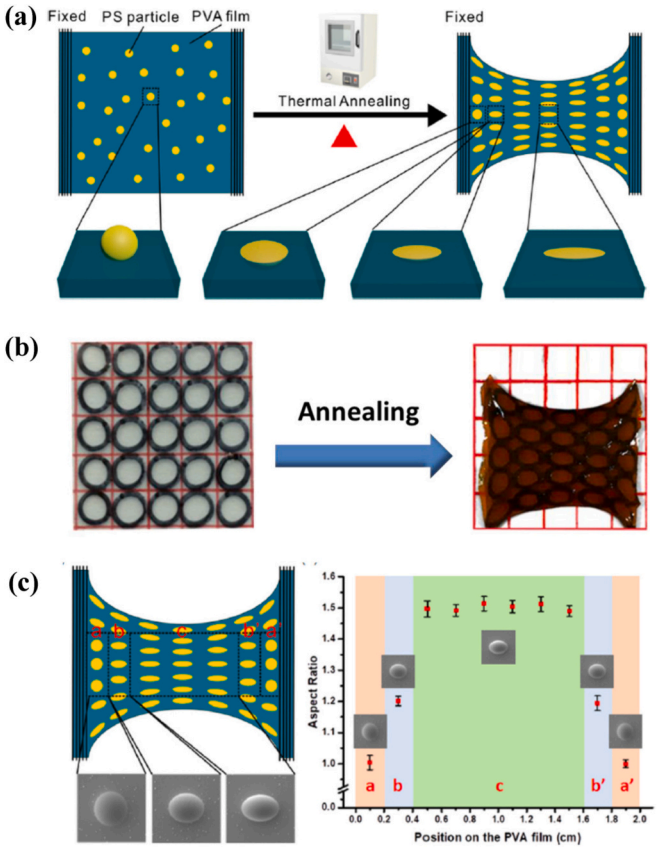

Fig. 14. - Thermal annealing of polymer particles on a free-standing polymer film: (a) sketch of the thermal annealing and self-stretching processes (reprinted with permission from [144]. Copyright 2017 American Chemical Society); (b) photograph of a PS/PVA composite film before and after the annealing and stretching process (size of the original film 2 cm × 2 cm) (reprinted with permission from [144]. Copyright 2017 American Chemical Society); (c) sketch and SEM images of the PS particles collected from different positions on a PVA film (left); aspect ratio of the PS particles as a function of the positions on the PVA films (right) (reprinted with permission from [144]. Copyright 2017 American Chemical Society).

investigated either by selectively removing PVA (by immersion of the PS/PVA composite in 30% isopropanol/water solution at 65 °C) to get anisotropic PS particles or by selectively removing PS (by immersion in toluene) to get PVA films with cavities [144]. Due to annealing far above the glass transition temperature, PVA films and PS particles are softened and become deformable [144]. As the surface tension of PS is much lower than that of PVA, the PS particles sink into the PVA films during the annealing process [144]. Simultaneously, the deformation of the PVA films to stretch the PS microspheres is induced by the high temperature annealing and bound edges [144]. As no external forces are applied to the PVA films during the deformation processes, shaping occurs via self-stretching [144]. Residual water in the PVA films is evaporated because of the high-temperature annealing, resulting in the contraction of the films and the deformation of the PS particles [144].

A crucial element for the process is represented by the binder clips, which confine the rims of the PVA films; they can be exploited to affect the deformation of the PS particles at different locations of the PVA films and get anisotropic PS particles with different shapes on a single PVA film, in particular [144]:

- for PS particles collected close to the binder clips, the samples are less stretched and oblate spheroidal PS particle deformation occurs;
- for PS particles farther from the binder clips, the degree of stretching increases and prolate spheroidal PS particle deformation is observed (aspect ratio expressed as the ratio between major and minor axis equal to 1.2);
- for PS particles near the center of the PVA films, the degree of stretching is the highest and prolate spheroidal particle deformation is found (aspect ratio of 1.5).

Fig. 14(b-c) show the deformation at different locations of the PVA film.

Deformation has been explained in the light of two different models [144]:

- a stretching force model, in which PS particles are stretched along the clip-clip direction; it is due to the contraction of the PVA films near the binder clips, which causes the stretching of the middle PVA films towards the binder clips to release the residual strains;
- a squeezing force model, in which PS particles are squeezed orthogonally to the clip-clip direction; it is caused by the surface tension of PVA and the evaporation of the residual water in the PVA film.

Different particle shaping effects can be obtained by using different binder clip configurations (for example four binder clips instead of two) [144]. Also in this case, polymer particles or polymer cavities of more complex shapes can be obtained by multiple neighbouring particles [144].

Morphological changes can be investigated by optical microscopy, SEM and scanning probe microscopy techniques such as AFM and scanning near field optical microscopy (SNOM) [142–148].

Comparison between polymeric and non-polymeric substrates has been performed. In particular, the influence of both temperature and substrate (polymeric and non-polymeric) has been investigated in thermal annealing of PS particles [149]. More specifically, ordered monolayers of PS spherical particles were prepared on both hydrophilic (glass and mica) and hydrophobic (PS and PMMA) substrates by convective self-assembly [149]. The influence of annealing on order was quantitatively assessed by image processing and analysis at temperatures below and above the glass transition temperature T_g of PS (97 °C) and PMMA (100 °C), with the following conclusions [149]:

- generally speaking, large ordered domains in the monolayers break up into smaller regions separated by cracks, because of the thermal expansion of the polymer and the attractive dispersion force between particles;
- large changes in the monolayer morphology were observed even by annealing to temperatures below the T_g of PS (ramping the temperature from 20 to 90 °C at 1 °C per minute, holding the samples at the elevated temperature for a certain amount of time, then ramping the temperature back down to 20 °C at the same rate); for samples with initially poor order, no change in the monolayer morphology was observed upon annealing; however, for samples with initially higher order, particles would move and a large, apparently well-ordered domain would break up into a collection of smaller domains separated by cracks, similar to the appearance of a dried mud puddle; when the temperature is decreased to room temperature, particles become smaller, but if the surfaces of neighbouring microspheres stick together during the heating cycle, this feature will be preserved as the temperature is decreased, forming small, densely packed regions within the monolayer, thereby broadening the cracks; the substrate affects the rate at which changes in the microsphere monolayer morphology occurred at elevated temperatures; for instance, the evolution was much slower for monolayers on glass than for monolayers on PMMA substrates; in addition, rolling or dragging of the microspheres during the sticking of the particles at high temperature and during their subsequent cooling to room temperature is affected by the substrate;
- in annealing experiments above T_g of PS (the temperature was ramped at 1 °C per minute from 95 to 140 °C and images of the same area of the sample were acquired at 1 min intervals), measurements of the widths of cracks in the monolayers showed differences between substrates: in the initial stages of the experiments, the changes in morphology for microsphere monolayers on the different substrates did not differ significantly, with essentially no change at all until the temperature reached approximately 106 °C, after which the cracks separating densely packed regions began to increase in width, as the microspheres in the densely packed regions started to deform and material began to flow; at later stages, the width of the cracks in monolayers on PS substrates were observed to decrease more quickly than for monolayers on PMMA substrates;
- after very long times at relatively high temperatures, the monolayers on both substrates became essentially smooth films.

6. Thermal annealing at the air/water interface

Thermal annealing of particle monolayers self-assembled at the air/water interface has been proposed as a route to tune the interstice size without major alteration of the initial particle arrangement (i.e. with negligible introduction of extra cracks) [150]. The possibility to carry out thermal treatments at the air/water interface permits to benefit from the high control over order and morphology of colloidal monolayers attainable by this self-assembly technique in comparison to other methods [1,5,6,10,11,14,17]. In addition, simple implementations of air/water interface self-assembly have been worked out, offering accurate control over morphology and area coverage of the final monolayer with a straightforward implementation in both crystalline [5,14] and amorphous patterns [10,11]. The morphology can be subsequently investigated using SEM or scanning probe microscopy techniques [150–154].

Fig. 15(a) shows the schematic of the process for thermal annealing of a colloidal polymer particle monolayer; the process is articulated in the following steps [150]:

- a colloidal monolayer is self-assembled at the air/water interface in a Petri dish;
- after self-assembly, the monolayer is transferred to an intermediate glass substrate;
- the colloidal monolayer is transferred onto the water surface inside a hydrothermal reactor via the intermediate glass substrate;

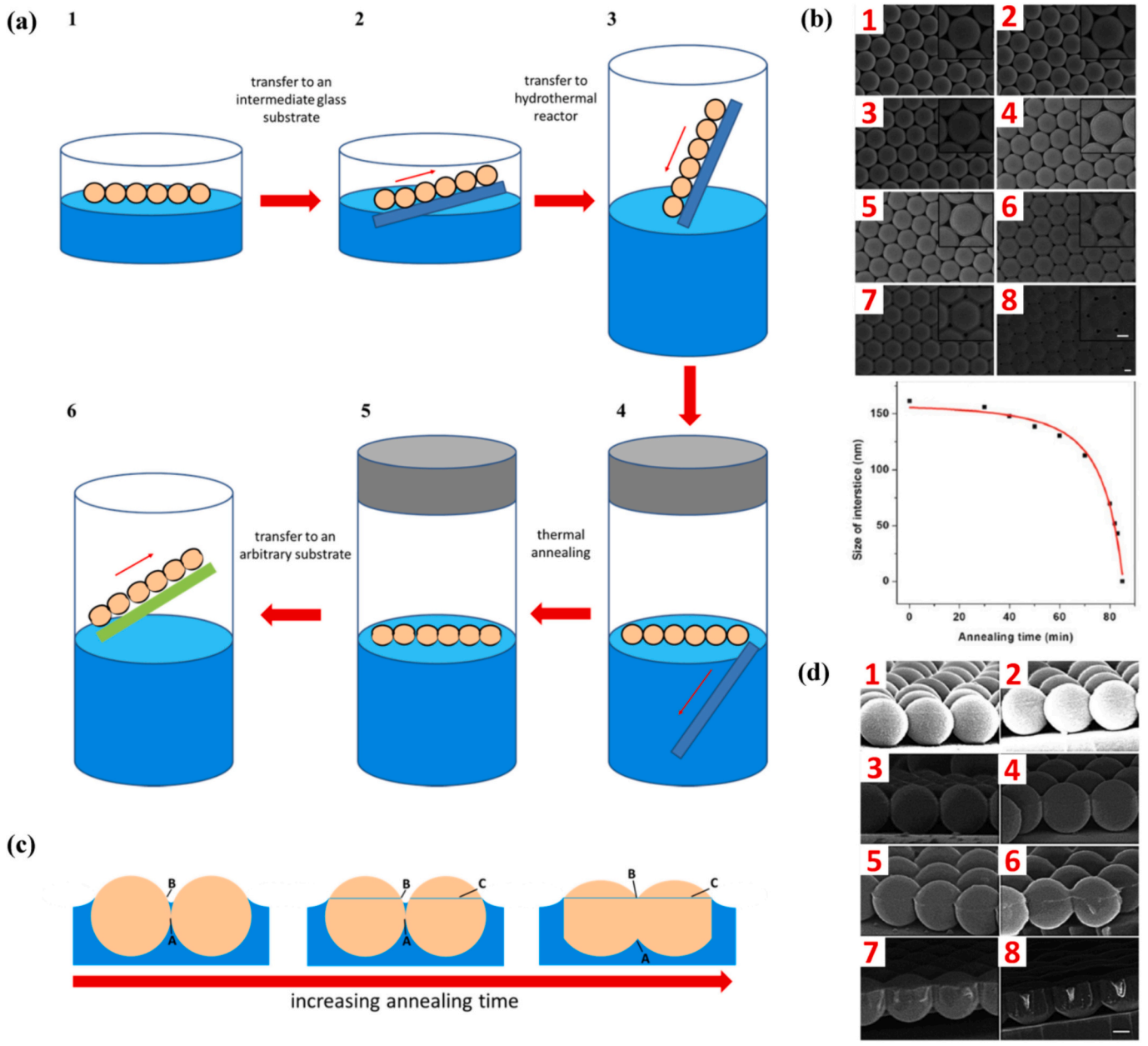

Fig. 15. - Thermal annealing at the air/water interface: (a) schematic of the process for thermal annealing of a colloidal polymer particle monolayer at the air/water interface (redrawn and adapted from Ref. [150]); (b) SEM images of monolayers of 683 nm PS colloidal particles after thermal annealing at 120 °C for (1) 30 min, (2) 40 min, (3) 50 min, (4) 60 min, (5) 70 min, (6) 80 min, (7) 82 min and (8) 83 min, respectively (the insets show high magnification SEM images; the scale bars are 200 nm); the lower plot shows the interstice size as a function of the annealing time at 120 °C (reproduced from Ref. [150] with permission from the Royal Society of Chemistry; https://pubs.rsc.org/en/content/articlelanding/2012/jm/c2jm33660j); (c) sketch of PS particles before thermal annealing (left), after the appearance of the annular region (center), after merging of the two locations (right); A indicates the contact point at the equator, B the three-phase interface, C the annular region (redrawn and adapted from Ref. [150]); (d) tilted cross-sectional views of monolayers of 683 nm PS particles annealed at 120 °C for (1) 40 min, (2) 50 min, (3) 60 min, (4) 70 min, (5) 80 min, (6) 82 min, (7) 85 min and (8) 87 min (scale bar 200 nm) (reproduced from Ref. [150] with permission from the Royal Society of Chemistry; https://pubs.rsc.org/en/content/articlelanding/2012/jm/c2jm33660j).

- thermal annealing is applied to the floating colloidal monolayer sealed in the hydrothermal reactor at a temperature T higher than T_g;
- the annealed monolayer is transferred to the desired solid substrate.

In selecting the temperature T for annealing, one should take into account these two factors [150]:

- the glass transition temperature T_g of the polymer particle material, because T should be higher than T_g;
- the highest temperature for existence of water in the liquid phase in an open system is its boiling point at local atmospheric pressure; above that temperature, transition into the vapour phase will occur rather than increase in temperature as additional thermal energy is provided, limiting highest temperature to 100 °C if the environmental pressure is the standard atmospheric pressure; in case of a closed system (as is the case for a hydrothermal reactor), water vapour due to continuous heating cannot escape from the confined space, entailing an increased inner pressure; hence, the water in a hydrothermal reactor can offer homogeneous conditions for thermal

annealing with a temperature above 100 °C and does not boil as it does in an open system, thereby hampering possible disruption of monolayer arrangement.

Experiments have been carried out on PS particles (diameter 683 nm) at different temperatures (100 °C, 120 °C, 150 °C and 180 °C, with T_g of PS of around 100 °C) with the following conclusions [150]:

- concerning the annealing time (variable up to about 85 min for $T = 120^{\circ}$C), experiments at 120 °C revealed no major change for an annealing time up to 40 min; for longer annealing time, an annular region appears at the edge of each PS particle; the interstice size between three neighbouring particles gradually shrinks, but still retains a concave-line nearly triangular shape; for an annealing time above 80 min, the annular regions of two neighbouring PS particles combine together, leading to a regular triangular interstice between three neighbouring particles; with even longer annealing time, the interstice size rapidly shrinks, while the shape of the interstice turns into a convex-line triangle; by studying the time-dependence of the interstice size, a non-linear behaviour was observed, with the presence of two different stages of shrinkage (a first stage with a lower shrinkage rate with a rate of about 0.7 nm/*min* for an annealing time below 70 min at 120 °C and a second stage with a faster shrinkage rate of about 5.3 nm/*min* for an annealing time above 70 min at 120 °C); at some point, the interstices get completely closed (for about 85 min at 120 °C) (Fig. 15(b));
- concerning the dependence on temperature, by comparing experiments at the same annealing time of 50 min, a higher annealing temperature increases the shrinkage rate, because the mobility of the polymer chains is enhanced due to the increased thermal energy; a non-linear time-dependence similar to the one observed for 120 °C was found at 150 °C, but with complete closure of the interstices already after 60 min;
- as to particle size, experiments performed at 120 °C for another PS particle diameter (898 nm) revealed a similar trend in interstice shrinkage.

By observing temporal evolution of particle shape, it has been observed that morphological changes of PS particles occur at two different locations, as illustrated in Fig. 15(c) [150]:

- at the contact point A between two neighbouring particles;
- at the liquid/gas/solid three-phase contact line (see point B).

When no thermal annealing is applied, two neighbouring particles touch in a point; thermal annealing at $T > T_g$ increases the mobility of the polymer chains, leading to particle merging at the contact point (point A) and reduction of interstice size; at the same time, also the mobility of the top part of PS particles increases, similarly to what occurs in the bottom part immersed in water; at the liquid/gas/solid three-phase contact line (see point B), the surface tension of water tends to pull the softened polymer chains of the top part of PS spheres which protruded out of the water along the three-phase contact line to reduce the contact area between liquid water and its vapour, resulting in the formation of a ridge at the three-phase contact line; as annealing time increases, morphological changes become more dramatic [150]. The morphological evolution was confirmed by cross-sectional views of the annealed particle monolayers at 120 °C for increasing annealing time (Fig. 15(d)) [150]. Three neighbouring particles tend to connect together with the formation of necks at the equatorial region and a ridge (probably corresponding to the annular region in the top view SEM images) at the three-phase contact line for sufficiently long annealing time (40 min); the ridge and particle coalescence due to the formation of necks become more evident for increasing annealing time; the deformation of the equator drags the adjacent ridges that approach each other until coalescence and merging of necks and ridges (>70 min); the deformation at both the equator and the three-phase contact line contribute to interstice shrinkage, until complete closure [150]. Simultaneously, the top part of the PS particles protruding out of the water surface flattens under the combined action of thermal energy and surface tension of water, while the bottom part retains the spherical shape, leading to an asymmetric particle deformation [150]. For increasing annealing temperature, the polymer chains diffuse more and more quickly across sphere boundaries at the equator as well as at the three-phase contact line, with a consequent faster interstice shrinkage [150].

7. Applications

Annealed colloidal monolayers can be indirectly used as a mask in nanosphere lithography or directly employed for their intrinsic physical properties, for example for their inherent optical or thermal properties. In addition, thermal treatments can be exploited to shape particles into specific morphologies.

7.1. Indirect use in colloidal lithography

Annealed colloidal particles can be harnessed for the fabrication of nanostructures via the so-called natural lithography or colloidal lithography or nanosphere lithography process. In this case, annealed colloidal particles are used as a mask or template for further processing steps (for instance, etching or deposition of material). As they typically serve as a sacrificial material, they are usually removed at the end of the whole process. For this class of applications, annealing is usually used to tune the size and shape of interstices (also called pores or holes or voids) between neighbouring particles.

For example, thermally annealed PS colloidal monolayers have been used as a mask for the fabrication of zero mode waveguides for single molecule fluorescence studies [155]. Fig. 16(a) shows a sketch of the process. Thermal annealing was carried out on 1 μm diameter PS particles. By controlling the annealing time at an annealing temperature of 107 °C, the size of the pores between particles could be tailored in the range of 350–100 nm (Fig. 16(b)), which is essential for constructing waveguides with cut-off wavelengths in the visible range appropriate for experiments with the most commonly used probes for single molecule fluorescence [155]. In addition, the thermal annealing treatment turns the nearly triangular holes into nearly circular interstices: a round cross-section is also important because in non-centrosymmetric waveguides, the transmission is polarization sensitive, which could compromise the attenuation of the zero mode waveguides or cause their fluorescence to be sensitive to the orientation of the macromolecules [155]. Such structures have been used for fluorescence resonance energy transfer (FRET) on ribosomes programmed with a biotinylated mRNA immobilized in the wells of Al zero mode waveguide arrays (Fig. 16(c)) [155].

ZnO nanowire/nanorod arrays for field emission devices with low turn-on electric field have been fabricated by carrying out electrochemical deposition on PS colloidal monolayers assembled on indium tin oxide (ITO)-glass substrate or heavily doped Si substrates and heated at 110 °C for different times (1–10 min) to introduce a different extent of deformation in a hot air oven [125]. Different degrees of template deformation were introduced under heating near T_g by tuning the thermal annealing time. In fact, upon annealing, the interstices among three neighbouring PS spheres become well defined and separated by the connection of the edges of the spheres [125]. Such changes affect the subsequent growth of nanowires and nanorods [125]. Experimental results show that the heating time affects the arrangement and morphology of ZnO nanowires/nanorods and, eventually, the field emission performance [125]. In fact, when a non-annealed monolayer is used, only network-like pore or wall-like arrays can be obtained (Fig. 16(d)) [125]. By contrast, when using a slightly deformed template, the growth of well-separated nanorods occurs due to the deformation-driven separation of voids within the template (Fig. 16(e)) [125]. If the

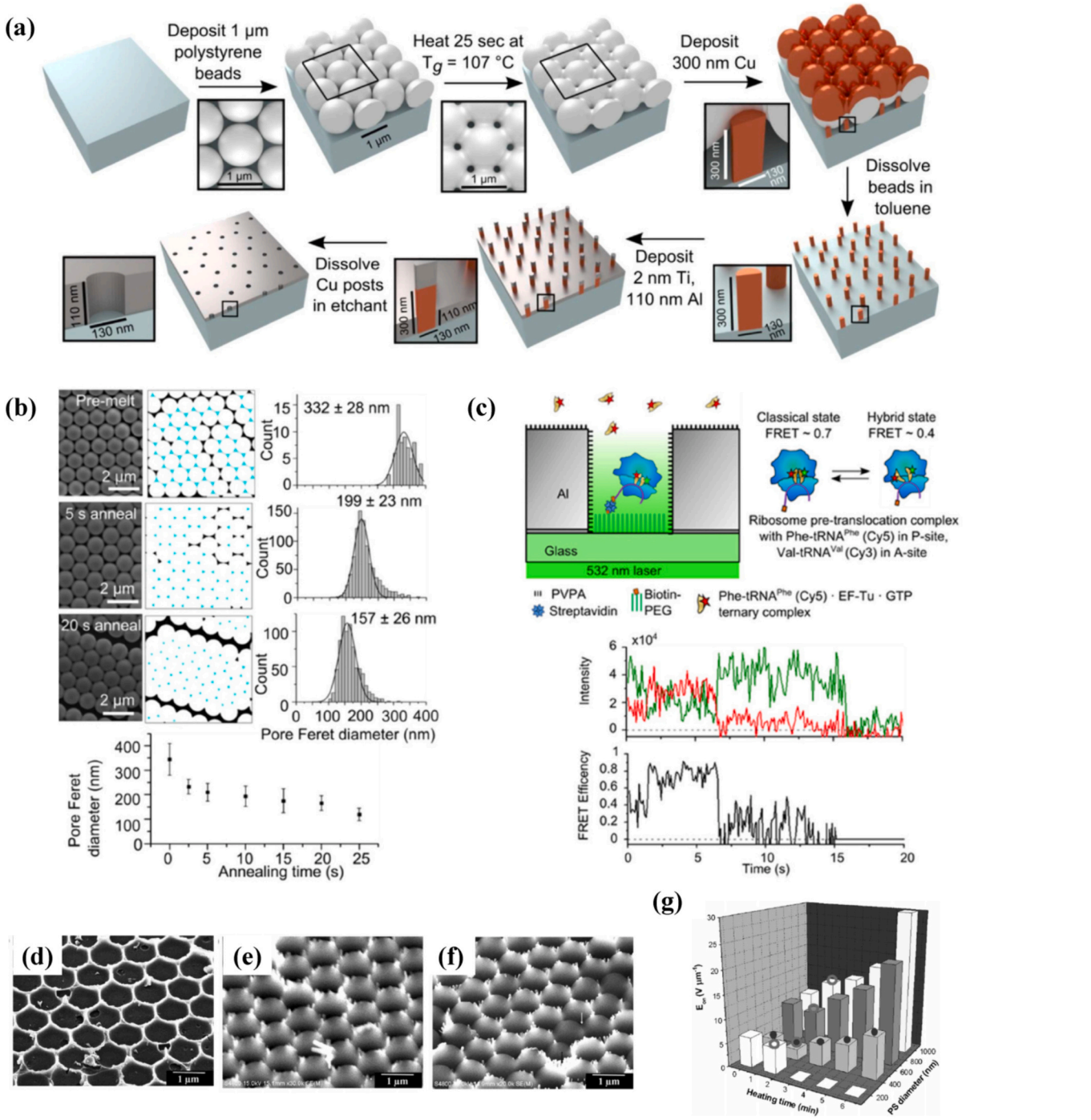

Fig. 16. - Applications of annealed colloidal particles: (a) sketch of the process of fabrication of zero mode waveguides (reprinted from [155], Copyright © 2019 Jamiolkowski et al. https://doi.org/10.1371/journal.pone.0222964); (b) SEM images of PS particles for variable annealing time and corresponding image processing to identify interstitial areas (in cyan) (reprinted from [155], Copyright © 2019 Jamiolkowski et al. https://doi.org/10.1371/journal.pone.0222964); (c) sketch of the principles and experimental results of fluorescence resonance energy transfer (FRET) on ribosomes programmed with a biotinylated mRNA immobilized in the wells of Al zero mode waveguide arrays (reprinted from [155], Copyright © 2019 Jamiolkowski et al. https://doi.org/10.1371/journal.pone.0222964); (d) network-like pore or wall-like arrays of ZnO nanorods without annealing (reproduced from [125], with permission, copyright 2009, John Wiley & Sons); (e) well-separated ZnO nanorods in case of 1.5 min annealing (reproduced from [125], with permission, copyright 2009, John Wiley & Sons); (f) extensive ZnO nanorod growth followed by nanorod bundling in case of 3 min annealing (reproduced from [125], with permission, copyright 2009, John Wiley & Sons); (g) dependence of turn-on electric field on PS diameter and PS heating time for ZnO nanorod array anodes (reproduced from [125], with permission, copyright 2009, John Wiley & Sons). (For interpretation of the references to colour in this figure legend, the reader is referred to the web version of this article.)

deformation is excessive as occurs for longer thermal treatments, some voids in the colloidal template fully disappear due to PS fusion and, consequently, no nanorod is grown on these sites; simultaneously, the other void areas become larger due to PS migration, leading to extensive nanorod growth followed by nanorod bundling (Fig. 16(f)) [125]. In this way, uniformity, density and patterning of nanorod arrays can be controlled using deformation-tailored templates, with a consequent impact on the performance of the final devices [125]. In fact, with

template heating time increasing, the turn-on field first decreases and then dramatically increases [125]. As previously described, the nanorod separation within the arrays can be improved by slight deformation of a template with heating time below 1.5 min [125]. Such moderate spacing of nanorods in a local area entails a reduction in the screening effects, increasing the emitting efficiency [125]. On the other hand, the excessive heating results in the absence of nanorods in some places and their bundling in others [125]. The former reduces the overall density of the array, whereas the latter increases the local screening effect, thereby decreasing the emitting efficiency [125]. Fig. 16(g) shows the dependence of turn-on electric field on PS diameter and heating time.

Periodic Fe_2O_3 pillar arrays have been fabricated by nanosphere lithography on PS particles sintered at 120 °C for a certain time, then taken out of the oven and cooled to room temperature: a droplet of Fe $(NO_3)_3$ solution was applied onto the sintered colloidal monolayer to infiltrate into the interstices among PS particles; after drying, annealing at 400 °C for 2 h was carried out to make the precursor decompose completely and the PS particles template to be burnt out to create the final array; the final characteristics can be controlled by the annealing time [156,157].

Porous PDMS surfaces have been fabricated using PS particles as templates: polystyrene microspheres were self-assembled on a substrate pre-coated with a thin layer of polystyrene and heated at an appropriate temperature, prior to infusion of a polymer precursor solution into cavities of the spherical particles of the template, solidification of the polymer and removal of the particles; the surface pore sizes can be tuned by varying the temperature and time for the heat treatment (Fig. 17(a)) [158].

For colloidal monolayers annealed by microwave irradiation, by performing material deposition by an electron beam evaporation system allowing control over both the evaporation angle and sample rotation, structures such as honeycomb arrays of cobalt (Co) nanodots and iron (Fe) nanorings and nanorods have been realized and their magnetic properties have been characterized [124] (Fig. 17(b)).

Thermal treatments have also been used for the fabrication of uniform non-closely-packed particle arrays starting from silica/polymer core/shell particles: silica/PMMA core/shell particles were first assembled on a substrate electrostatically and subsequently immobilized by heating above T_g of the shell polymer; particle arrangement was shown to be more uniform compared to the case where heat treatment was not performed; the influence of the shell material was also investigated, in particular the effect of polymer cross-linking [159].

Special masks for nanosphere lithography have been produced by sintering of monolayers of PS-*co*-PDVB copolymer colloidal particles (500 nm) and selective dissolution, with morphological characteristics tunable via proper calibration of the sintering conditions [160]. Particles consist of cross-linked polydivinyl benzene (PDVB) as the insoluble portion and PS as the portion soluble in cyclohexane [160]. Two different structures were obtained according to sintering temperature (whether colloidal arrays were sintered for 30 min either at 123 °C, i.e. the glass transition temperature of the colloids, or at 140 °C) (Fig. 17(c)) [160]. Sintering at 140 °C caused the formation of necks, indicated in green in Fig. 17(c), due to active polymer chain mobility, with migration of the uncrosslinked fraction of colloids being dominant [160]. Subsequently, the sintered colloids were selectively dissolved in cyclohexane at 40 °C for 2 h [160]. Selective dissolution of the colloidal array sintered at 123 °C gives rise to an ordered array of spheres of 320 ± 55 nm, in which each sphere has three nearest neighbours, whereas selective dissolution of the array sintered at 140 °C gives an ordered array of rods in which each rod (width 150 ± 6 nm, length 220 ± 16 nm) has four nearest neighbours [160]. Their morphology can be explained as follows [160]:

- in case of structure A, the colloids have no necks between them and, consequently, as the dissolution proceeds, insoluble PDVBs are trapped in the triangular interstices between neighbouring colloidal particles; hence, the selective dissolution results in spherical nanostructures due to the symmetry of the triangular interstices;
- in case of structure B, as cyclohexane dissolves the colloids, the insoluble PDVBs move and are adsorbed on the necks where relatively strong physical cross-links of polymer chains could exist and PDVBs are intermingled with the necks; the necks are converted into rods during selective dissolution.

Also monolayers annealed at the air/water interface can serve as a mask for nanosphere lithography.

For example, monolayers thermally annealed at the air/water interface have been used as a mask for silver deposition for the fabrication of plasmonic structures for surface-enhanced Raman scattering (SERS), whose response can be tuned by playing with the size and shape of the interstices, as revealed by measurements on rhodamine 6G [150].

When colloidal particles are exploited as a template for nanostructure fabrication, monolayers or few layers of particles are typically used; however, for some applications, thicker 3D particle assemblies can be used. For instance, sintered colloidal assemblies can also be exploited for the fabrication of inverse opals.

In [161], sintered 3D assemblies of silica colloidal particles have been used as a template for the fabrication of optically active and tunable TiO_2 structures. To this end, 10 μm thick silica opal templates (460 nm silica particle diameter) were first assembled on silicon substrates; next, for the realization of a non-closely-packed inverse opal, the opal template was first sintered at 1000 °C for 3 h, stronger than typical sintering treatments of 800 °C for 2 h, in order to cause partial collapse of the template and increase of sinter-neck diameter [161]. Subsequently, TiO_2 was conformally deposited in the very small air voids (smaller than 10 nm) using atomic layer deposition, in order to fully and homogeneously infiltrate nanoporous structures for a uniform infiltration of the narrow air channels of the sintered opal [161]. The infiltrated sample was heated to 400 °C for 2 h to convert the amorphous TiO_2 into the anatase phase, before ion milling of the top surface to expose the silica template and etching in HF solution to remove silica particles [161] (Fig. 17(d-e)). The final optical properties can be precisely tuned by backfilling the modified inverse-opal template with increasing TiO_2 depositions [161]. In comparison to typical inverse opals, this procedure resulted in an ultralow filling fraction, structurally stable inverse opal with a much larger sinter neck diameter, allowing the formation of cylindrical or hyperboloid-like connections between the air spherical cavities [161].

It is noteworthy to observe that, for those applications in which colloidal particles need to be removed at the end of the process, one should consider that annealing also affects the dissolution of polymer colloidal films in organic solvents [162]. Dissolution coefficients of polystyrene particle films annealed at different temperatures have been computed from fluorescence studies [162]. Fig. 17(f) illustrates the dissolution coefficients D_d for PS particle films annealed for 10 min for temperatures above T_g of PS. At low annealing temperatures, the film still owns individual particles or small chains [162]. However, at higher annealing temperatures, polymer chains relax and form mechanically strong continuous films, which dissolve much more slowly due to the resistance of the polymer film to the solvent molecules; as a result, D_d values are found to be much smaller [162].

One should also bear in mind that the thermal treatment itself can be exploited for the elimination of the colloidal particles in applications in which they serve as a sacrificial material for templating. For example, in [163], a hexagonal closely packed (hcp) PS colloidal monolayer was used as a mask for gold deposition, resulting in a honeycomb pattern of gold quasi-nanotriangles and a hexagonal pattern of Au-coated PS particles. Subsequent thermal treatments of the Au-coated colloidal monolayer template at elevated temperatures (<350 °C) led to decomposition of the PS spheres, while preserving the position of the PS spheres during the thermal deformation and decomposition process [163]. Finally, Au film evaporated on the PS spheres was loaded onto the

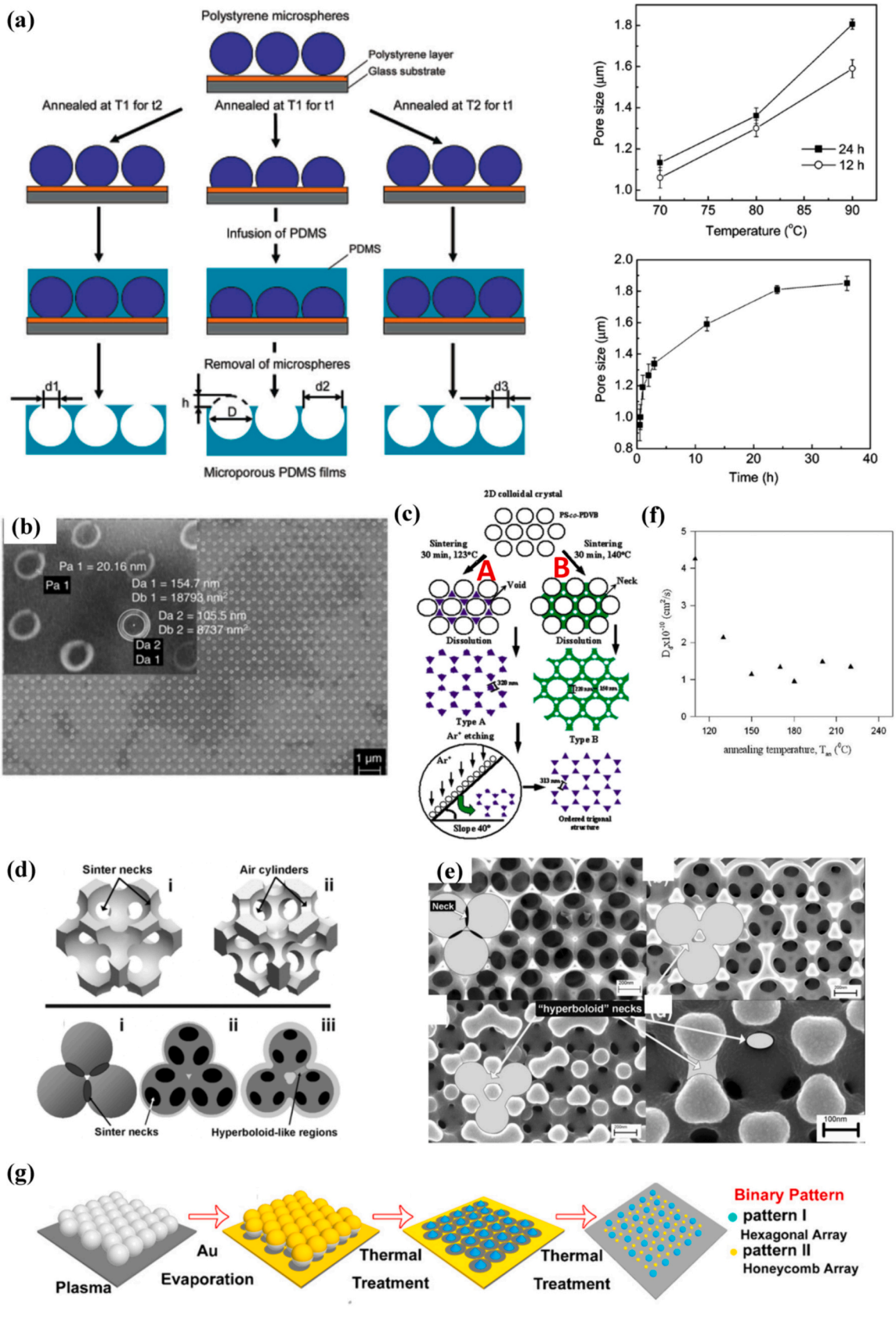

(caption on next page)

Fig. 17. - Applications of annealed colloidal particles: (a) sketch of the process of fabrication of a porous polymer film with tunable pore sizes on its surface (on the left); the pore sizes can be tuned via heat treatment at different temperatures (T1, T2) for different times (t1, t2); size of the pores on the surfaces of porous PDMS films (using 2.68 μm polystyrene microspheres as a template) as a function of the temperature for heat treatment (for 24 h and 12 h) and of the time for heat treatment (at 90 °C) (on the right) (reprinted with permission from [158]. Copyright 2007 American Chemical Society); (b) SEM image of ordered Fe nanorings evaporated over an annealed 540 nm PS colloidal mask; the outer diameter of the individual ring is 150 nm and the width is 20–30 nm (reproduced from [124], with permission, copyright 2005, John Wiley & Sons); (c) sketch of the fabrication process of two different structures (A and B) depending on the sintering temperature (reproduced from Ref. [160] with permission from the Royal Society of Chemistry; https://pubs.rsc.org/en/content/articlelanding/2003/cc/b300638g); (d) sketch of the process of fabrication of optically active and tunable TiO_2 structures based on templates of sintered 3D assemblies of silica colloidal particles (reproduced from [161], with permission, copyright 2006, John Wiley & Sons); (e) SEM images of ion-milled cross sections of the structures produced by the method illustrated in (d) (reproduced from [161], with permission, copyright 2006, John Wiley & Sons); (f) plot of the dissolution coefficient D_d as a function of the annealing temperature (reprinted from [162], Copyright 2004, with permission from Elsevier); (g) sketch of the fabrication process of plasmonic arrays exhibiting a binary pattern (one with honeycomb symmetry and one with hexagonal symmetry) (reprinted with permission from [163]. Copyright 2014 American Chemical Society).

substrate, which accurately occupied the original position of the PS [163]. Dewetting process of the Au film took place at high heating temperatures (>400 °C), resulting in the transformation of the Au film originally deposited on the PS spheres into Au structures, with the original hexagonal symmetry of the PS particles [163]. In this way, plasmonic arrays exhibiting a binary pattern (one with honeycomb symmetry and one with hexagonal symmetry) could be produced [163]. The procedure is sketched in Fig. 17(g).

7.2. Direct use for intrinsic physical properties

Annealing of colloidal particles can be directly exploited to get materials with properly tailored physical properties (optical, thermal, mechanical). In fact, thermal annealing has a direct impact on different material properties, which has been exploited first for the analysis of the annealing process and then for their practical applications.

It is noteworthy to observe that the onset of dry sintering is related to the glass transition temperature in the case of polymer colloidal crystals [164]. At this point, an abrupt change in both the optical and thermal properties occurs, corresponding to the structural degradation process [164]. The concomitant loss of contrast and periodicity reduces both photonic opalescence and thermal insulation properties of 3D arrangements of polymer particles [164]. Mechanical properties are also affected by thermal treatment.

Also for silica particle arrays, the pore size and the connectivity of colloidal lattices are important parameters that largely affect their mechanical and optical properties as well as the diffusion of fluids through them [165].

7.2.1. Optical properties

One possible application of thermal annealing of 3D structures composed of multilayers of colloidal particles is to tailor the optical response of photonic crystals. In fact, the spectral response is influenced by the colloidal particle size, the refractive index of the colloidal particle material, the refractive index of the material in the interstices between colloidal particles and the filling fraction or volume fraction, i.e. the ratio between the volume occupied by the colloidal particles and the total volume of the structure [133,166,167]. The latter can be modified via thermal annealing [133]. More specifically, highly ordered, periodic structures can strongly diffract light, exhibiting a stop-band in their transmission spectrum, whose characteristics are related to specific morphological features of the colloidal crystals [168]:

- mid-gap position: determined by the pitch of the periodic structure, i.e. the center-to-center distance between neighbouring particles;
- maximum attenuation of the stop-band: determined by the number of particle layers along the direction of propagation of light and the refractive index contrast between the particles and the matrix material;
- width of the stop-band: determined by the refractive index contrast and the packing structure of the colloidal lattice.

The possibility to control the spectral response of colloidal crystals via thermal annealing has been demonstrated for both silica and polymer particles. In opals, the volume packing fraction of spherical colloidal particles can be brought from the face-centered cubic (fcc) close-packed value 0.74 to unity by thermal annealing [169].

As we have seen in section 4.2, tracking variations in optical properties of 3D colloidal assemblies can be used to get insight into morphological variations upon thermal treatment. At the same time, such shaping effects can be directly employed for optical applications. In particular, in [133], accurate control over the optical properties of silica colloidal photonic crystals (diameter 415 nm) has been achieved via thermal annealing, which induces strong structural and physicochemical modifications without loss of order. Characterization was performed by computing transmission spectra at normal incidence: the intense attenuation band shifts towards lower wavelengths as the temperature increases [133]. As we have seen in section 4.2 and Fig. 10(b), by plotting the central wavelength of this minimum λ_c as a function of temperature, a decay has been observed for samples treated at temperatures between 100 °C and 200 °C; afterwards, λ_c stabilizes until about 400 °C; for temperatures between 400 °C and 700 °C, λ_c gradually shifts downwards, until remaining unaltered between 700 °C and 950 °C; at higher temperatures, a rapid blue-shift occurs simultaneously with an intensity decrease; no bands are observed in case of annealing at 1100 °C [133]. The overall wavelength shift between non-annealed samples and samples annealed at 1050 °C is 111 nm, i.e. corresponding to a variation of 11% in the Bragg reflected wavelength [133]. For particles smaller than 300 nm, diffraction effects are observed in the visible range [133]. Fig. 18(a-b) show photographs of untreated and thermally treated samples taken by white light illumination at normal incidence using an optical microscope operating in reflection mode and the corresponding optical transmission spectra; the reflection wavelength depends on the thermal treatment and shifts from 628 nm for the non-annealed sample to 561 nm at 1050 °C [133]. The wavelength λ_c can be fitted with the following equation for normal incidence [133]:

$$\lambda_c = 2d_p\sqrt{\varepsilon_{ave}} \tag{15}$$

where d_p is the distance between crystalline planes responsible for that direction and ε_{ave} is the average dielectric constant of the structure. This equation has been used to cast light on morphological and physical properties of the structure upon annealing.

Compared with their inorganic counterparts (e.g. silica colloids), the spectral response of polymeric systems could be easily tuned by annealing them at much lower temperatures, usually below 100 °C (depending on the glass transition temperature of the polymer) in contrast to 500–1000 °C for silica [168]. The lower temperatures allow a more straightforward infiltration of a variety of materials into the interstices among colloidal particles to further tune the band-gap properties by changing the dielectric contrast [168].

In [168], engineering of the optical properties of colloidal crystals of 230 nm PS particles via thermal annealing has been investigated. Differently from [165], where particles were annealed fundamentally in air, PS particles were always surrounded by water during the annealing process; in addition, the confinement within a cell allowed the accurate measurement of the change in attenuation as the sample was annealed at

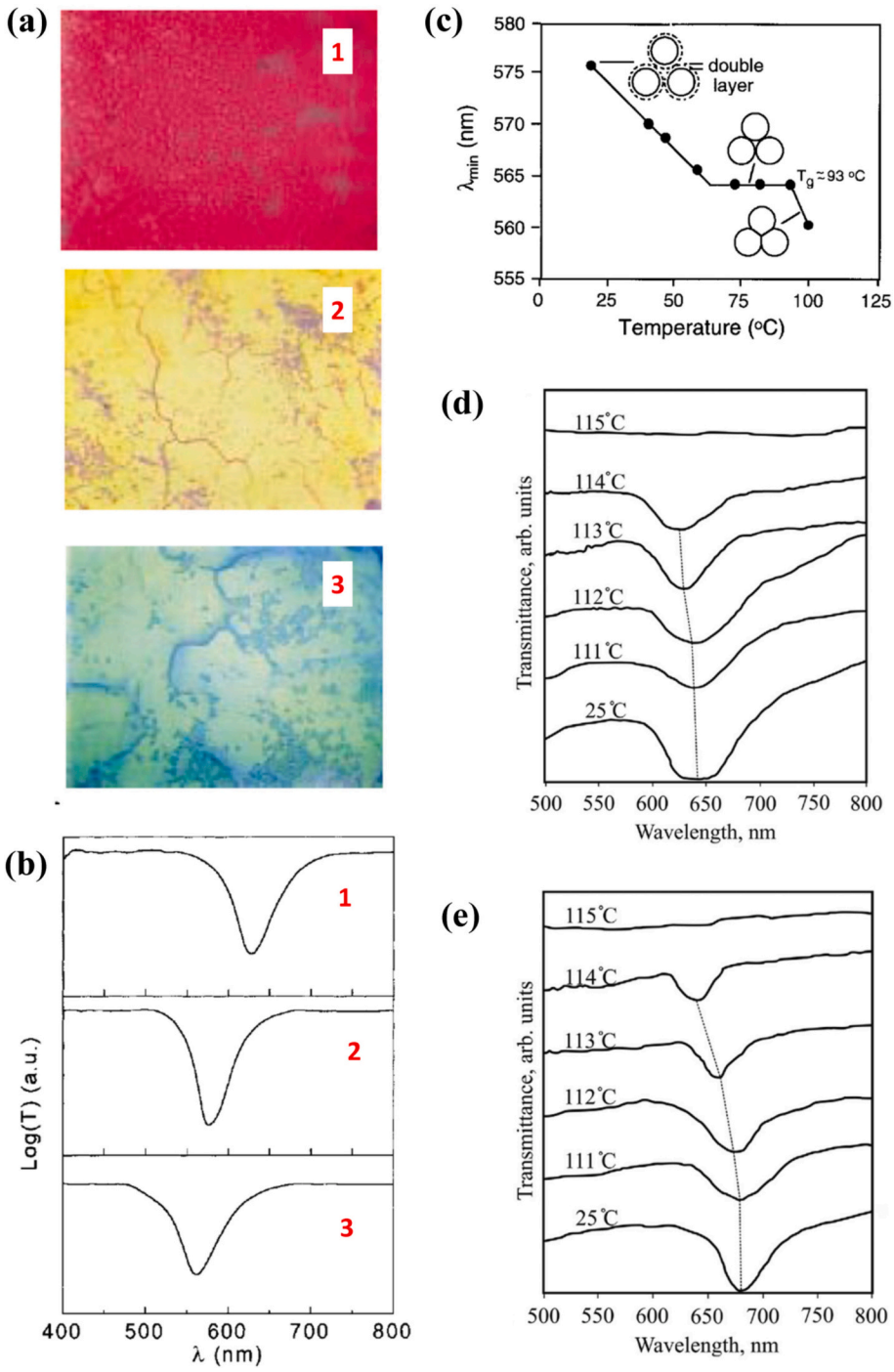

Fig. 18. - Applications of annealed colloidal particles: (a) optical microscope images in reflection mode of 260 nm diameter silica spherical particles: (1) as-grown, (2) treated at 950 °C, and (3) treated at 1050 °C, spanning the following areas (1) 0.65 × 0.55 mm^2, (2) 0.32 × 0.28 mm^2, (3) 0.13 × 0.11 mm^2; the difference in colour is due to the different range of wavelengths reflected (reproduced from [133], with permission, copyright 1998, John Wiley & Sons); (b) optical transmission spectra obtained at normal incidence for a sample made up of 260 nm diameter silica spherical particles: (1) as-grown, (2) treated at 950 °C, and (3) treated at 1050 °C (reproduced from [133], with permission, copyright 1998, John Wiley & Sons); (c) mid-gap position as a function of the annealing temperature and sketch of the morphological evolution mechanism; the sample was annealed at each data point for 1 h; below the glass transition temperature of polystyrene (approximately 93 °C), the mid-gap position was largely controlled by the annealing temperature; above the glass transition temperature, the mid-gap position was mainly dependent on the annealing time (reproduced from [168], with permission, copyright 2000, John Wiley & Sons); (d) effect of annealing temperature on the position of the photonic stop-band of a photonic crystal made up of PS microspheres without ethanol (reprinted from [126], Copyright 2017, with permission from Elsevier); (e) effect of annealing temperature on the position of the photonic stop-band of a photonic crystal made up of PS microspheres filled with ethanol (reprinted from [126], Copyright 2017, with permission from Elsevier).

various temperatures for different periods of time [168]. By annealing at temperatures in the range of 20 to 100 °C, the position of its stop-band was continuously blue-shifted from approximately 576 to 548 nm and the attenuation of this stop-band was reduced in a controllable fashion; the appearance of new stop-bands was also observed in the UV–vis transmission spectra when the sample was subjected to annealing at temperatures higher than T_g of polystyrene (about 93 °C) [168]. Fig. 18 (c) illustrates the mid-gap position versus the temperature at which the sample was successively annealed at each data point for 1 h; the following conclusions were drawn, with the individuation of three distinct stages [168]:

- from room temperature to about 62 °C, the mid-gap position was blue-shifted from 576 to 564 nm at a rate of approximately 0.28 nm/°C and the magnitude of this shift was insensitive to total annealing time; during this stage, an increase in the temperature causes a shrinkage in the thickness of the double layer, and thus a reduction in the hydrodynamic size of the particles, as well as in the center-to-center distance between the PS particles;
- from about 62 °C to T_g, the mid-gap position was constant at 564 nm; during this stage, no further change in the center-to-center distance was observed once the particles had reached a state in which they are all in physical contact;
- above T_g, the mid-gap position was blue-shifted again but, in this case, the magnitude of the variation was chiefly determined by the annealing time; during this stage, the center-to-center distance between particles is further reduced as a result of their viscoelastic deformation; the intrinsic forces of surface tension deform the particles into space-filling shapes; as the temperature increases, the contact area among neighbouring particles increases, with a consequent increase in the density of the crystalline array; the polymer particles will eventually be fused into a uniformly dense body that is transparent over the entire UV–vis region.

In [126], the effect of the annealing temperature on the optical properties has been investigated for photonic crystals consisting of multilayers of PS (diameter 270 nm) or silica (diameter 275 nm) particles. Annealing was carried out for one hour at fixed temperatures in the range 60–115 °C for PS particles and for five hours at fixed temperatures in the range 100–1000 °C for silica particles [126]. After thermal treatment, the transmission spectra of the modified colloidal crystals were measured without filling and saturated with a liquid of known refractive index, in particular ethanol for PS and water for silica; the liquid fills the photonic crystal pores under the action of capillary forces [126]. The spectral position of the photonic stop-band of bare PS particles does not show any major change after annealing in the range 25–110 °C; an increase in the annealing temperature leads to a spectral blue-shift; furthermore, stronger spectral shifts are observed in samples impregnated with ethanol, until the complete disappearance of the dip for annealing temperatures higher than 115 °C [126] (Fig. 18(d-e)). In case of silica photonic crystals, an appreciable shift in the spectral dip is observed already from 500 °C; for temperatures higher than 960 °C, the periodic structure is completely impaired due to silica sintering [126]. The deformation of the colloidal particles for the two different materials was estimated from the transmission spectra at normal incidence from the following equation (derived from Bragg law and effective medium approximation):

$$f_{part} = \frac{\lambda_1^2 n_{liq}^2 - \lambda_2^2}{\lambda_2^2\left(n_{part}^2 - 1\right) - \lambda_1^2\left(n_{part}^2 - n_{liq}^2\right)} \tag{16}$$

where f_{part} is the volume fraction occupied by the particles, λ_1 and λ_2 are the wavelengths of the transmission minima for unsaturated and liquid-saturated photonic crystals, n_{part} and n_{liq} are the refractive indices of the particle material and of the filling liquid [126]. The volume fraction occupied by PS and silica particles for variable annealing temperature is shown in Fig. 19(a-b). In case of PS, for temperatures up to 110 °C, the volume fraction is 0.71 close to the theoretical value for close-packing; partial particle sintering occurs between 110 and 114 °C, resulting in an increase in the volume fraction; at 115 °C complete sintering occurs with the consequent disappearance of the photonic stop-band [126]. In case of silica particles, for temperatures up to 500 °C the volume fraction exhibits only minor variations (even if, in this case, the volume fraction was much lower than the theoretical value due to the higher polydispersity of the investigated silica particles in comparison with PS); between 500 and 920 °C, the volume fraction increases due to the beginning of sintering with consequent reduction of the voids; between 920 °C and 1000 °C, the volume fraction of silica increases more dramatically [126].

Reversible thermal tuning of the photonic band-gap position has been observed in PS particle colloidal crystals for temperatures up to T_g (about 85 °C) [170]. A non-linear behaviour in the blue-shift in the band-gap position was observed, attributed to the non-linear thermal behaviour of the synthesized PS particles [170]. The relative packing density of the photonic crystal structures changed from approximately 74% at room temperature to about 76% at 55 °C and 86% at 90 °C [170]. At 90 °C, particles take on a polyhedral shape, while, for increasing temperatures, they tend to form a uniform thin film (particle melting point at approximately 103 °C) [170].

Colloidal photonic crystals with a graded lattice-constant distribution have been produced by annealing of 3D PS particle assemblies (diameter 242 nm) in a graded temperature field, heating one end at about 130 °C for 36 h and keeping the other end at room temperature (Fig. 19(c)) [171]. The band-gap wavelength as well as the attenuation could be varied with the position of the gradient colloidal crystal along the gradient direction because of the lattice constant variation (Fig. 19 (d-e)) [171].

The effect of surface functionalization on the optical properties of 3D silica colloidal assemblies has also been explored, by comparing annealed vinyl-functionalized silica colloidal crystals with pure silica colloidal crystals [172,173].

The modification of optical properties of polymer colloidal crystals upon thermal treatment can be exploited for sensing applications. In fact, clear polymer films can be obtained due to the loss of the refractive index contrast within the structure [56]. For example, manipulation-free and autonomous recording of temperature states for extended periods of time is of increasing importance for food spoilage and battery safety assessment; an optical read-out is preferred for low-tech visual inspection [164]. Time-temperature integrators based on colloidal crystals have been proposed for this purpose, in particular homogeneous colloidal crystals comprising monodisperse poly[(methyl methacrylate)-*random*-(butyl acrylate)] (PMMA-*r*-nBA) colloids via dip-coating from aqueous dispersions [164]. Upon dry sintering, larger contact areas are present between neighbouring particles and the air is expelled from the structure, leading to the loss of the periodic variation of the refractive index; at the same time, the structural colour vanishes and the cracks between crystalline domains become larger to accommodate shrinkage; transmission UV–vis spectra show a slight blue-shift of the photonic stop-band and an even more pronounced decrease of the intensity [164]. By mixing particles with the same size but different T_g (which can be done by varying the percentage of nBA in the copolymer as described in Appendix B and section 4.1), the sintering temperature and, consequently, the variation of optical properties upon temperature can be carefully adjusted [164]. Hence, the thermal response and, consequently, the morphological changes in colloidal particles and the resulting optical response, can be tailored simply by mixing particles at a defined ratio with two distinct glass transition temperatures [164]. Fig. 19(f-h) show examples of decay curves of the stop-band intensity for colloidal crystals with variable percentage of low T_g particles treated at different temperatures for different times [164]. In order to fully exploit the potential of this composition-dependent film formation behaviour,

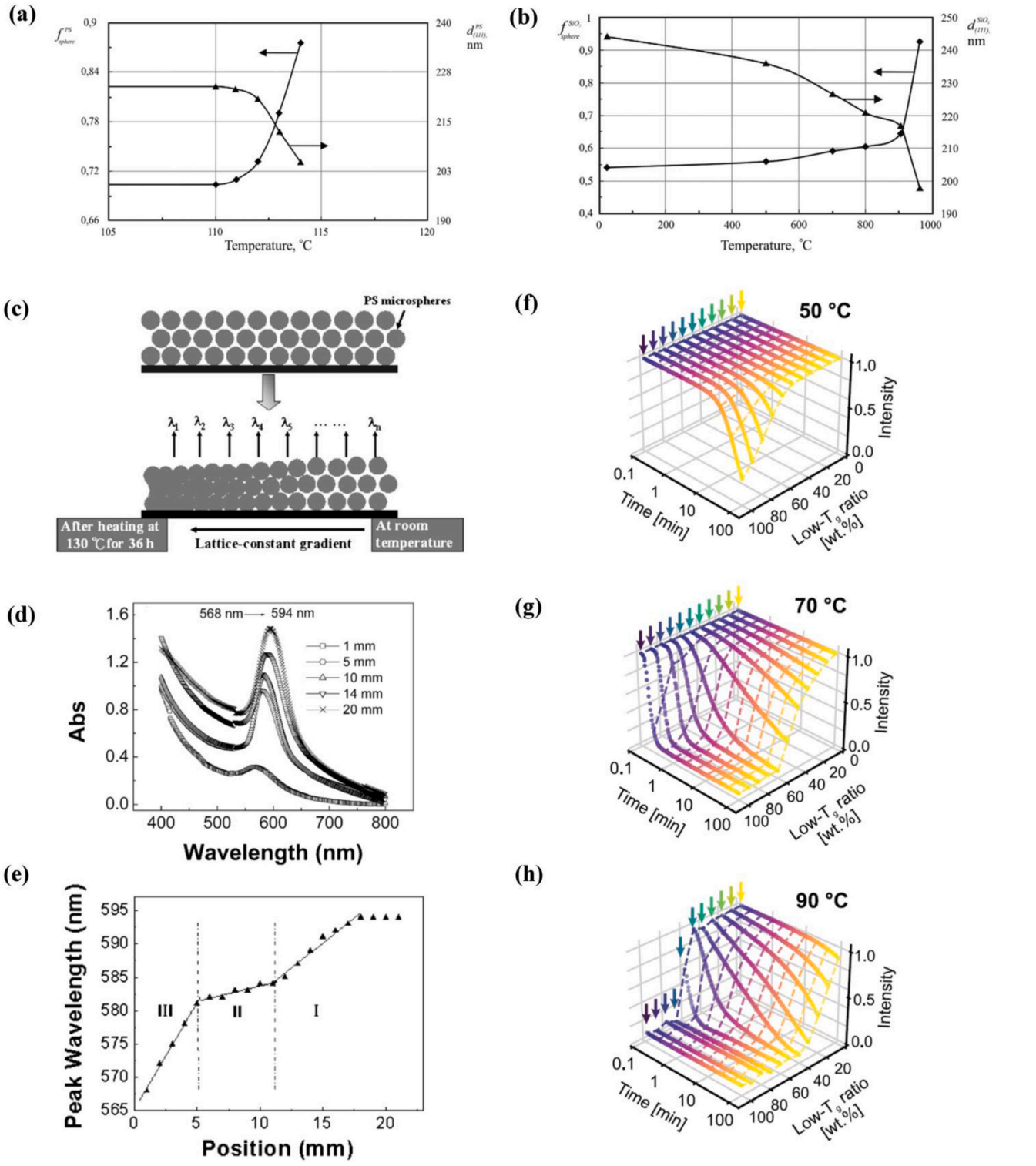

Fig. 19. - Applications of annealed colloidal particles: (a) effect of annealing temperature on the structural parameters of a PS photonic crystal (reprinted from [126], Copyright 2017, with permission from Elsevier); (b) effect of annealing temperature on the structural parameters of a silica photonic crystal (reprinted from [126], Copyright 2017, with permission from Elsevier); (c) sketch of the process of preparation of polystyrene colloidal photonic crystals with a graded lattice constant distribution in a graded temperature field (reprinted by permission from Springer Nature: [171], Copyright 2007, reproduced with permission from SNCSC); (d) position-dependent absorption spectra of the PS gradient colloidal crystal annealed in a graded temperature field from room temperature to 130 °C (reprinted by permission from Springer Nature: [171], Copyright 2007, reproduced with permission from SNCSC); (e) position-dependent stop-band peak of a PS gradient colloidal crystal (reprinted by permission from Springer Nature: [171], Copyright 2007, reproduced with permission from SNCSC); (f-g-h) three-dimensional representation of stopband decay curves for different compositions at temperatures of 50 °C (f), 70 °C (g) and 90 °C (h) (reproduced from [164], with permission, copyright 2021, John Wiley & Sons).

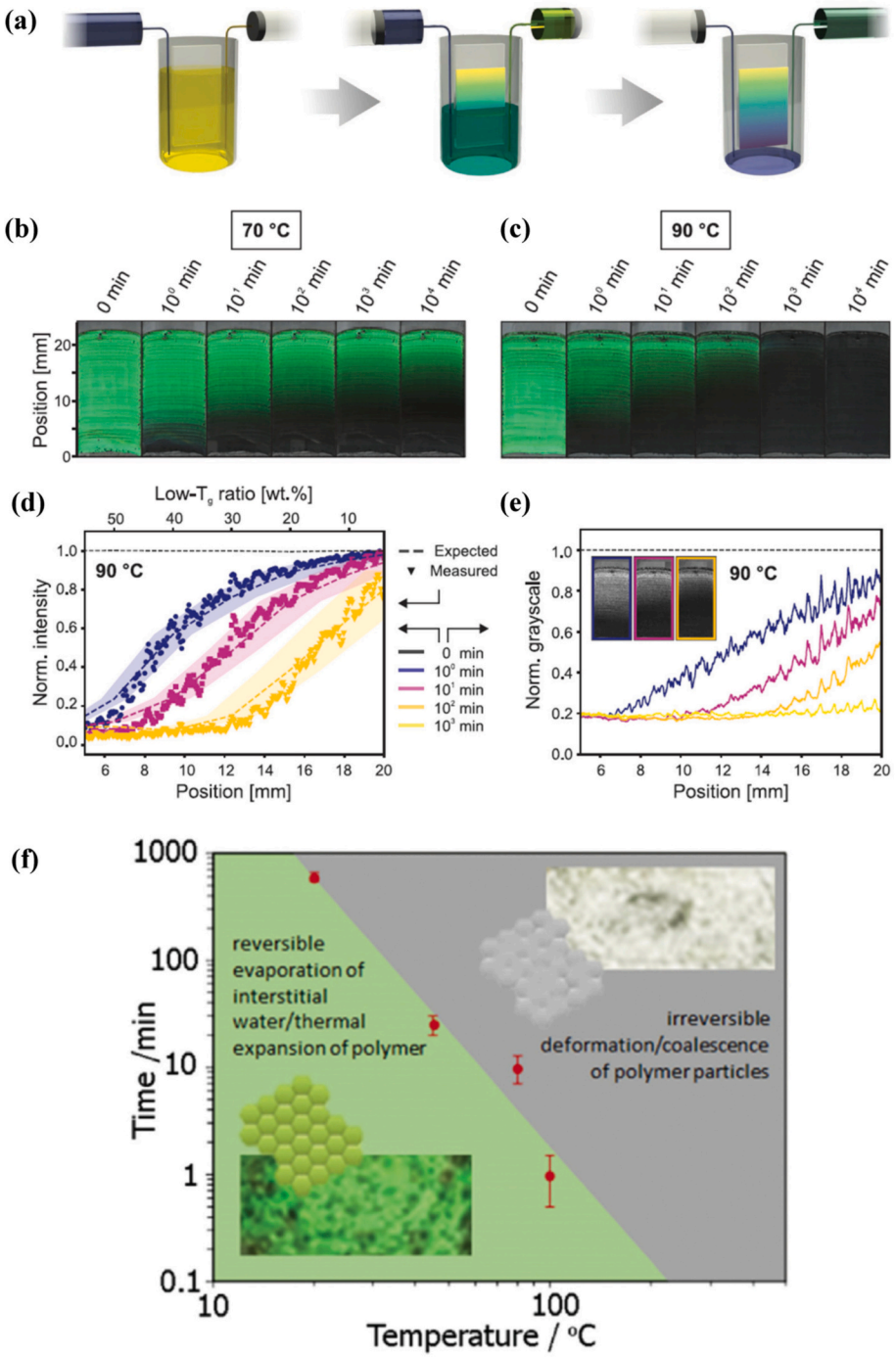

Fig. 20. - Applications of annealed colloidal particles: (a) sketch of the infusion withdrawal coating technique to fabricate gradient colloidal crystals based on the simultaneous infusion and extraction of the colloidal dispersion at different rates leading to a continuous composition gradient; this gradient is coated on the submerged glass substrate by continuous extraction of the mixed dispersion (reproduced from [164], with permission, copyright 2021, John Wiley & Sons); (b-c) colloidal crystals with a gradual change of the ratio of high- and low-T_g particles with identically prepared gradients, but sintering at 70 and 90 °C; images are obtained via stitching of light microscopy images and ex situ during the sintering process; the respective sintering times increase on a logarithmic scale (reproduced from [164], with permission, copyright 2021, John Wiley & Sons); (d) normalized intensity obtained from ex situ UV–vis transmission measurements along the gradient axis (reproduced from [164], with permission, copyright 2021, John Wiley & Sons); (e) normalized grayscale along the gradient axis; the inset shows green-channel images after colour-channel separation of the pictures in (b) (reproduced from [164], with permission, copyright 2021, John Wiley & Sons); (f) graphene based colloidal photonic crystals for time-temperature indicator applications: time versus temperature plot illustrating regimes at which the interfacial structural transitions occur, resulting in an associated colour variation; in the insets, optical photographs of the graphene-doped photonic crystals and sketch of particle boundaries showing the transition of colour from green to transparent (reproduced from [174], with permission, copyright 2020, John Wiley & Sons). (For interpretation of the references to colour in this figure legend, the reader is referred to the web version of this article.)

the binary particles (same size but different T_g) can be arranged in a linear composition gradient colloidal crystal by proper self-assembly techniques, such as infusion-withdrawal-coating, i.e. colloidal crystals with a gradual change of the ratio of high- and low-T_g particles [164]. This can be obtained, for example, using dip-coating with two syringe pumps: a glass substrate is dipped in a dispersion of one particle type, which is extracted with a syringe pump; concomitantly, a second syringe pump infuses a dispersion of the second particles at a slower rate; the water level, thereby, decreases continuously, mimicking dip-coating, while the composition changes in a slow and gradual way (Fig. 20(a)) [164]. Fig. 20(b-e) show the variation in the optical response at different positions along the gradient colloidal crystals, for sintering at different temperatures with different durations [164]. The gradient structures exhibit the expected film-formation kinetic behaviour and, consequently, local change in the intensity of the optical stop-band [164]. The gradual and local transition can be analyzed spectroscopically or through simple image analysis for the purpose of a simple, autonomous and manipulation-free way to assess thermal history of the colloidal gradient [164].

The thermo-optical response of colloidal crystals can be exploited for sensing applications. In particular, thermo-chromic devices based on graphene-infused synthetic opals, i.e. hcp opal-like colloidal crystals (made up of colloidal particles consisting of a random copolymer of methyl methacrylate-MMA, butyl acrylate-BA, methacrylic acid-MAA) containing pristine graphene present at the interstitial sites between particles, have been proposed as integrated time-temperature indicators (TTIs) which act over large temperature windows (from room temperature to 100 °C) [174]. A possible application would be in the field of intelligent packaging to offer a visual indication of whether perishables (such as food, pharmaceuticals, chemicals, inks, paints or coatings) have experienced undesirable time-temperature histories [174]. As we have seen, colloidal crystals undergo change in optical properties and, in particular, also a colour change upon thermal treatment, i.e. a thermochromic effect. The distinct but gradual colour change with time is associated with the loss of refractive index contrast when polymer/polymer boundaries are formed when intervening water is lost [174]. The thermal expansion of polymer particles and interfacial water (both increasing the lattice constant) with increasing temperatures produces a red-shift of the stop-band, which is extremely sensitive to even a small rise in temperature [174]. Depending on the combination of temperature and duration of exposure to a certain temperature, two different regions can be distinguished, one in which the structural change in the colloidal crystal is reversible and one in which it is irreversible [174]:

- in the former case, the crystals can act as smart shape-memory polymers that can memorize and recover their shape and colour after experiencing the external heat stimulus; the temperature of the graphene infused crystals can be repeatedly shifted above and below their glass transition temperature value; each time the crystal experiences elevated temperatures, it gradually relaxes back to the initial shape configuration while, at the same time, exhibiting gradual structural colour change as the stop-band returns to its original pre-deformation value; if the crystals are rehydrated, their colour returns to the original green; in this regime, they are operating close to their MFFT for complete coalescence; hence the particle deformation is incomplete and particle/particle interfaces still exist;
- in the latter case, the diffusion of individual polymer chains across particle/particle boundaries results in irreversible and complete coalescence of the particles; the periodicity disappears and thus Bragg's diffraction does not apply anymore; this means that, at higher temperatures or longer exposure times, there is a certain cut-off point where the crystals lose their colour irreversibly with the stop band completely disappearing; the colour is fully lost when particles coalesce during exposure to high temperatures for prolonged times.

Fig. 20(f) shows a time-temperature phase diagram, where the shaded green region in the figure indicates the conditions at which the TTIs exhibit reversibility and gray-shaded region corresponds to the conditions of irreversible change [174].

7.2.2. Thermal properties

Concerning thermal properties, change in thermal conductivity occurs upon heating above T_g, in particular its increase. For example, the thermal transport of 3D PS colloidal particle assemblies has been characterized via flash laser analysis: such systems are characterized by low thermal conductivity in combination with high density; the high amount of interfaces and their small inter-particle contact area should result in efficient thermal insulation; upon crossing the T_g, film forming takes place, with a decrease in thickness and increase in thermal conductivity, which can be exploited as thermal switch at least in the range of low conducting materials [175].

The small contact points between the particles play a major role in thermal transport within a colloidal crystal because they serve as geometrical constrictions for heat to travel through the material [56]. Hence, their size is crucial for the thermal transport and can be adjusted via thermal treatment: in fact, beyond the glass transition temperature of the polymer, the polymer chains become mobile, resulting in a strong enlargement of the contact points between the adjacent particles and, consequently, to a drastic increase in the thermal conductivity [56]. The principle is shown in Fig. 21(a). By exceeding the T_g of the constituting polymer, the mobility of the polymer chains strongly increases, resulting in a fast sintering of the particles; Fig. 21(b) shows the variation in thermal conductivity for 20 vol% nBA-co-80 vol% MMA colloidal crystals, which increases above T_g in a step-like, irreversible fashion due to a strong enlargement of the particle/particle interfaces [56].

Custom-designed colloidal materials exhibit specific temperature-dependent thermal transport properties with potential interest for thermal switches, transistors or diodes [176]. In fact, common crystalline and amorphous materials are not suitable for this purpose, due to their gradual changes of the temperature-dependent thermal conductivity [176]. Colloidal superstructures made up of copolymer particles of *n*BA and MMA have been proposed for tailored temperature-dependent thermal conductivity [176]. These materials are based on a transition in thermal conductivity for variable temperature, due to the fact that, by exceeding T_g, the thermal conductivity irreversibly increases, as a result of the enlargement of contact points during particle sintering (Fig. 21(c)-1); this unique control over thermal conductivity is only governed by the inter-particle constriction, the particle composition and its mesostructure [176]. The transitions in thermal conductivity can be controlled in different ways; in particular, such systems are characterized by [176]:

- control over transition temperature: as described in Appendix B and section 4.1, by adjusting the nBA content of the particles, it is possible to control the glass transition temperature of the copolymer (Fig. 21(c)-2);
- control over the width of phase transition regime: by assembling the crystal from particles having almost equal size but different T_g; random co-assembly of equal-sized particles but different T_g results in a broad transition, whereas assembly of particles with the same T_g results in a sharp transition (Fig. 21(c)-3);
- possible introduction of multistep transitions (i.e. introduction of multiple discrete transition steps in thermal conductivity): a discrete layer-by-layer assembly of multilayered, freestanding colloidal monoliths in which every layer consists of particles with a predefined T_g; this introduces multiple transition steps of the thermal conductivity by a discrete sintering of the individual layers at the respective T_g (Fig. 21(c)-4);
- control over step height of the transition: by the thickness of the respective layer of particles with a given T_g (Fig. 21(c)-5).

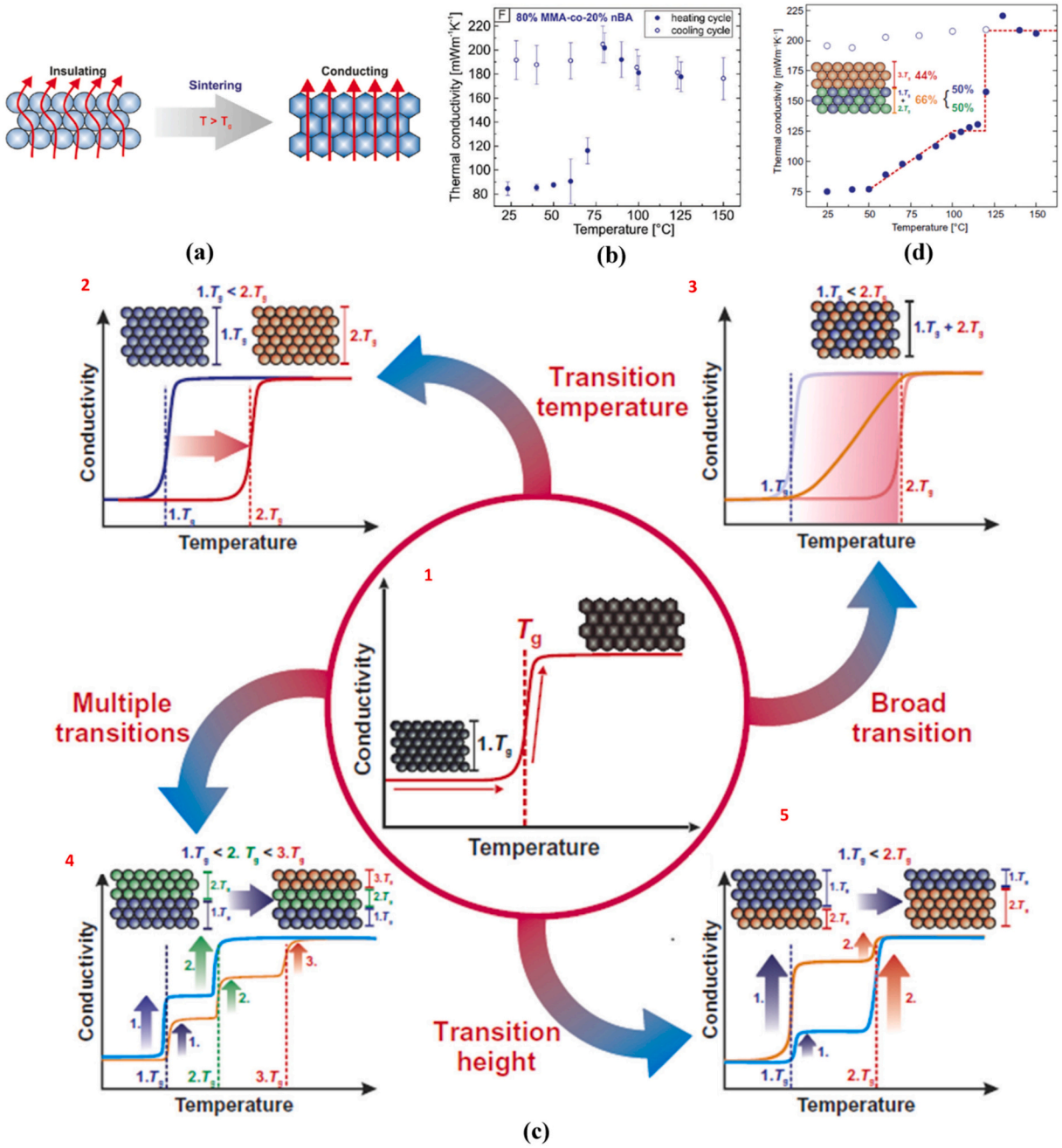

Fig. 21. - Applications of annealed colloidal particles: (a) sketch of the mechanism of increasing thermal conductivity during sintering of a polymer colloidal crystal; due to the small contact points, the crystal is thermally insulating at temperatures below T_g; above T_g the particles deform into dodecahedrons with every facet in full contact to the facet of the neighbouring particle, with a consequent increased thermal transport through the structure (reproduced from Ref. [56] with permission from the PCCP Owner Societies; https://pubs.rsc.org/en/content/articlelanding/2017/cp/c7cp01994g); (b) temperature-dependent thermal conductivity of the colloidal crystal, showing a dramatic increase in the thermal conductivity above T_g of the polymer (reproduced from Ref. [56] with permission from the PCCP Owner Societies; https://pubs.rsc.org/en/content/articlelanding/2017/cp/c7cp01994g); (c) principles of heat management devices and their realization based on constriction-controlled thermal transport in colloidal assembly structures: above T_g, the thermal conductivity irreversibly increases based on the enlargements of contact points during particle sintering (1); the transition temperature can be tailored by assembling the crystal from particles with different T_g (2); the random co-assembly of particles of equal size but different T_g results in a broad transition (3); multiple transition steps can be introduced by a discrete layer-by-layer assembly (4); the height of the transition steps can be controlled the thickness of the corresponding layer (5) (reprinted from [176], Copyright © 2017 The Authors); (d) combination of a broad and a step-like transition; temperature-dependent thermal conductivity of a two-layer colloidal assembly; the bottom layer is fabricated by evaporation-induced self-assembly of two particles having different T_g (90 vol% MMA-2, $T_g = 103$ °C; 70 vol% MMA-2, $T_g = 61$ °C), while the upper layer consists of only one particle type (100 vol% MMA-1, $T_g = 127$ °C); closed symbols represent the heating cycle; open symbols represent the cooling cycle (reprinted from [176], Copyright © 2017 The Authors).

More complex thermal responses based, for instance, on the combination of a broad and a step-like transition can be introduced by proper material engineering (for example, by layer-by-layer deposition of a layer with a mixture of particles with different T_g resulting in a broad transition and a layer of particles with the same T_g resulting in a steep transition) (Fig. 21(d)) [176]. A shortcoming of this simple material composition is the irreversibility of changes of the inter-particle contact area [176].

Microfibers built out of sintered silica nanoparticles (80 nm) with size of 25x150x10000 μm have been shown to exhibit excellent mechanical properties [177]. High-temperature annealing leads to the transformation of low-dimensional colloidal arrays into β-cristobalite structure at 750–800 °C (major product), which further transforms into a mixture of SiO_2 polymorphs at both prolonged heating and cooling [177]. Structures with an anisotropy in thermal conductivity have been proposed starting from these fibers [177]. In the low-temperature zone, the structures with a gradient of morphology (ordering, grain size, porosity) due to temperature gradient along the array length were obtained and characterized [177]. The size of the sintering neck between the nanoparticles and, by this means, the phonon transport properties in the partially sintered ordered nanocrystalline arrays can be changed [177]. A gradient of the phonon transport properties with the length of the nanofiber can also be expected [177]. The microfibers after complete coalescence of nanoparticles in the high-temperature zone are very porous but retain perfect shape with a rectangular cross-section [177].

7.2.3. *Mechanical properties*

The approach generally employed to increase the connectivity of colloidal crystals and, hence, vary also their mechanical properties, is based on the sintering of the particles from which they are made [165].

Preliminary observations above mechanical stability for silica particles were performed in [133]. As pointed out in section 4.2, a contraction of silica particle assemblies was observed at 700 °C with no further contraction up to 950 °C. Nonetheless, the mechanical stability of samples annealed below 700 °C was lower than those treated at temperatures above 700 °C [133]. The formation of necks between the spheres caused by an incipient sintering process starts to occur at temperatures higher than 800 °C through viscous flow and is responsible for the sample strengthening [133]. When samples are annealed at temperatures above 950 °C particles start to crush into each other, losing their spherical shape [133]. Then sample cleavage becomes much more difficult and the spheres that form the resulting internal free surfaces usually present fractures or holes [133]. It is noteworthy to observe that the strong structural modification that occurs above 950 °C does not induce the loss of long-range order and symmetry in the structure [133]. Similarly, by performing thermal annealing at temperatures between

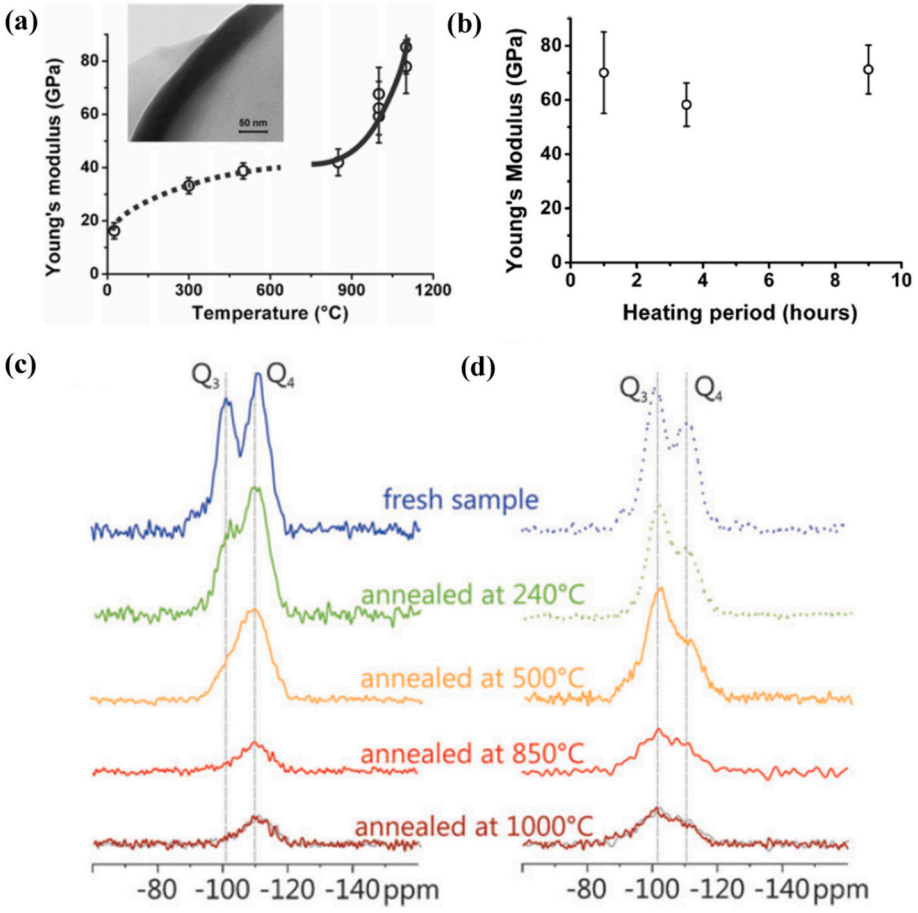

Fig. 22. - Applications of annealed colloidal particles: (a) increase in Young's modulus with annealing temperature until approaching the value of fused silica; in the inset, TEM image of a shell at high magnification (the dark area representing the shell shows uniform thickness) (reproduced from Ref. [179] with permission from the PCCP Owner Societies; https://pubs.rsc.org/en/content/articlelanding/2010/cp/c0cp00871k); (b) Young's modulus as a function of heating period at 1000 °C (reproduced from Ref. [179] with permission from the PCCP Owner Societies; https://pubs.rsc.org/en/content/articlelanding/2010/cp/c0cp00871k); (c-d) ^{29}Si magic-angle spinning nuclear magnetic resonance spectra recorded at 5 kHz MAS spinning frequency and ambient temperature: direct excitation ^{29}Si MAS NMR spectra obtained with 15 s relaxation delay between subsequent transients for the three lower temperatures and 90 s for the two highest temperatures and a low tip angle (c); ^{29}Si cross-polarization magic-angle spinning NMR spectra recorded with 3 ms cross-polarization (CP) contact time and polyvinylpyrrolidone coating of the silica capsules after annealing (d) (reproduced from Ref. [179] with permission from the PCCP Owner Societies; https://pubs.rsc.org/en/content/articlelanding/2010/cp/c0cp00871k).

700 and 1100 °C on silica particles, it was pointed out how this treatment induces the softening of the silica and the occurrence of viscous mass flow processes, which, eventually, provide mass continuity to the structure and decrease the pore size that can be gradually varied with the sintering temperature; a reduction in the center-to-center interparticle distance was also observed; in this way, the mechanical stability of the assembly can be enhanced without disrupting its long range order [165]. Improvement in the mechanical properties of 3D silica particle assemblies due to necking was observed also in [177,178].

Sintering can be exploited to increase the rigidity of 3D colloidal crystals, without losing the pore structure. For example, in [167], 390 nm silica colloidal particles have been heated at 950 °C for 3 h: the sphericity of silica particles was conserved, with a neck developing between particles of approximately 25% of the particle size, making a more rigid structure for optical applications.

Heat treatment can also be exploited to increase the hardness of silica in various applications. For example, high temperature annealing affects the mechanical properties of silica microcapsules (Fig. 22) [179]. Hollow silica spheres were fabricated starting from PS/silica core/shell particles, by dissolution of the PS cores in toluene; afterwards, the silica microcapsules were stored in ethanol and annealed for 3.5 h at temperatures ranging from 240 to 1150 °C; the annealed shells were redispersed in ethanol [179]. The Young's modulus of the shells undergoes a moderate increase upon annealing at temperatures above 500 °C; a much stronger increase is observed for temperatures over 850 °C resulting in a Young's modulus approaching that of fused silica after annealing at 1100 °C [179]. NMR analysis revealed that in untreated microcapsules only 55% of the silicon atoms form siloxane bonds with four neighbours, while the others only form three or less siloxane bonds each and, consequently, a large number of ethoxy and silanol groups still exist; upon annealing at 500 °C, these are successively transformed into siloxane bonds through condensation reactions, a phenomenon that explains only a moderate increase in Young's modulus [179]. The strong increase at temperatures above 850 °C was correlated with a densification, which was accompanied by a decrease in capsule size and shell thickness while the shells preserved a homogenous spherical shape [179]. The main strengthening of the shells was shown to be mostly due to compaction by sintering at length scales significantly larger than that of local siloxane bonds [179]. In contrast to the annealing temperature, the annealing time hardly had any influence on the Young's modulus [179].

In [180], sintering has been applied to enhance the stability of 3D assemblies made up of multilayers of silica larger particles (of diameters between 500 and 1500 nm) with smaller silica nanoparticles (50 nm in diameter) on the top; the samples (deposited on glass substrates) were heated in a furnace under air atmosphere for 30 min at 450 °C to obtain sintered, stable and organics-free silica films and subsequently silanized by self-assembly of a monolayer of dodecyltrichlorosilane so as to obtain hierarchically structured superhydrophobic coatings.

7.2.4. Other applications: Colloidosomes and particles with engineered morphology

Besides the applications to colloidal monolayers and multilayers, thermal annealing can be applied also to spherical dense packings of particles, known as supraparticles or supraballs or colloidosomes [181,182].

Colloidosomes subjected to sintering have been proposed for efficient encapsulation of active ingredients such as drugs, proteins, vitamins, flavours, gas bubbles or even living cells for applications ranging from functional foods to drug delivery to other intriguing biomedical applications [181]. Hollow, elastic capsules, with sizes ranging from micrometers to millimeters and with easily adjusted and highly controllable permeability and elasticity can be produced; the capsule surface is made up of a close-packed layer of colloidal particles, which can be linked together to form a solid shell by sintering (as an alternative to electrostatic interactions and van der Waals forces); the interstices between the particles form an array of uniform pores, whose size can be adjusted to control the permeability via sintering processing parameters [181]. For example, this approach has been applied to a colloidosome made from an oil droplet in an aqueous phase containing 900 nm diameter PS particles locked together by heating at 105 °C for 5 min, slightly above the glass transition temperature of the PS of 100 °C; upon heating, the particles coalesced slightly, creating approximately 150 nm diameter bridges or necks, originating a colloidosome with a precise array of uniform holes in an elastic shell; increasing the sintering time leads to smaller pores, until complete coalescence and full closure of holes after 20 min [181]. By using particles with different T_g, the sintering temperature can be adjusted over a wide range, which might be advantageous for encapsulants incompatible with elevated temperatures [181]. An important feature of colloidosomes, which makes them attractive as encapsulants, is the wide variety of potential mechanisms for release: for instance, release may be triggered by rupture through shear stress, because of the elastic shells [181]. The elastic modulus, and hence the rupture stress, can be controlled by the method of preparation, for instance via the sintering time; in particular, the rupture stress of the colloidosomes increases substantially with longer sintering time [181].

In [182], supraparticles were prepared by rolling $2.5 \pm 0.3\,\mu$m polystyrene sulphate latex particles with $T_g = 106^{\circ}$C on hot superhydrophobic surfaces and underwent annealing to get particle fusion by two different methods:

- hot plate method: supraparticles were placed inside a dry sample tube immersed in an oil bath and heated for two hours by a hot plate, by keeping the temperature of the bath at 107 °C using a temperature probe immersed in the oil and connected to the hot plate control socket;
- dry block heating system: the system with interchangeable heating blocks was set to the desired temperature and a dry sample tube containing the supraparticles was inserted in the heating block; after heating, the supraparticles were cooled to room temperature; heating to temperatures in the range 105–107 °C for two hours led to well-fused composite supraparticles stable in both ethanol and water, while supraparticles heated to 103 °C immediately disassembled when placed in ethanol suggesting lack of fusion.

Concerning the morphology of thermally annealed porous supraparticles the following conclusions were drawn [182]:

- for $T \geq T_g$, PS particles started to melt due to polymer softening and fused together in an aggregate (Fig. 23(a-b)); when the latex particles were partially fused, they showed a glassy appearance and changed their composite colour to yellowish; extensive fusion and melting of the latex particles (e.g. occurring at 120 °C) would block all the pores;
- for $T < 103^{\circ}$C, supraparticles showed poor stability and disintegrated when immersed in a solvent.

Density, porosity and impregnation of supraparticles with liquids were examined within the framework of particle-stabilised emulsions and foams in a range of pharmaceutical, food and cosmetic formulations as well as ore flotation [182].

Reversible behaviour of cohesion between particles in colloidosomes has been exploited for encapsulation and release of small molecular drugs [183]. This behaviour has been observed in colloidosomes formed via tightly bound monodisperse core/shell structured nanoparticles (CSNPs), composed of PS or PMMA cores and amphiphilic polymeric shells (based on polyethylene glycol-PEG segments) with a low melting point (lower than the boiling point of normal solvents) (Fig. 23(c-e)) [183]. This solution has been proposed to circumvent the problem of control over inter-particle spacing in case of small molecule encapsulation when particles are weakly locked together by electrostatic

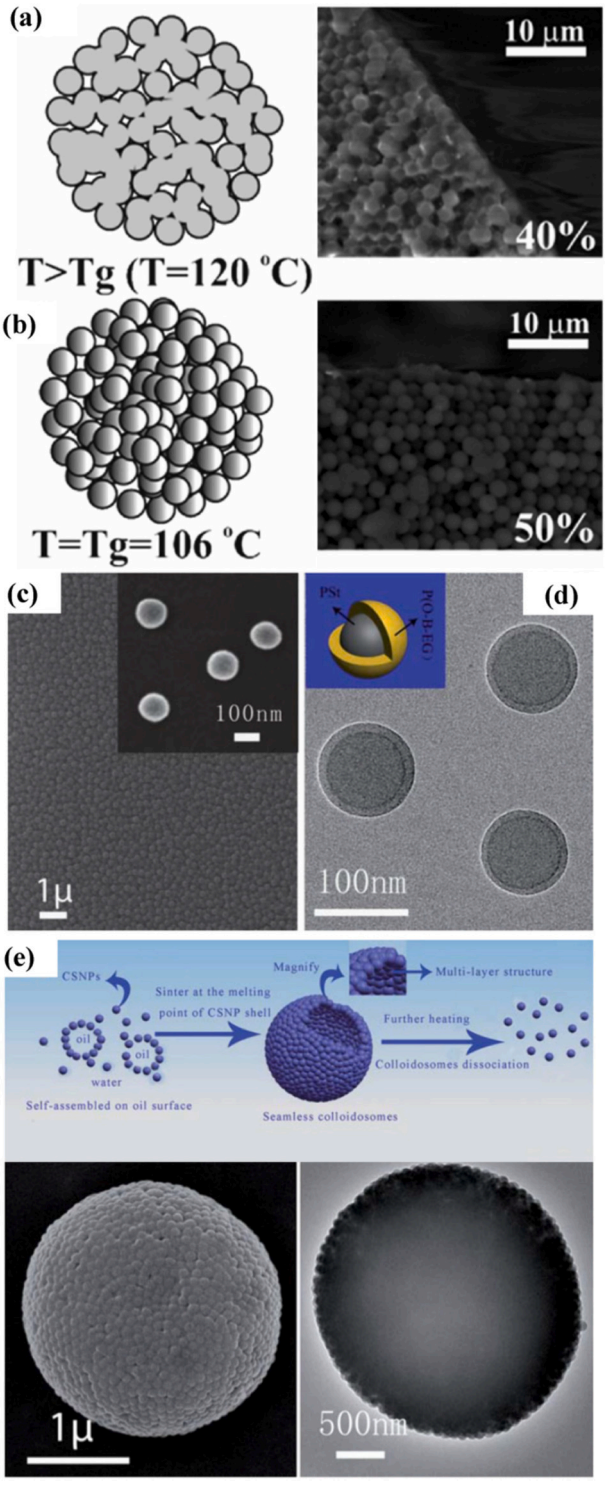

(caption on next column)

Fig. 23. - Applications of annealed colloidal particles: (a) illustration of the effect of temperature on the fusion of individual polystyrene latex particles inside a composite supra-particle: diagram of the fusion of latex particles annealed at $T > T_g$ and SEM image of a supra-particle made from a 40 wt% latex particle suspension annealed at 120 °C (reproduced from Ref. [182] with permission from the Royal Society of Chemistry; https://pubs.rsc.org/en/content/articlelanding/2016/sm/c6sm01651k); (b) diagram of a supra-particle annealed at the glass transition temperature (T_g) of polystyrene (106 °C) and SEM image of a fractured porous supra-particle made from 50 wt% particle suspension after annealing at T_g (reproduced from Ref. [182] with permission from the Royal Society of Chemistry; https://pubs.rsc.org/en/content/articlelanding/2016/sm/c6sm01651k); (c) SEM images of P(St-co-O–B-EG600) CSNPs; the inset is the a high resolution SEM image of P(St-co-O–B-EG600) CSNPs (reproduced from Ref. [183] with permission from the Royal Society of Chemistry; https://pubs.rsc.org/en/content/articlelanding/2011/sm/c0sm01128b); (d) SEM images of P(St-co-O–B-EG600) CSNPs; the inset is the model of the CSNPs (reproduced from Ref. [183] with permission from the Royal Society of Chemistry; https://pubs.rsc.org/en/content/articlelanding/2011/sm/c0sm01128b); (e) structure, formation and dissociation mechanism of seamless colloidosomes; SEM and TEM images of seamless colloidosomes built from P(St-co-O–B-EG600) CSNPs (reproduced from Ref. [183] with permission from the Royal Society of Chemistry; https://pubs.rsc.org/en/content/articlelanding/2011/sm/c0sm01128b).

interactions and van der Waals forces or to obviate the need to operate at temperatures higher than the boiling point of normal solvents when particles made up of materials with high sintering temperatures are used [183]. In fact, the proposed colloidosomes can reversibly lock together and dissociate by quenching and heating this system, respectively, and are bound so compactly that no interstice is present between the particles, allowing encapsulation and release of small molecular drugs [183]. In particular, the colloidosomes can dissociate into single nanoparticles and release the small target molecules encapsulated in the interior of the colloidosomes at a temperature higher than the melting point of the shell [183]. In addition, the dissociation temperature of colloidosomes can be controlled by simply adjusting the length of the PEG chains in the shell [183]. This type of colloidosome is dissociated into single core/shell particles when the system is heated up to 2 °C higher than the melting points of the CSNP shells; by varying the molecular weight of PEG in the amphiphilic shells of the CSNPs, a series of colloidosomes with different dissociation temperatures ranging from 43 to 56 °C could be obtained [183].

Sintered colloidal films can also serve as a starting point for further treatments. For example, in [178], sintering of 3D silica colloidal crystals was used before focused ion beam (FIB) structuring. In particular, 305 nm diameter silica colloidal particles were first calcined at 300, 450 and 550 °C for 12 h at each temperature; the use of calcination before self-assembly on quartz microscope slides and sintering at 900 °C for 12 h made colloidal crystals less prone to cracking; the sintered films were robust and derived their mechanical strength by virtue of the sintering-induced formation of nanoscale silica necks that connect them to their neighbouring spheres [178]. Focused ion beam milling was subsequently used to fabricate micron and submicron scale patterns in sintered silica colloidal crystal films [178].

Thermal annealing can also be exploited to get complex and anisotropic particle shapes starting from spherical particles. Anisotropic particles are of utmost interest both for their intrinsic physicochemical aspects and self-assembly behaviour and for practical applications due to their distinctive transport properties useful in detoxification, drug delivery and biosensing (if put in circulation in the human body), as well as in bioremediation and removal of contaminants from groundwater [184–191]. Converting spherical particles into anisotropic particles represents an interesting route for this purpose. Oblate and prolate ellipsoidal shapes as well as other anisotropic shapes have been obtained by high energy ion beam irradiation [9,27,29]. Anisotropic particle shaping can be achieved also by dry etching due to the presence of preferential etching directions [5,18,24–26]. However, these techniques

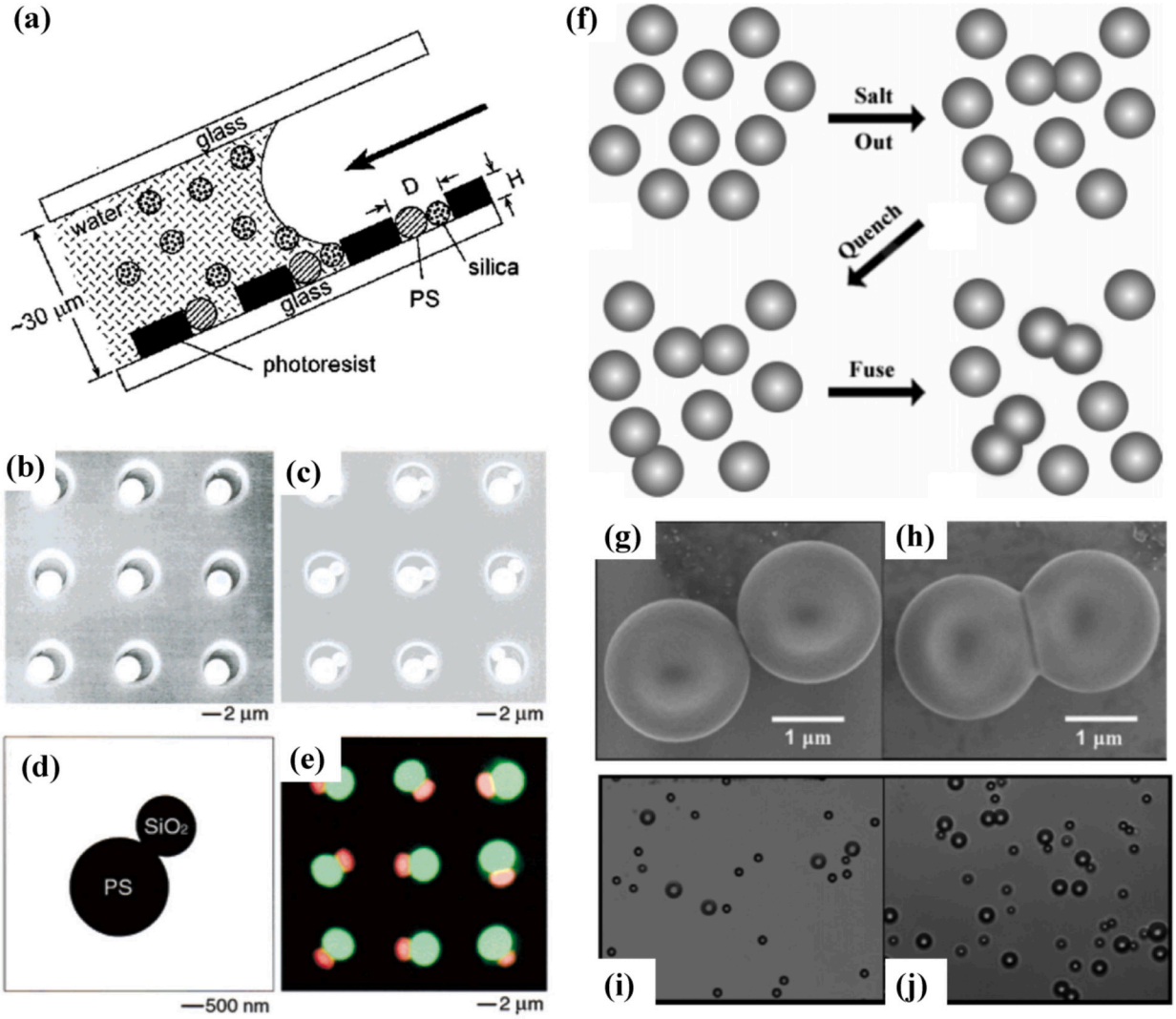

Fig. 24. - Applications of annealed colloidal particles: (a) sketch of the experimental procedure to generate dimers; the liquid was allowed to dewet from the surface along the direction indicated by the arrow (reprinted with permission from [192]. Copyright 2001 American Chemical Society); (b-c) SEM images showing the procedure used to assemble two different types of spherical colloids (2.8 μm polystyrene beads, 1.6 μm silica balls) into dimeric units under the physical confinement exerted by the cylindrical holes (5 and 2.5 μm in diameter and height, respectively) patterned in a thin film of photoresist (reprinted with permission from [192]. Copyright 2001 American Chemical Society); (d) TEM image of one of the dimers after release from the original support by dissolution of the photoresist pattern in ethanol, followed by redeposition onto a TEM grid (reprinted with permission from [192]. Copyright 2001 American Chemical Society); (e) fluorescence microscopy image of a 2D array of dimers from polystyrene of different size and colour: 3.0 μm beads doped with a green dye (FITC) and 1.7 μm beads doped with a red dye (Rhodamine); the green and red dye molecules were selectively excited and recombined into an overlapped image (reprinted with permission from [192]. Copyright 2001 American Chemical Society); (f) sketch of the salting out-quenching-fusing technique: starting from a suspension of singlet particles, a high ionic strength is introduced to start diffusion-limited aggregation due to van der Waals forces; afterwards, the ionic strength is quickly diluted after roughly the rapid flocculation time, which effectively quenches the aggregation reaction due to large electrostatic repulsive forces; heating above their glass transition temperature or chemical fusion is used to fuse the doublets together permanently (reprinted with permission from [193]. Copyright 2006 American Chemical Society); (g-h) field emission scanning electron microscope (FESEM) images of amidine homodoublets; the amidine particles making up the homodoublets are 2.1 μm in diameter: amidine homodoublet after the salting out-quenching steps (g); permanently fused amidine homodoublet particle after the full salting out-quenching-fusing process (h) (reprinted with permission from [193]. Copyright 2006 American Chemical Society); (i-j) carboxyl modified latex -sulfate heterodoublets; the sulfate particles are 2.4 μm in diameter, and the carboxyl modified latex particles are 4.6 μm in diameter: (i) singlet carboxyl modified latex and sulfate particles in deionized water (40×); (j) after the full salting out-quenching-fusing process; the heterodoublets break apart during sonication without the fusion step and remain stable during sonication (10 min) with the fusion step (reprinted with permission from [193]. Copyright 2006 American Chemical Society). (For interpretation of the references to colour in this figure legend, the reader is referred to the web version of this article.)

require complex and expensive equipment.

Thermal treatments can offer a cheaper route to anisotropic shaping. In section 5, we have already seen how thermal annealing of polymer particles on a polymer film can be exploited to get anisotropic particles such as peanut-like and rod-like structures [143] and prolate spheroidal particles [144].

In addition, thermal treatment in combination with specific template self-assembly techniques has also been exploited to generate asymmetric dimers from two types of monodispersed, spherical colloids that could be different in size, chemical composition, surface functionality, density or sign of surface charges, bulk properties or a combination of such characteristics [192]. In particular, a parallel cell composed of two glass substrates has been used, with the surface of the bottom substrate patterned with cylindrical holes of diameter D and height H [192] (Fig. 24(a)). When the colloidal suspension is allowed to dewet slowly across the cell, the capillary force exerted on the rear edge of this liquid

slug would drag the spherical colloids across the surface of the bottom substrate until they are physically trapped in the arrays of cylindrical holes [192]. If specific geometric constraints relating the characteristics of the patterned surface to the particle diameter d are satisfied (namely, if $0.5d \leq H \leq 1.37d$ and $d \leq D \leq 2d$), only one particle can get trapped in a hole, with a yield as high as 95% [192]. The procedure can be summarized as follows [192]:

- self-assembly of the first particle type (for instance, 2.8 μm PS particles trapped in cylindrical holes patterned in a photoresist film spin-coated on a glass substrate with $D = 5$ μm and $H = 2.5$ μm);
- permanent fixing of the position of the first particle type in each cylindrical hole by thermal treatment (for example, heating the sample to a temperature slightly higher than T_g of PS for a few seconds);
- self-assembly of a second particle type (for instance, 1.6 μm silica particles);
- permanent welding of the two particles together by thermal treatment (heating the sample to a temperature slightly higher than T_g of PS);

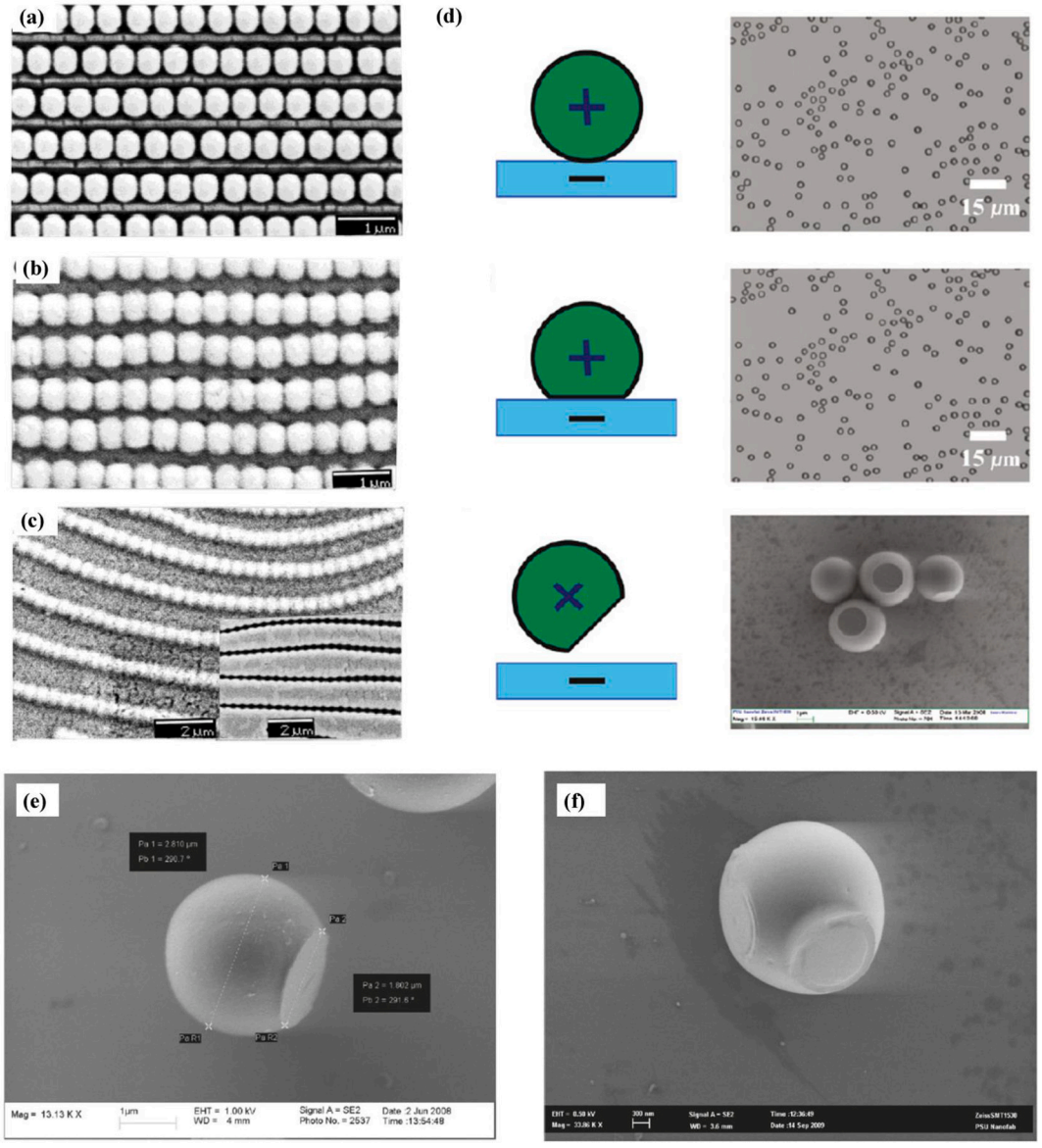

Fig. 25. - Applications of annealed colloidal particles: (a) 1D colloidal array on grooves (reprinted with permission from [194]. Copyright 2002 American Chemical Society); (b) 1D colloidal array on grooves after heating at 165 °C for 100 s (reprinted with permission from [194]. Copyright 2002 American Chemical Society); (c) 1D colloidal array on grooves after heating at 165 °C for 680 s; the inset image is the inverse pearl necklace (after extraction of PS particles) (reprinted with permission from [194]. Copyright 2002 American Chemical Society); (d) procedure to get polystyrene microspheres flattened in one spot and corresponding images of positively charged 3.3 μm amidine-functionalized PS particles in DI water that were electrostatically adhered to a negatively charged flat glass substrate (top), placed in a standard heat autoclave (120 °C, 18 psig) to flatten particles in one spot (center) and finally sonicated off the surface to obtain single flattened microsphere colloids in water (reprinted with permission from [194]. Copyright 2002 American Chemical Society); (e) SEM image of 3.3 μm amidine-functionalized PS particles settled in DI water and placed in the autoclave at 120 °C and 18 psig for 60 min (reprinted with permission from [195]. Copyright 2009 American Chemical Society); (f) SEM image of an amidine-functionalized polystyrene latex particle with two flattened sides; the particles were settled in DI water onto a nanofabricated v-groove template etched in a silicon wafer; subsequently, the sample was placed in an autoclave at 120 °C and 18 psig for 90 min (reprinted with permission from [195]. Copyright 2009 American Chemical Society).

- release of the particle dimers by removal of the cylindrical pattern (e.g. release into an aqueous dispersion by dissolving the photoresist pattern in ethanol under sonication).

In this way, not only a seamless bonding between a polymer and an inorganic particle can be obtained, but also other combinations (for example, particles of the same material but different size and doped with different fluorescent dyes, etc.) [192] (Fig. 24(b-e)).

Colloidal doublets have also been produced by a salting out/quenching/fusing technique. Both homodoublets (i.e. doublets consisting of two particles of the same type) and heterodoublets (i.e. particles of different type) have been produced in this way [193]. Fig. 24(f) illustrates a schematic of the process; it consists of the following steps [193]:

- a suspension of functionalized charged colloidal particles is placed in a test tube; a salt solution is added and is swirled to promote good mixing between particles and salt;
- particles aggregate quickly, thereby being salted out;
- after 60 s, the aggregation is quenched by adding deionized water to decrease the ionic strength;
- in order to prevent doublets from breaking apart (because particles remain stable in unperturbed solution, but severe agitation due, for example, to sonication, vortexing or high-speed centrifugation often causes the doublets to break apart), particles are heated above their glass transition temperature for 15 min, inducing the doublets to permanently fuse to each other by allowing the polymer chains of the touching particles in the doublet to diffuse together; an autoclave is used to heat, while avoiding boiling; simple heating in an oil bath or on a hot plate and not in a pressurized vessel results in the aqueous solution undergoing convective boiling, which then causes further uncontrolled aggregation; an oil bath with a small pressurized vessel enables better control of the temperature and time of heating (for example, placing solutions in an autoclave at 120 °C and 18 psi results in the PS homodoublets and heterodoublets becoming permanently fused into a doublet); as an alternative, doublets can be fused by the combination of addition of an organic solvent and heating; the solvent (e.g. toluene) causes the particles to swell slightly, thereby lowering their T_g such that the particles can be fused at a lower temperature where the solution is not boiling; for example a particle solution heated to 80 °C and containing only 5% toluene results in permanently fused colloidal homodoublets; after fusion, the solvent is removed from the particle suspension (e.g. removal of toluene via a N_2 purge).

This approach has been applied to the fabrication of homodoublets and heterodoublets starting from particles in the size range from 800 nm to 5.0 μm; PS and silica homodoublets and PS/silica heterodoublets have been produced [193] (Fig. 24(g-j)).

Specific particle shaping effects can be obtained by thermal treatments carried out on particles self-assembled onto pre-patterned substrates.

For instance, thermal treatment of 1D wires of colloidal particles has been investigated [194]. In particular, dense packings of PS particles were assembled on template samples consisting of 1D surface relief gratings obtained on a photopatterned epoxy-based azobenzene-functionalized polymer (AFP) matrix. The glass transition temperatures of PS particles and AFP were 98 and 110 °C, respectively [194]. The 1D colloidal array on the grooves was treated for 100, 680 and 1560 s at 165 °C, resulting in neck (contact area of beads), pearl necklace and wire formation, respectively [194] (Fig. 25(a-c)). The AFP matrix, which consists of grooves prior to heating, became smooth and level [194]. For treatments at 113 °C (close to T_g of the matrix) for 2 h, particles retained their shape and no neck was observed between them [194]. The findings show that neck formation, which is necessary for the wire pattern, is strongly dependent on the thermal states of the polymer chains of the particles and the matrix [194]:

- at a low thermal state, small chain mobility, the enlarged interface between PS particles and the PS-matrix interfacial tension led to failure of the elastic adhesion of the particles and, as a result, no neck was formed;
- when the thermal state was sufficiently high, the sintering process followed the viscous flow model due to active polymer chain mobility; experimental data for particle sintering were compared with Frenkel's model.

Applications have been envisaged in material patterning. For instance, by selective dissolution of the surface of the pearl necklace pattern by placing the sample in cyclohexane at 44 °C for 3 h, an inverse pearl necklace pattern can be obtained [194] (inset of Fig. 25(c)). Such patterning could be especially useful if particles are functionalized to show conducting properties [194].

Thermal treatments have also been harnessed to get colloidal flats, i.e. colloidal particles with a flat region, which can be useful for the fabrication of patchy particles in which the patch is chemically different from the rest of the particle [195]. For this purpose PS particles (amidine-functionalized, average diameter 3.3 μm) were used and went through the following steps [195] (Fig. 25(d-e)):

1. electrostatic adhesion to a flat surface;
2. heating of the sample above T_g of the polymer to allow particle deformation by spreading;
3. cooling of the particles below their T_g;
4. sonication to release spherical colloids with a flattened patch.

Being slightly above T_g, the particles deformed primarily because of surface tension, spreading onto the flat surface, whereas gravity plays a negligible role in the flattening because of the small size of the particles [195]. The radius s of the particle flat consistently increased with increasing time; a model was developed showing a dependence on time t of the type $s \sim t^{1/3}$, in disagreement with Frenkel's model [195]. Experimental data showed a good accordance with the developed theoretical model, except for short thermal treatments (below 15 min) and long treatments (above 6 h), where the graph shows a plateau, because s reaches about 90% of the original particle size [195]. By assembling particles on more complex pre-patterned substrates, particles with multiple flats can be obtained: for instance, by assembly on a v-shaped template in a silicon wafer, particles with two flats can be obtained [195] (Fig. 25(f)).

8. Conclusions

In this review, we have examined thermal treatments for polymer and silica particles, which represent the most widespread building blocks for colloidal assemblies. Heat is a powerful and cost-effective tool to achieve deformation of colloidal particles and colloidal masks. Except for the case of selective laser sintering, thermal treatments can be implemented with more straightforward and lower cost experimental set-ups in comparison to other techniques exploited for the modification of colloidal particles and assemblies, such as dry etching and ion beam irradiation.

For polymer particles, the key material parameter governing shaping upon thermal annealing is the glass transition temperature relative to the temperature of thermal treatment. For silica particles, surface and internal silanol groups play a major role in dehydration and dehydroxylation processes and determine the final shaping effects for variable temperature. Complex viscous and viscoelastic transport mechanisms intervene upon thermal treatment leading to necking and even coalescence between neighbouring particles.

Different parameters can be adjusted to control the specific shaping effects. These are related to both the thermal treatment (heating system, temperature and duration of the treatment) and the particles (size,

polydispersity, surface functionalization). Polymer particles allow one to get morphological changes at much lower temperatures than silica particles. In addition, as the glass transition temperature of polymers spans over a broad range depending on the specific polymer at hand (as it is related to its structure and crystallinity), this offers great versatility in engineering morphological changes, for instance by adjusting it via the composition of copolymer particles. Shaping can also be tailored by using core/shell particles or combining particles with different glass transition temperatures. The substrate on which particles are placed also plays a role. In particular, when polymer particles are assembled on a polymer substrate, both the particles and the substrate undergo deformation, with the possibility to get more complex shaping effects depending on the particle/substrate material combination. Finally, thermal treatments of particle monolayers can also be carried out at the air/water interface, thereby benefitting from the possibility to preserve the high order attainable via self-assembly at the air/water interface.

The ensuing deformation can be exploited for different applications. For example, the expansion and flattening of particles in thermally annealed closely-packed monolayers can be employed to tune the shape and size of the interstices between neighbouring particles, with consequent enrichment of the variety of geometric features that can be obtained when particles are used as a mask in colloidal lithography. In addition to this indirect application in nanostructuring, thermally treated particle assemblies can be directly exploited for their intrinsic physical properties. Thermal annealing can be harnessed to tune the spectral response of photonic crystals or to vary the thermal conductivity and mechanical stability of colloidal assemblies. Finally, it allows to synthesise particles of anisotropic shapes from spherical particles even of different materials, as is the case for homodoublets, heterodoublets, particles exhibiting a flat or peanut-like and rod-like structures. In addition, thermal annealing can improve the cohesion between individual particles in colloidosomes in comparison to mere electrostatic interactions and van der Waals forces.

It is noteworthy to observe that necking, sintering and coalescence have been observed also by other particle shaping techniques, such as dry etching [5,18–23,196], ion beam irradiation [9,27–31] and X-ray bombardment [197]. Although each technique exhibits peculiar features and shaping mechanisms and entails characteristic morphological variations, thermal treatment allows one to reach such shaping effects in a more cost effective way. While it is true that other specific shaping effects are not attainable via thermal treatments (e.g. particle size reduction or precise ellipsoidal shaping), it can represent a valid and powerful alternative to get necking and other morphologies, including complex and anisotropic ones such as doublets, peanuts and rods.

Other approaches, such as photolithography and two-photon polymerization, can be adopted for the fabrication of particles with anisotropic shapes [198,199]. Even if some specific intricate shapes (e.g. silica tori or handlebodies [198] and colloidal particles in the form of thin, rigid polymeric tubes shaped into knots of different chiralities [199]) may not be feasible by heat-based approaches, in the other cases thermal treatment represents a more attractive solution in comparison with such methods in terms of cost, yield and time burden and allows one to get anisotropic shaping on a large scale starting from widespread spherical colloidal particles (often commercially available) with simple and low cost equipment.

In addition, we point out that the theoretical background and experimental results and concepts such as necking and sintering here illustrated for spherical polymer and silica particles are important to understand similar phenomena occurring in other situations, for instance different material systems, such as microgels [200] or Pt, CeO_2, SnO_2 and TiO_2 [201], or other treatments.

In conclusion, we are confident that this comprehensive review of thermal treatment of colloidal particles may help the reader to get insight into this shaping technique, accurately understand its mechanisms and potential and envisage novel vistas and routes of particle shaping.

CRediT authorship contribution statement

Valeria Lotito: Conceptualization, Data curation, Formal analysis, Investigation, Methodology, Software, Validation, Visualization, Writing – original draft, Writing – review & editing. **Tomaso Zambelli:** Funding acquisition, Project administration, Resources, Writing – review & editing.

Declaration of competing interest

The authors declare that they have no known competing financial interests or personal relationships that could have appeared to influence the work reported in this paper.

Data availability

No data was used for the research described in the article.

Acknowledgements

This work was supported by the Swiss innovation promotion agency KTI-CTI (Contract 14336.1 PFNM).

Appendix A. More on glass transition temperature and melting temperature

According to their response to thermal treatments, polymers can be classified into different categories. A thermoplastic is a polymer that softens and can be made to flow if heated; upon cooling it hardens and retains the shape imposed at elevated temperature; this heating and cooling cycle can usually be repeated many times if the polymer is properly compounded with stabilizers [35]. Examples of thermoplastics are polystyrene, poly (vinyl chloride), polyethylene, poly(ethylene terephthalate) [35]. A thermosetting plastic is a polymer that can be made to undergo a chemical change to produce a network polymer, named a thermoset polymer; thermosetting polymers can often be shaped with the application of heat and pressure, but the number of such cycles is severely limited; an example of thermosetting polymers is given by epoxies [35]. A thermoset plastic is a solid polymer that cannot be dissolved or heated to sufficiently high temperatures to allow continuous deformation, because chemical decomposition intervenes at lower temperatures; an example is given by vulcanized rubber [35].

Both T_g and T_m are important [35]:

- T_g sets an upper temperature limit for the use of amorphous thermoplastics like polymethyl methacrylate (PMMA) or polystyrene and a lower temperature limit for rubbery behaviour of an elastomer like SBR (styrene-butadiene rubber) or 1,4-cis-polybutadiene;
- in case of semicrystalline thermoplastics, T_m or the onset of the melting range determines the upper operating temperature; semicrystalline polymers tend to be tough and leathery between T_g and T_m; brittleness begins to set in below T_g of the amorphous regions; as a rule of thumb, semicrystalline plastics are used at temperatures between T_g and a practical softening temperature lying above T_g and below T_m.

Different relationships and empirical correlations have been found out between T_g and T_m; typically, for most of symmetrical and asymmetrical polymers, the ratio between T_g and T_m is around 0.5–0.8 [38].

Fig. A1 shows the specific volume-temperature graph for a polymer which cools down from its molten state; the polymer can either crystallize (route a) or cool down to its glassy, amorphous state (route b); the temperature at which the slope changes (route b) corresponds to the glass transition temperature [38].

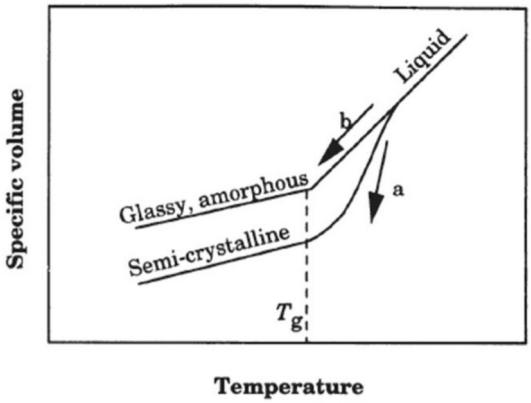

Fig. A1. - Fundamental properties of polymers: temperature-specific volume graph showing cooling of a liquid following routes a (crystallization) or b (forming a glassy amorphous structure) (reprinted by permission from Springer Nature: [38], Copyright 1999, reproduced with permission from SNCSC).

The concept of free volume plays a major role in distinguishing between crystalline, glassy amorphous polymer and rubbery amorphous polymer (Scheme 1). This concept has been introduced as an explanation for mobility by recalling the words used by the poet Lucretius to describe the thoughts of Epicurus on empty space or free volume, as “intangible space, voids, emptiness”, without which “things could not in any way move” [38]. In this way, one can assume the existence of two types of volume in matter, namely occupied volume and free volume; the latter allows the mobility of the atoms (segments) [38]. The free volume can be represented by mobile holes jumping around in the structure [38]. The fractional free volume is the ratio of the free volume to the total volume [38]. An ideal crystal consists only of occupied volume, a glassy, amorphous polymer ($T < T_g$) has only a small fraction of slowly moving holes, while an amorphous, rubbery polymer ($T > T_g$) exhibits a higher concentration of rapidly moving holes [38].

The mechanical properties of amorphous polymers undergo profound variations across the glass transition region, whereas those of semi-crystalline polymers are less pronounced in general, although still evident [35].

When a material is stressed, it can respond by deforming [35]:

- in a non-recoverable manner: rearrangements in the positions of whole molecules or segments of molecules result in the dissipation of the applied work as internal heat; this irreversible mechanism involves the flow of sections of macromolecules in the solid specimen;
- in an elastic manner: it is characteristic of glasses, whose components cannot flow past each other; such materials usually fracture in a brittle manner at small deformations, because the creation of new surfaces is the only way to release the strain energy stored in the solid (as is the case for window glasses).

At sufficiently low temperatures a polymer is a hard, brittle material with a modulus $>10^9$ N/m^2 [35]. In fact, in the glassy region the available thermal energy is insufficient to allow rotation about single bonds in the polymer backbone, thereby hampering movements of large-scale (about 50 consecutive chain atoms) segments of macromolecules [35]. The glass transition region is a temperature range over which the onset of motion on the scale of molecular displacements can be found in a polymer specimen [35]. In fact, as the temperature is raised, the thermal agitation becomes sufficient for segmental movement and the brittle glass begins to behave in a leathery fashion [35]. The modulus decreases by a factor of about 10^3 over a temperature range of about 10–20 °C in the glass-to-rubber transition region [35].

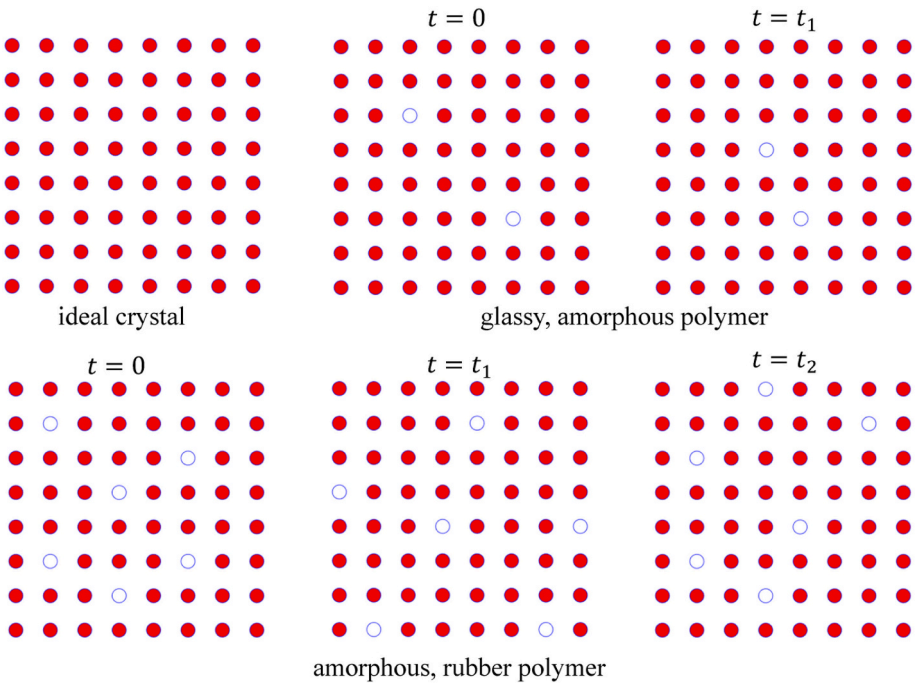

Scheme 1. – Sketch of the free volume concept; the occupied volume is indicated by filled red circles, free volume (hole) by empty circles; an ideal crystal consists only of occupied volume; a glassy, amorphous polymer ($T < T_g$) has only a small fraction of slowly moving holes, while an amorphous, rubbery polymer ($T > T_g$) exhibits a higher concentration of rapidly moving holes; snapshots are taken at different times (t) (redrawn and adapted from [38]).

The rubbery region is characterized by a short-term elastic response to the application and removal of a stress [35]. Polymer molecules respond to the gross deformation of the specimen by changing to more extended conformations; they do not flow past each other to a significant extent, due to the fact that their rate of translation is restricted by mutual entanglements; a single entangled molecule has to drag along its attached neighbours or slip out of its entanglement in order to flow; the amount of slippage increases with the duration of the applied stress [35]. In addition, molecular flexibility and mobility increase with temperature and continued warming of the sample causes the scale of molecular motions to increase in the time scale of the experiment [35]. The sample will flow in a rubbery manner [35]. When the stress is released, the specimen will not contract completely back to its initial dimensions [35]. With higher testing temperatures, the flow rate and the amount of observed permanent deformation will continue to increase [35].

Appendix B. Factors affecting characteristic temperatures

As anticipated in section 2.1.2, T_g is affected by the following factors:

- polymer structure: as the glass-to-rubber transition reflects the onset of movements of fairly large segments of the polymer backbone, T_g is influenced by the flexibility of the macromolecules and by the intensities of intermolecular forces [35], in particular:

1. aromatic or aliphatic polymers [35]: chain backbones with bonds such as those of Scheme 2 tend to be flexible and exhibit low T_g; insertion of an aromatic ring in the main chain entails an increase in T_g (this aspect plays a major role in the application of amorphous glassy polymers like poly (phenylene oxide) and polycarbonate);
2. presence of substituents [35]: bulky, inflexible substituents on chain carbons generally hinder rotations about single bonds in the main chain and raise T_g (for this reason, T_g of polypropylene and poly (methyl methacrylate) are respectively higher than T_g of polyethylene and poly (methyl acrylate)); nonetheless, the size of the substituent does not exert alone an impact on T_g; a flexible side group (e.g. an alkyl chain) lowers T_g; larger substituents prevent efficient packing of macromolecules in the absence of crystallization, but motion of the polymer chain is freed only if the substituent itself can change its conformation readily;
3. intermolecular forces [35]: stronger intermolecular attractive forces pull the chains together and impede relative motions of segments of different macromolecules; for this reason, polar polymers and those in which hydrogen bonding or other specific interactions are significant have high T_g (e. g. polyacrylonitrile>poly(vinylalcohol) > poly(vinylacetate) > polypropylene);
4. molecular weight [35]: for a given polymer type, T_g increases with number average molecular weight $\overline{M_n}$ according to:

$$T_g = T_g^{\infty} - \frac{u}{\overline{M_n}} \tag{B1}$$

where T_g^{∞} is the glass-to-rubber transition temperature of an infinitely long polymer chain and u is a constant dependent on polymer; for example T_g is 88 °C for polystyrene with $\overline{M_n} > 10000$ and 100 °C for polystyrene with $\overline{M_n} > 50000$. Other relationships describing the dependence of T_g on $\overline{M_n}$ have also been found [39–41];

5. cross-linking [35]: material cohesiveness in amorphous glassy polymers, like polystyrene, stems mainly from entanglements between macromolecules; in case of cross-linking of the macromolecules instead of just entanglement, the intermolecular linkages do not slip and the rubbery plateau region persists until the temperature is high enough to induce chemical degradation of the macromolecules. Cross-linking increases the glass transition temperature of a polymer when the average size of the segments between cross-links is equal or lower than the lengths of the main chain that can start to move at temperatures near T_g. The glass transition temperature exhibits minor variation with the degree of cross-linking when the cross-links are widely spaced (e.g. in normal vulcanized rubber). Nonetheless, in case of polymers that are already highly cross-linked (as in the "cure" of epoxy and phenolic thermosetting resins), large shifts of T_g with increased cross-linking are observed. Different polymers have been investigated and empirical relationships describing the dependence of T_g on cross-linking have also been derived [42–45];
6. crystallinity: amorphous thermoplastics undergo major, typically step-like changes of properties in the glass transition range; in semi-crystalline thermoplastics, such variations are less pronounced (because of the presence of an as yet unmelted crystalline phase) and depend on the crystallinity, i.e. the proportion of crystalline phase [36]. In a solid semi-crystalline polymer, large-scale segmental motion occurs only at temperatures between T_g and T_m and only in amorphous regions; at low degrees of crystallinity the crystallites act as virtual cross-links and the amorphous regions exhibit rubbery or glassy behaviour, according to the temperature and time scale of the experiment [35];
7. miscible polymer mixtures: T_g of miscible polymer mixtures of two components can be computed as [35]:

$$\frac{1}{T_g} \cong \frac{w_A}{T_{gA}} + \frac{w_B}{T_{gB}} \tag{B2}$$

where T_{gA} and T_{gB} are the glass transition temperatures of the two components and w_A and w_B are the weight fractions of the two components. The relationship can be generalized to the Fox equation for n components [38]:

$$\frac{1}{T_g} = \sum_{i=1}^{n} \frac{w_i}{T_{gi}} \tag{B3}$$

where T_{gi} and w_i represent the glass transition temperature and the mass fraction of component i. These equations are useful with plasticizers which are materials that enhance the flexibility of the polymer with which they are mixed: in fact, the incorporation of plasticizers also affects T_g and the mechanical behaviour of polymers, in particular by reducing T_g and making the polymer more flexible at any temperature above T_g [35]. For instance, T_g of poly(vinyl chloride) can be lowered from about 85 °C for unplasticized material to −30 °C for blends of the polymer with 50 wt% of dioctylphthalate plasticizer [35]. The previous equations cannot be applied to polymer blends in which the components are not mutually soluble [35]. The previous equations are also a useful to estimate the glass transition temperatures of statistical copolymers (in this case the subscripts A and B refer to the homopolymers) [35]. However, it cannot be applied to block and graft copolymers in which a separate T_g is observed for each component polymer if the blocks or branches are long enough to allow each homopolymer type to segregate into its own region [35]. We observe that alternative expressions are available for the glass transition temperature of polymer blends, for instance [38]:

$$\frac{\ln T_g}{T_g} = \sum_{i=1}^{n} \frac{w_i \ln T_{gi}}{T_{gi}} \tag{B4}$$

- pressure [38]: T_g depends on the hydrostatic pressure p according to the following equation:

$$\frac{dT_g}{dp} = \frac{\Delta\beta}{\Delta\alpha} \tag{B5}$$

where $\Delta\beta$ and $\Delta\alpha$ represent the variation in compressibility and volume expansion coefficient associated with the glass transition, respectively; typical values of this ratio for polymers are in the range of 0.2–0.4 K MPa^{-1};

- presence of additives, solvent residues, moisture, etc., which can lower T_g [34].

Scheme 2. – Examples of chain backbones.

References

[1] Lotito V, Zambelli T. Approaches to self-assembly of colloidal monolayers: a guide for nanotechnologists. Adv Colloid Interface Sci 2017;246:217.
[2] Xia Y, Gates B, Yin Y, Lu Y. Monodispersed colloidal spheres: old materials with new applications. Adv Mater 2000;12(10):693–713.
[3] Zhang J, Sun Z, Yang B. Self-assembly of photonic crystals from polymer colloids. Curr Opin Colloid Interface Sci 2009;14(2):103.
[4] Galisteo-Lopez JF, Ibisate M, Sapienza R, Froufe-Perez LS, Blanco A, Lopez C. Self-assembled photonic structures. Adv Mater 2011;23(1):30.
[5] Lotito V, Zambelli T. Self-assembly and nanosphere lithography for large-area plasmonic patterns on graphene. Adv Colloid Interface Sci 2015;447:202.
[6] Vogel N, Weiss CK, Landfester K. From soft to hard: the generation of functional and complex colloidal monolayers for nanolithography. Soft Matter 2012;8:4044.
[7] Cortés E, Wendisch FJ, Sortino L, Mancini A, Ezendam S, Saris S. de S Menezes L, Tittl a, Ren H, Maier SA, optical metasurfaces for energy conversion. Chem Rev 2022;122(19):15082.
[8] Huang Y, Yang R, Xiao T, Li H, Tian M, Xie Z, et al. Wafer-scale self-assembled 2.5D metasurface for efficient near-field and far-field electromagnetic manipulation. Appl Surf Sci 2022;601:154244.

[9] Lotito V, Karlušić M, Jakšić M, Tomić Luketić K, Müller U, Zambelli T, et al. Shape deformation in ion beam irradiated colloidal monolayers: an AFM investigation. Nanomaterials 2020;10(3):453.
[10] Lotito V, Zambelli T. Pattern formation in binary colloidal assemblies: hidden symmetries in a kaleidoscope of structures. Langmuir 2018;34(26):7827.
[11] Lotito V, Zambelli T. A journey through the landscapes of small particles in binary colloidal assemblies: unveiling structural transitions from isolated particles to clusters upon variation in composition. Nanomaterials 2019;9(7):921.
[12] López-Godoy S, Díaz-Leyva P, Kozina A. Self-assembly in binary mixtures of spherical colloids. Adv Colloid Interface Sci 2022;308:102748.
[13] Ickler M, Menath J, Holstein L, Rey M, Buzza DMA, Vogel N. Interfacial self-assembly of SiO_2-PNIPAM core-shell particles with varied crosslinking density. Soft Matter 2022;18(30):5585.
[14] Lotito V, Zambelli T. Self-assembly of single-sized and binary colloidal particles at air/water interface by surface confinement and water discharge. Langmuir 2016;32(37):9582.
[15] Keller AW, Marino E, An D, Neuhaus SJ, Elbert KC, Murray CB, et al. Sub-5 nm anisotropic pattern transfer via colloidal lithography of a self-assembled GdF_3 nanocrystal monolayer. Nano Lett 2022;22(5):1992.
[16] Qian L-X, Li W, Gu Z, Tian J, Huang X, Lai PT, et al. Ultra-sensitive β-Ga_2O_3 solar-blind photodetector with high-density Al@$Al2O_3$ core-shell nanoplasmonic array. Adv Optical Mater 2022;10(12):2102055.
[17] Li X, Chen L, Ma Y, Weng D, Li Z, Song L, et al. Ultrafast fabrication of large-area colloidal crystal micropatterns via self-assembly and transfer printing. Adv Funct Mater 2022;32(45):2205462.
[18] Lotito V, Zambelli T. Playing with sizes and shapes of colloidal particles via dry etching methods. Adv Colloid Interface Sci 2022;299:102538.
[19] Jeong J-R, Kim S, Kim S-H, Bland JAC, Shin S-C, Yang S-M. Fabrication of hexagonal lattice co/Pd multilayer nanodot arrays using colloidal lithography. Small 2007;3(9):1529.
[20] Venugopalan PL, Gupta G, Chosh A, Singh HJ, Nair G, Ghosh A. Study of the formation of nano-networks in colloidal particles. Int J Polym Mater Po 2013;62:499.
[21] Gogel D, Weinl M, Lindner JKN, Stritzker B. Plasma modification of nanosphere lithography masks made of polystyrene beads. J Optoelectron Adv M 2010;12(3):740.
[22] Sparnacci K, Antonioli D, Deregibus S, Panzarasa G, Laus M, De Leo N, et al. Two-dimensional non-close-packed arrays of nanoparticles via core-shell nanospheres and reactive ion etching. Polym Adv Technol 2012;23:558.
[23] Wendisch FJ, Oberreiter R, Salihovic M, Elsesser MS, Bourret GR. Confined etching within 2D and 3D colloidal crystals for tunable nanostructured templates: local environment matters. ACS Appl Mater Interfaces 2017;9:3931.
[24] Tan BJY, Sow C-H, Lim K-Y, Cheong F-C, Chong G-L, Wee AT-S, et al. Fabrication of a two-dimensional periodic non-close-packed array of polystyrene particles. J Phys Chem B 2004;108:18575.
[25] Ngamaroonchote A, Muangnapoh T, Aroonyadet N, Kumnorkaew P, Laocharoensuk R. Plasma-etched nanosphere conductivity-inverted lithography (PENCIL): a facile fabrication of size-tunable gold disc array on ITO-coated glass. Adv Mater Interfaces 2018;5:1800477.
[26] Akinoglu EM, Morfa AJ, Giersig M. Understanding anisotropic plasma etching of two-dimensional polystyrene opals for advanced materials fabrication. Langmuir 2014;30:12354.
[27] Lotito V, Zambelli T. Manipulating the morphology of colloidal particles via ion beam irradiation: a route to anisotropic shaping. Adv Colloid Interface Sci 2022;304:102642.
[28] Kraus D, Lindner JKN, Stritzker B. Ion beam induced sintering of colloidal polystyrene nano-masks. Nucl Instrum Methods Phys Res, Sect B 2007;257:455.
[29] van Dillen T, van Blaaderen A, Polman A. Shaping colloidal assemblies. Mater Today 2004;7(7–8):40.
[30] Zolnai Z, Deák A, Nagy N, Tóth AL, Kótai E, Battistig G. A 3D-RBS study of irradiation-induced deformation and masking properties of ordered colloidal nanoparticulate masks. Nucl Instrum Methods Phys Res, Sect B 2010;268:79.
[31] Lindner JKN, Gehl B, Stritzker B. Shape modifications of self-organised colloidal silica nanomasks on silicon. Nucl Instrum Methods Phys Res, Sect B 2006;242:167.
[32] Merkel DG, Hegedus G, Gracheva M, Deák A, Illés L, Németh A, et al. A three-dimensional analysis of magnetic nanopattern formation in FeRh thin films on MgO substrates: implications for spintronic devices. ACS Appl Nano Mater 2022;5(4):5516.
[33] Dawi EA, Mustafa E, Siahaan T. Anisotropic deformation of colloidal particles under 4 MeV cu ions irradiation. Mater Res Exp 2022;9(8):086506.
[34] Pacáková V, Virt J. Plastics. In: Worsfold P, Townshend A, Poole C, editors. Encyclopedia of analytical science (second edition) reference module in chemistry, Molecular Sciences and Chemical Engineering. 7; 2005. p. 180–6.
[35] Rudin A, Choi P. The elements of polymer science and engineering. 3rd ed. Elsevier; 2013.
[36] Ehrenstein GW, Riedel G, Trawiel P. Thermal analysis of plastics. Theory and practice. Carl Hanser Verlag; 2004.
[37] Angell CA, Sivarajan S. Glass transition. Encyclopedia of Materials: Science and Technology 2001;4:3565.
[38] Gedde UW. Polymer physics. Springer; 1999.
[39] Hitachi Application brief. DSC measurements of polystyrene – the effects of molecular weight on glass transition. TA No 68 Aug. 1995.
[40] Claudy P, Létoffé JM, Camberlain Y, Pascault JP. Glass transition of polystyrene versus molecular weight. Polym Bull 1983;9:208.
[41] Rieger J. The glass transition temperature of polystyrene, Results of a round robin test. J Thermal Anal 1996;46:965.
[42] Glans JH, Turner DT. Glass transition elevation of polystyrene by crosslinks. Polymer 1981;22:1540.
[43] Ueberreiter K, Kanig G. Second-order transitions and mesh distribution functions of cross-linked polystyrenes. J Chem Phys 1950;18(4):399.
[44] Mason P. Thermal expansion and viscoelasticity of rubber in relation to crosslinking and molecular packing. Polymer 1964;5:625.
[45] Loshaek S. Crosslinked polymers, II. Glass temperatures of copolymers of methyl methacrylate and glycol dimethacrylates. J Polym Sci A 1955;15:391.
[46] Zhuravlev LT. The surface chemistry of amorphous silica. Zhuravlev model. Colloids and Surfaces A 2000;173:1.
[47] Bergna HE. In Bergna HE (editor) the colloid chemistry of silica. American Chemical Society; 1994.
[48] Bergna HE, In Bergna HE, Roberts WO, editors. Colloidal silica. Fundamentals and applications. CRC Press Taylor & Francis Group; 2005.
[49] Zhuravlev LT, Potapov VV. Density of silanol groups on the surface of silica precipitated from a hydrothermal solution. Russian Journal of Physical Chemistry 2006;80(7):1119.
[50] Di Vona ML. Annealing of polymer membranes. In: Drioli E, Giorno L, editors. Encyclopedia of membranes. Springer-Verlag; 2014.
[51] Harel E, Meltzer SE, Requicha AAG, Thompson ME, Koel BE. Fabrication of polystyrene latex nanostructures by nanomanipulation and thermal processing. Nano Lett 2005;5(12):2624.
[52] Perez-de-Eulate NG, Di Lisio V, Cangialosi D. Glass transition and molecular dynamics in polystyrene nanospheres by fast scanning calorimetry. ACS Macro Lett 2017;6:859.
[53] Yang Z, Fujii Y, Lee FK, Lam C-H, Tsui OKC. Glass transition dynamics and surface layer mobility in unentangled polystyrene films. Science 2010;328:1676.
[54] Bachelany M, Maeder X, Riesterer J, Hankache J, Lerose D, Christiansen S, et al. Synthesis mechanisms of organized gold nanoparticles: influence of annealing temperature and atmosphere. Cryst Growth Des 2010;10(2):587.
[55] Shi Y, Yan C, Zhou Y, Wu J, Wang Y, Yu S, et al. Materials for additive manufacturing. Academic Press-Elsevier; 2021.
[56] Nutz FA, Retsch M. Interfacial and volumetric sensitivity of the dry sintering process of polymer colloidal crystals: a thermal transport and photonic bandgap study. Phys Chem Chem Phys 2017;19:16124.
[57] Routh AF, Russel WB. Deformation mechanisms during latex film formation: experimental evidence. Ind Eng Chem Res 2001;40:4302.
[58] Pekcan Ö, Arda E, Bulmus V, Piskin E. Photon transmission method for studying film formation from polstyrene latexes with different molecular weights. J Appl Polym Sci 2000;77:866.
[59] Chen X, Fischer S, Yi Z, Boyko V, Terrenoire A, Reinhold F, et al. Structural reorganization of a polymeric latex film during dry sintering at elevated temperatures. Langmuir 2011;27:8458.
[60] Nawaz Q, Rharbi Y. Various modes of void closure during dry sintering of close-packed nanoparticles. Langmuir 2010;26(2):1226.
[61] Gonzalez E, Tollan C, Chuvilin A, Barandiaran MJ, Paulis M. Determination of the coalescence temperature of latexes by environmental scanning electron microscopy. ACS Appl Mater Interfaces 2012;4:4276.
[62] Arda E, Pekcan Ö. Time and temperature dependence of void closure, healing and interdiffusion during latex film formation. Polymer 2001;42:7419.
[63] Arda E, Özer F, Piskin E, Pekcan Ö. Film formation from nanosized copolymeric latex particles: a photon transmission study. J Colloid Interface Sci 2001;233(2):271.
[64] Singh PK, Pacholski ML, Gu J, Go YK, Singhal G, Leal C, et al. Designing multicomponent polymer colloids for self-stratifying films. Langmuir 2022;38(37):11160.
[65] Pekcan Ö, Winnik MA, Croucher MD. Fluorescence studies of coalescence and film formation in poly(methyl methacrylate) nonaqueous dispersion particles. Macromolecules 1990;23:2673.
[66] Uğur Ş, Elaissari A, Pekcan Ö. Void closure and interdiffusion processes during latex film formation from surfactant-free polystyrene particles: a fluorescence study. J Colloid Interface Sci 2003;263:674.
[67] Uğur Ş, Pekcan Ö. Time evolution of film formation from polystyrene particles: a percolation approach. Colloid Polym Sci 2005;284(3):309.
[68] Canpolat M, Pekcan Ö. Healing and photon diffusion during sintering of high-T latex particles. J Polym Science Pol Phys 1996;34:691.
[69] Arda E, Bulmus V, Piskin E, Pekcan Ö. Molecular weight effect on latex film formation from polystyrene particles: a photon transmission study. J Colloid Interface Sci 1999;213:160.
[70] Kim KD, Sperling LH, Klein A, Wignall GD. Characterization of film formation from direct mini-emulsified polystyrene latex particles via SANS. Macromolecules 1993;26:4624.
[71] Kim KD, Sperling LH, Klein A, Hammouda B. Reptation time, temperature, and cosurfactant effects on the molecular interdiffusion rate during polystyrene latex film formation. Macromolecules 1994;27:6841.
[72] Hu S, Rieger G, Yi Z, Zhang J, Chen X, Roth SV, et al. Structural evolution of a colloidal crystal fiber during heating and annealing studied by in situ synchrotron small angle X-ray scattering. Langmuir 2010;26(16):13216.
[73] Hu S, Rieger J, Roth SV, Gehrke R, Leyrer Men Y. GIUSAXS and AFM studies on surface reconstruction of latex thin films during thermal treatment. Langmuir 2009;25:4230.
[74] Qu X, Shi Y, Tang Y, Chen L, Jin X. Novel sintering behavior of polystyrene nanolatex particles in the filming process. J Colloid Interface Sci 2002;250:484.

[75] Wang Y, Zhao C-L, Winnik MA. Molecular diffusion and latex film formation: An analysis of direct nonradiative energy transfer experiments. J Chem Phys 1991; 95:2143.
[76] Asgarpour M, Bakir F, Khelladi S, Khavandi A, Tcharkhtchi A. Characterization and modeling of sintering of polymer particles. J Appl Polym Sci 2011;119(5): 2784.
[77] Rosenzweig N, Narkis M. Dimensional variations of two spherical polymeric particles during sintering. Polym Eng Sci 1981;21(10):582.
[78] Rosenzweig N, Narkis M. Observation and analysis technique for studying sintering of polymeric particles. J Appl Polym Sci 1981;26:2787.
[79] Rosenzweig N, Narkis M. Coalescence phenomenology of spherical polymer particles by sintering. Polymer 1980;21:988.
[80] Rosenzweig N, Narkis M. Sintering rheology of amorphous polymers. Polym Eng Sci 1981;21(17):1167.
[81] Kuczynski GC, Neuville B, Toner HP. Study of sintering of poly(methyl methacrylate). J Appl Polym Sci 1970;14:2069.
[82] Rosenzweig N, Narkis M. Newtonian sintering simulator of two spherical particles. Polym Eng Sci 1983;23(1):32.
[83] Truss RW, Han KS, Wallace JF, Geil PH. Cold compaction molding and sintering of ultra high molecular weight polyethylene. Polym Eng Sci 1980;20(11):747.
[84] Thümmler F, Thomma W. The sintering process. Metall Rev 1967;12(1):69.
[85] Kuczynski GC. Study of the sintering of glass. J Appl Phys 1949;20:1160.
[86] Narkis M. Sintering behavior of poly(methyl methacrylate) particles. Polym Eng Sci 1979;19(13):889.
[87] Bellehumeur CT, Bisaria MK, Vlachopoulos J. An experimental study and model assessment of polymer sintering. Polym Eng Sci 1996;36(17):2198.
[88] Mazur S, Plazek DJ. Viscoelastic effects in the coalescence of polymer particles. Prog Org Coat 1994;24:225.
[89] Lontz JF, Bonis LJ, Hausner HH. Fundamental phenomena in the material sciences. In: Sintering and plastic deformation. Proceedings of the first symposium on fundamental phenomena in the material sciences. Volume 1. Springer Science+Business Media; 2013. p. 25.
[90] Siegmann A, Raiter I, Narkis M, Eyerer P. Effect of powder particle morphology on the sintering behaviour of polymers. J Mater Sci 1986;21:1180.
[91] Hornsby PR, Maxwell AS. Mechanism of sintering between polypropylene beads. J Mater Sci 1992;27:2525.
[92] Pokluda O, Bellehumeur CT, Vlachopoulos J. Modification of Frenkel's model for sintering. AIChE J 1997;43(12):3253.
[93] Fuchs R, Weinhart T, Ye M, Luding S, Butt H-J, Kappl M. Initial stage sintering of polymer particles – experiments and modelling of size-, temperature- and time-dependent contacts. EPJ Web Conf 2017;140:13012.
[94] Hooper R, Macosko CW, Derby JJ. Assessing a flow-based finite element model for the sintering of viscoelastic particles. Chem Eng Sci 2000;55:5733.
[95] Balemans C, Hulsen MA, Anderson PD. Sintering of two viscoelastic particles: a computational approach. Appl Sci 2017;7:516.
[96] Balemans C, Hulsen MA, Anderson PD. Temperature-dependent sintering of two viscous particles. Addit Manuf 2018;24:528.
[97] Balemans C, Hejmady P, Cardinaels R, Anderson PD. Towards unraveling the sintering process of two polystyrene particles by numerical simulations. Korea-Australia Rheology J 2019;31(4):285.
[98] Aid S, Eddhahak A, Ortega Z, Froelich D, Tcharkhtchi A. Predictive coalescence modeling of particles from different polymers: application to PVDF and PMMA pair. J Mater Sci 2017;52:11725.
[99] Scribben E, Baird D, Wapperom P. The role of transient rheology in polymeric sintering. Rheol Acta 2006;45:825.
[100] Alvarez JE, Snijder H, Vaneker T, Cheng H, Luding S, Weinhart T. Neck growth kinetics during polymer sintering for powder-based processes. EPJ Web of Conferences 2021;249:05001.
[101] Jagota A, Argento C, Mazur S. Growth of adhesive contacts for Maxwell viscoelastic spheres. J Appl Phys 1998;83(1):250.
[102] Bellehumeur CT, Kontopoulou M, Vlachopoulos J. The role of viscoelasticity in polymer sintering. Rheol Acta 1998;37:270.
[103] German RM, Munir ZA. Morphology relations during bulk-transport sintering. Metall Trans A 1975;6A:2229.
[104] German RM, Munir ZA. Morphology relations during surface-transport controlled sintering. Metall Trans A 1975;6B:289.
[105] Lin YY, Hui CY, Jagota A. The role of viscoelastic adhesive contact in the sintering of polymeric particles. J Colloid Interface Sci 2001;237:267.
[106] Muller J-D, Bousmina M, Maazouz A. 2D-sintering kinetics of two model fluids as drops. Macromolecules 2008;41:2096.
[107] Polychronopoulos ND, Benos LT, Stergiou CI, Sarris IE, Vlachopoulos J. Viscous coalescence of unequally sized spherical and cylindrical doublets. Soft Matter 2022;18:4017.
[108] Berretta S, Wag Y, Davies R, Ghita OR. Polymer viscosity, particle coalescence and mechanical performance in high-temperature laser sintering. J Mater Sci 2016;51:4778.
[109] Mazur S, Beckerbauer R, Buckholz J. Particle size limits for sintering polymer colloids without viscous flow. Langmuir 1997;13(16):4287.
[110] Teteris G, Briedis I. A contribution to the sintering model of viscoelastic liquid drops with solid kernels. Mech Compos Mater 1997;33(4):397.
[111] Dillon RE, Matheson LA, Bradford EB. Sintering of synthetic latex particles. J Colloid Sci 1951;6(2):108.
[112] Polychronopoulos ND, Vlachopoulos J. The role of heating and cooling in viscous sintering of pairs of spheres and pairs of cylinders. Rapid Prototyping J 2020;26 (4):719.
[113] Routh AF, Russel WB. A process model for latex film formation: limiting regimes for individual driving forces. Langmuir 1999;15(22):7762.
[114] Popat A, Hartono SB, Stahr F, Liu J, Qiao SZ, Lu GQ(M). Mesoporous silica nanoparticles for bioadsorption, enzyme immobilisation, and delivery carriers. Nanoscale 2011;3:2801.
[115] Tang F, Li L, Chen D. Mesoporous silica nanoparticles: synthesis, biocompatibility and drug delivery. Adv Mater 2012;24:1504.
[116] Wu S-H, Mou C-Y, Lin H-P. Synthesis of mesoporous silica nanoparticles. Chem Soc Rev 2013;42:3862.
[117] Rosenholm JM, Sahlgren C, Lindén M. Towards multifunctional, targeted drug delivery systems using mesoporous silica nanoparticles – opportunities & challenges. Nanoscale 2010;2:1870.
[118] Slowing II, Vivero-Escoto JL, Wu C-W, Lin VS-Y. Mesoporous silica nanoparticles as controlled release drug delivery and gene transfection carriers. Adv Drug Deliv Rev 2008;60:1278.
[119] Silencieux F, Bouchoucha M, Mercier O, Turgeon S, Chevallier P, Kleitz F, et al. Mesoporous silica nanoparticles under sintering conditions: a quantitative study. Langmuir 2015;31:13011.
[120] Cho W, Saxena R, Rodriguez O, Achanta R, Plawsky JL, Gill WN. Effects of sintering on dielectric constants of mesoporous silica. J Non Cryst Solids 2004; 350:336.
[121] Newby JJ, Legg MA, Rogers B, Wirth MJ. Annealing of silica to reduce the concentration of isolated silanols and peak tailing in reverse phase liquid chromatography. J Chromatogr A 2011;1218:5131.
[122] Kandulski W. Shadow nanosphere lithography. PhD thesis. University of Bonn; 2007.
[123] Herzog G, Kashem MMA, Benecke G, Buffet A, Gehrke R, Perlich J, et al. Influence of nanoparticle surface functionalization on the thermal stability of colloidal polystyrene films. Langmuir 2012;28:8230.
[124] Kosiorek A, Kandulski W, Glaczynska H, Giersig M. Fabrication of nanoscale rings, dots, and rods by combining shadow nanosphere lithography and annealed polystyrene nanosphere masks. Small 2005;1(4):439.
[125] Zeng H, Xu X, Bando Y, Gautam UK, Zhai T, Fang X, et al. Template deformation-tailored ZnO nanorod/nanowire arrays: full growth control and optimization of field-emission. Adv Funct Mater 2009;19:3165.
[126] Mikhnev LV, Bondarenko EA, Chapura OM, Skomorokhov AA, Kravtsov AA. Influence of annealing temperature on optical properties of the photonic-crystal structures obtained by self-organization of colloidal microspheres of polystyrene and silica. Opt Mater 2018;75. 453e458.
[127] Sivadas BO, Ashcroft I, Khlobystov AN, Goodridge RD. Laser sintering of polymer nanocomposites. Adv Ind Eng Polym Res 2021;4:277.
[128] Hejmady P, van Breemen LCA, Anderson PD, Cardinaels R. Laser sintering of polymer particle pairs studied by *in situ* visualization. Soft Matter 2019;15:1373.
[129] Hejmady P, Cleven LC, van Breemen LCA, Anderson PD, Cardinaels R. A novel experimental setup for *in situ* optical and X-ray imaging of laser sintering of polymer particles. Rev Sci Instrum 2019;90(8):083905.
[130] Hejmady P, van Breemen LCA, Hermida-Merino D, Anderson PD, Cardinaels R. Laser sintering of PA12 particles studied by in-situ optical, thermal and X-ray characterization. Addit Manuf 2022;52:102624.
[131] Georgiadis A, Bryant PA, Murray M, Beharrell P, Keddie JL. Resolving the film-formation dilemma with infrared radiation-assisted sintering. Langmuir 2011;27: 2176.
[132] Gonzalez E, Paulis M, Barandiaran MJ, Keddie JL. Use of a Routh-Russel deformation map to achieve film formation of a latex with a high glass transition temperature. Langmuir 2013;29:2044.
[133] Míguez H, Meseguer F, López C, Blanco A, Moya JS, Requena J, et al. Control of the photonic crystal properties of fcc-packed submicrometer SiO_2 spheres by sintering. Adv Mater 1998;10:6.
[134] Sulyanova EA, Shabalin A, Zozulya AV, Meijer J-M, Dzhigaev D, Gorobtsov O, et al. Structural evolution of colloidal crystal films in the process of melting revealed by Bragg peak analysis. Langmuir 2015;31:5274.
[135] Zozulya AV, Meijer J-M, Zaluzhnyy IA, Shabalin A, Ricci A, Westermeier F, et al. In situ X-ray crystallographic study of the structural evolution of colloidal crystals upon heating. J Appl Cryst 2013;46:903.
[136] Zozulya AV, Zaluzhnyy IA, Mukaramova N, Lazarev S, Meijer J-M, Kurta RP, et al. Unravelling the structural rearrangement of polymer colloidal crystals under dry sintering conditions. Soft Matter 2018;14:6849.
[137] Zhao M, Drummer D, Wudy K, Drexler M. Sintering study of polyamide 12 particles for selective laser melting. iJES 2015;3(1):28.
[138] Lotito V, Zambelli T. Pattern detection in colloidal assembly: a mosaic of analysis techniques. Adv Colloid Interface Sci 2020;284:102252.
[139] Khanna S, Utsav Chaliyawala H, Paneliya S, Roy D, Mukhopadhyay K, Banerjee R, et al. Systematic investigation of close-packed silica nanospheres monolayer under sintering conditions. J Eur Ceram Soc 2019;39:1411.
[140] Ruckdeschel P, Kemnitzer TW, Nutz FA, Senker J, Retsch M. Hollow silica sphere colloidal crystals: insights into calcination dependent thermal transport. Nanoscale 2015;7:10059.
[141] Dang A, Hui CM, Ferebee R, Kubiak J, Li T, Matyjaszewski K, et al. Thermal properties of particle brush materials: effect of polymer graft architecture on the glass transition temperature in polymer-grafted colloidal systems. Macromol Symp 2013;331-332:9.
[142] Chen J-T, Lee P-H, Tseng H-F, Chiu Y-J, Kao Y-H, Jeng K-S, et al. On-film annealing: a simple method to fabricate heterogeneous polymer surfaces, porous films, and hemispheres. ACS Macro Lett 2015;4:721.

[143] Tseng H-F, Cheng M-H, Jeng K-S, Li J-W, Chen J-T. Asymmetric polymer particles with anisotropic curvatures by annealing polystyrene microspheres on poly(vinyl alcohol) films. Macromol Rapid Commun 2016;37:1825.
[144] Lo Y-C, Chiu Y-J, Tseng H-F, Chen J-T. Thermal-annealing-induced self-stretching: fabrication of anisotropic polymer particles on polymer films. Langmuir 2017;33:12300.
[145] Lotito V, Sennhauser U, Hafner C. Effects of asymmetric surface corrugations on fully metal-coated scanning near field optical microscopy tips. Opt Express 2010; 18(8):8722.
[146] Lotito V, Sennhauser U, Hafner C. Finite element analysis of asymmetric scanning near field optical microscopy probes. J Comput Theor Nanosci 2010;7(8):1596.
[147] Chibani H, Dukenbayev K, Mensi M, Sekatskii SK, Dietler G. Near-field scanning optical microscopy using polymethylmethacrylate optical fiber probes. Ultramicroscopy 2010;110:211.
[148] Lotito V, Sennhauser U, Hafner C, Bona G-L. Fully metal-coated scanning near-field optical microscopy probes with spiral corrugations for superfocusing under arbitrarily oriented linearly polarised excitation. Plasmonics 2011;6(2):327.
[149] Gigault C, Dalnoki-Veress K, Dutcher JR. Changes in the morphology of self-assembled polystyrene microsphere monolayers produced by annealing. J Colloid Interface Sci 2001;243:143.
[150] Geng C, Zheng L, Yu J, Yan Q, Wei T, Wang X, et al. Thermal annealing of colloidal monolayer at the air/water interface: a facile approach to transferrable colloidal masks with tunable interstice size for nanosphere lithography. J Mater Chem 2012;22:22678.
[151] Lotito V, Sennhauser U, Hafner C. Numerical analysis of novel asymmetric SNOM tips. Progr Electromagn Res Symp; 2011. p. 1505.
[152] Shubeita GT, Sekatskii SK, Dietler G, Potapova I, Mews A, Basché T. Scanning near field optical microscopy using semiconductor nanocrystals as a local fluorescence and fluorescence resonance energy transfer source. J Microsc 2003; 210:274.
[153] Lotito V, Sennhauser U, Hafner C. Interaction of an asymmetric scanning near field optical microscopy probe with fluorescent molecules. Prog Electromagn Res 2011;121:281.
[154] Lotito V, Hafner C, Sennhauser U, Bona G-L. A novel nanostructured scanning near field optical microscopy probe based on an adirectional asymmetry. J Comput Theor Nanosci 2012;9:486.
[155] Jamiolkowski RM, Chen KY, Fiorenza SA, Tate AM, Pfeil SH, Goldman YE. Nanoaperture fabrication via colloidal lithography for single molecule fluorescence analysis. PloS One 2019;14(10):e0222964.
[156] Li Y, Cai W, Cao B, Duan G, Sun F. Fabrication of the periodic nanopillar arrays by heat-induced deformation of 2D polymer colloidal monolayer. Polymer 2005;46: 12033.
[157] Li Y, Cai W, Cao B, Duan G, Li C, Sun F, et al. Morphology-controlled 2D ordered arrays by heating-induced deformation of 2D colloidal monolayer. J Mater Chem 2006;16:609.
[158] Li J, Zhang Y. Porous polymer films with size-tunable surface pores. Chem Mater 2007;19:2581.
[159] Kuno G, Sakaguchi K. Anti-reflective biomimetic nanostructures formed by 2D arrays of silica colloidal particles via self-assembly using sublimation, polymer solidification, and thermal fusion. Appl Surf Sci 2021;564:150406.
[160] Yi DK, Kim D-Y. Polymer nanosphere lithography: fabrication of an ordered trigonal polymeric nanostructure. Chem Commun 2003;9(8):982.
[161] King JS, Gaillot DP, Graugnard E, Summers CJ. Conformally back-filled, non-close-packed inverse-opal photonic crystals. Adv Mater 2006;18:1063.
[162] Uğur Ş, Pekcan Ö. The effect of annealing temperature on latex film dissolution. J Colloid Interface Sci 2004;277:359.
[163] Yang S, Slotcavage D, Mai JD, Liang W, Xie Y, Chen Y, et al. Combining the masking and scaffolding modalities of colloidal crystal templates: plasmonic nanoparticle arrays with multiple periodicities. Chem Mater 2014;26:6432.
[164] Schöttle M, Tran T, Feller T, Retsch M. Time-temperature integrating optical sensors based on gradient colloidal crystals. Adv Mater 2021:2101948.
[165] Míguez H, Tétreault N, Hatton B, Yang SM, Perovic D, Ozin GA. Mechanical stability enhancement by pore size and connectivity control in colloidal crystals by layer-by-layer growth of oxide. Chem Commun 2002;22:2736.
[166] Astratov. Photonic band gaps in 3D ordered fee silica matrices. Phys Lett A 1996; 1996(222):349.
[167] Mayoral R, Requena J, Moya JS, López C, Cintas A, Míguez H, et al. 3D long-range ordering in an SiO_2 submicrometer-sphere sintered superstructure. Adv Mater 1997;9(3):257.
[168] Gates B, Park SH, Xia Y. Tuning the photonic bandgap properties of crystalline arrays of polystyrene beads by annealing at elevated temperatures. Adv Mater 2000;12(9):653.
[169] Vlasov YA, Astratov VN, Karimov OZ, Kaplyanskii AA, Bogomolov VN, Prokofiev AV. Existence of a photonic pseudogap for visible light in synthetic opals. Phys Rev B 1997;55(20):357.
[170] Tahami SHV, Pourmahdian S, Hadavand BS, Azizi ZS, Tehranci MM. Thermal tuning the reversible optical band gap of self-assembled polystyrene photonic crystals. Photonic Nanostruct 2016;22:40.
[171] Li J, Xue L, Wang Z, Han Y. Colloidal photonic crystals with a graded lattice-constant distribution. Colloid Polym Sci 2007;285:1037.
[172] Deng T-S, Zhang J-Y, Zhu K-T, Zhang Q-F, Wu J-L. Improving the optical properties of vinyl-functionalized silica colloidal crystals by thermal annealing. J Cerma Soc Jpn 2010;118(10):862.
[173] Deng T-S, Zhang J-Y, Zhu K-T, Zhang Q-F, Wu J-L. Controlled tuning of the stop band of colloidal photonic crystals by thermal annealing. Opt Mater 2010;32:946.
[174] Jurewicz I, King AAK, Shanker R, Large MJ, Smith RJ, Maspero R, et al. Mechanochromic and thermochromic sensors based on graphene infused polymer opals. Adv Funct Mater 2020;30:2002473.
[175] Nutz FA, Ruckdeschel P, Retsch M. Polystyrene colloidal crystals: Interface controlled thermal conductivity in an open-porous mesoparticle superstructure. J Colloid Interface Sci 2015;457:96.
[176] Nutz FA, Retsch M. Tailor-made temperature-dependent thermal conductivity via interparticle constriction. Sci Adv 2017;3(11):aao5238.
[177] Shklover V. Formation of aligned microfiber arrays via self-assembling SiO_2 nanocolloids. Change of microfiber structure during annealing. Chem Mater 2005;17:608.
[178] Moran JL, Wheat PM, Posner JD. Submicron scale patterning in sintered silica colloidal crystal films using a focused ion beam. Langmuir 2008;24(18):10532.
[179] Zhang L, D'Acunzi M, Kappl M, Imhof A, van Blaaderen A, Butt H-J, et al. Tuning the mechanical properties of silica microcapsules. Phys Chem Chem Phys 2010; 12:15392.
[180] Tsai P-S, Yang Y-M, Lee Y-L. Hierarchically structured superhydrophobic coatings fabricated by successive Langmuir-Blodgett deposition of micro−/nano-sized particles and surface silanization. Nanotechnology 2007;18:465604.
[181] Dinsmore AD, Hsu MF, Nikolaides MG, Marquez M, Bausch AR, Weitz DA. Colloidosomes: selectively permeable capsules composed of colloidal particles. Science 2002;298(5595):1006.
[182] Al-Shehri H, Horozov TS, Paunov VN. Preparation and attachment of liquid-infused porous supra-particles to liquid interfaces. Soft Matter 2016;12:8375.
[183] Yuan C, Xu Y, Jiang N, Chen G, Xu B, He N, et al. Colloidosomes constructed by the seamless connection of nanoparticles: a mobile and recyclable strategy to intelligent capsules. Soft Matter 2011;7:3366.
[184] Grebe V, Liu M, Weck M. Tools for the quantification of the dynamic assembly of colloidal chains of ellipsoidal particles. Colloid Interface Sci Commun 2022;50: 100661.
[185] Ben-Akiva E, Meyer RA, Yu H, Smith JT, Pardoll DM, Green JJ. Biomimetic anisotropic polymeric nanoparticles coated with red blood cell membranes for enhanced circulation and toxin removal. Sci Adv 2020;6:eaay9035.
[186] Nowak M, Brown TD, Graham A, Helgeson ME, Mitragotri S. Size, shape, and flexibility influence nanoparticle transport across brain endothelium under flow. Bioeng Transl Med 2020;5:e10153.
[187] Ma H, Bolster C, Johnson WP, Li K, Pazmino E, Camacho KM, et al. Coupled influences of particle shape, surface property and flow hydrodynamics on rod-shaped colloid transport in porous media. J Colloid Interface Sci 2020;577:471.
[188] Kao P-K, VanSaders BJ, Durkin MD, Glotzer SC, Solomon MJ. Anisotropy effects on the kinetics of colloidal crystallization and melting: comparison of spheres and ellipsoids. Soft Matter 2019;15:7479.
[189] Roller J, Geiger JD, Voggenreiter M, Meijer J-M, Zumbusch A. Formation of nematic order in 3D systems of hard colloidal ellipsoids. Soft Matter 2020;16: 1021.
[190] Yu B, Cong H, Peng Q, Gu C, Tang Q, Xu X, et al. Current status and future developments in preparation and application of nonspherical polymer particles. Adv Colloid Interface Sci 2018;256:126.
[191] Liu J, Huang J, Niu W, Tan C, Zhang H. Unconventional-phase crystalline materials constructed from multiscale building blocks. Chem Rev 2021;121:5830.
[192] Yin Y, Lu Y, Xia Y. A self-assembly approach to the formation of asymmetric dimers from monodispersed spherical colloids. J Am Chem Soc 2001;123:771.
[193] Yake AM, Panella RA, Snyder CE, Velegol D. Fabrication of colloidal doublets by a salting out-quenching-fusing technique. Langmuir 2006;22(22):9135.
[194] Yi DK, Seo E-M, Kim D-Y. Fabrication of a mesoscale wire: sintering of a polymer colloid arrayed inside a one-dimensional groove pattern. Langmuir 2002;18: 5321.
[195] Ramírez LM, Milner ST, Snyder CE, Colby RH, Velegol D. Controlled flats on spherical polymer colloids. Langmuir 2010;26(10):7644.
[196] Wu P, Peng L, Tuo X, Wang X, Yuan J. Control of deposition channels in nanosphere templates for high-density nanodot array production. Nanotechnology 2005;16:1693.
[197] Weon BM, Kim JT, Je JH, Yi JM, Wang S, Lee W-K. Colloid coalescence with focused X rays. Phys Rev Lett 2011;107:018301.
[198] Senyuk B, Liu Q, He S, Kamien RD, Kusner RB, Lubensky TC, et al. Topological colloids. Nature 2013;493:200.
[199] Martinez A, Ravnik M, Lucero B, Visvanathan R, Žumer S, Smalyukh II. Mutually tangled colloidal knots and induced defect loops in nematic fields. Nat Mater 2014;13:258.
[200] Chen S, Pirhadi E, Yong X. Viscoelastic necking dynamics between attractive microgels. J Colloid Interface Sci 2022;618:283.
[201] Anumol EA, Viswanath B, Ganesan PG, Shi Y, Ramanath G, Ravishankar N. Surface diffusion driven nanoshell formation by controlled sintering of mesoporous nanoparticle aggregates. Nanoscale 2010;2:1423.